Study of Particle Transport in a High Power Spallation Target for an Accelerator-Driven Transmutation System

From the Faculty of Georesources and Materials Engineering of the RWTH Aachen University

Submitted by

Nikhil Vittal Shetty, M.Sc.

from Udupi, India

in respect of the academic degree of

Doctor of Engineering

approved thesis

Advisors: Univ.-Prof. Dr. rer. nat. Bruno Thomauske
Professor Dr. rer. nat. Rahim Nabbi
Univ.-Prof. Dr. rer. nat. Hans-Josef Allelein

Date of the oral examination: 31.01.2013

Abstract

Transmutation of highly radioactive nuclear waste can be performed using an accelerator-driven system (ADS), where high energy protons impinge on a spallation target to produce neutrons. These neutrons are multiplied in a sub-critical core, while simultaneously fissioning the minor actinides into short-lived or stable nuclides. AGATE is a project envisaged to demonstrate the feasibility of transmutation in a gas (helium) cooled ADS using solid spallation target. Development of the spallation target module and assessing its safety aspects are studied in this work. According to the AGATE concept parameters, 600 MeV protons are delivered on to the segmented tungsten spallation target. Tungsten is an ideal solid spallation target material because of its high melting point, other than the many desirable properties.

Spallation is by far the most attractive means of neutron production when it comes to energy deposition per neutron. The spallation mechanism initiates with intra-nuclear cascade (INC) reactions, followed by de-excitation of nuclei through evaporation, multi-fragmentation and fission. Both the INC and de-excitation processes lead to the production of neutrons and spallation products. Spallation neutron energy spectrum is relatively harder compared to fission because of the higher energetics involved. The monte carlo toolkit Geant4 has been used in the simulation of particle transport. Binary cascade is used to simulate INC, along with the G4NDL neutron data library for low energy neutrons (< 20 MeV).

From the systematics study of incident projectile types (proton, deuteron and ^{4}He), neutron yield due to proton and deuteron are generally higher than that for ^{4}He. At higher energies, deuteron fares better than proton. Given the lower kinetic energy of proton (600 MeV) and owing to the fact that acceleration cost increases with increasing mass, proton turns out to be the ideal projectile for the current system. Energy cost of neutron production is the most efficient for protons of energy between 800 - 1000 MeV. Nuclear collision probability increases with increasing proton energy, reaching a saturation value at about 1 GeV for tungsten. Nuclear collision probability in tungsten is about 80% for 600 MeV protons. To ensure maximum interaction, the target length needs to be as long as the range of protons in the material. For 600 MeV protons, the range is about 15 cm in tungsten. There exists an optimum radius of the target determining the neutron yield. While lower radii means the leakage of energetic secondaries without producing further neutrons, larger radii results in the parasitic absorption. For tungsten, target radius of about 10 cm turns out to be a good option.

About 70% of the beam power is lost in target heating for all materials at 600 MeV. Protons, both secondaries and primaries are responsible for more than 80% of energy deposition in the target. To facilitate adequate cooling of the target and to distribute the neutron yield along the length of the target, segmentation of the target is necessary.

In a monolith tungsten target, neutron build-up near the target head is not very suitable to illuminate the sub-critical core coupled to the target. Hence splitting the target using flux-traps into segments of varying thicknesses is necessary to produce a homogenized neutron field. This also leads to the hardening of the emitted neutron energy spectrum required for transmutation. Further, the flux-traps allow efficient cooling and reduced parasitic absorption in the target. Power density in the optimized target is still very high to be cooled. Fluidizing the target with pebbles instead of solid material is a feasible option. Thermal hydraulic studies of the first segment of the optimized pebble

bed target indicates that the maximum temperature reached in the tungsten pebbles is about 670 °C, which is well below the recrystallization temperature (1350 °C) and melting point (3410 °C) of tungsten. Major problem of the optimized target is the leakage of high energy protons, which can be solved by making the target radially composite.

Radiation damage has been calculated using the NRT theory for one full power year operation and per mA proton current. Damage is significant in the first few segments of the target, decreasing gradually with increasing tungsten length. Maximum damage in the target is inflicted on the first segment, about 4.5 dpa and the total damage is about 53 dpa. Total helium production in the target is about 7340 appm. Radiation damage in the aluminum proton beam window (PBW) is comparatively lower (0.81 dpa and 149 helium appm).

Total specific activity in the target at shutdown after one full power year operation is about 2.4×10^{14} MBq/g per mA. Production cross section of the most radiotoxic nuclide ^{148}Gd is about 2.4 mb in the target. Other isotopes contributing large amounts of activity in the target are positron emitters such as, ^{172}Hf, ^{173}Lu, ^{174}Lu and ^{179}Ta. The hard gamma emitter,^{60}Co is also present in significant amounts in the target. Unlike the actinides, which need to be transmuted, radionuclides produced in the target are less radiotoxic and have shorter life time. Major radionuclides found in PBW cooling water are ^{7}Be and ^{11}C, and additionally in aluminum are ^{18}F, ^{22}Na and ^{24}Na.

Spallation produces high energy neutrons and gammas which need to be shielded. An additional dimension in the shielding calculation is introduced by the high energy forward-peaked neutrons. Shields composed of boronated steel and boronated concrete are used, which greatly reduces the shielding dimensions while exhibiting good shielding performance. This also reduces the amount of activated materials. An inner thick layer of iron is required to attenuate the high energy of neutrons. The concrete block following this is efficient in shielding against the low energy neutrons. With the same shielding material configuration, gammas tend to attenuate relatively faster than the neutrons.

Zusammenfassung

Die Transmutation von hochradioaktiven Stoffen kann unter Verwendung eines beschleunigergetriebenen Systems (ADS) erfolgen. In diesem treffen hochenergetische Protonen auf ein Spallationstarget, um Neutronen zu erzeugen. Diese Neutronen werden in einem unterkritischen Reaktor vervielfacht und spalten die Aktiniden in kurzlebige oder stabile Nuklide. AGATE ist ein Projekt, um die Machbarkeit einer gasgekühlten beschleunigergetriebenen Transmutationsanlage zu zeigen. Die Entwicklung eines Spallationstargets und die Bewertung der Sicherheitsaspekte werden in dieser Arbeit untersucht. Die Auslegung in der AGATE-Studie sieht einen 600 MeV Protonenstrahl vor, welcher auf ein segmentiertes Wolfram Target trifft. Wolfram ist aufgrund seiner günstigen physikalischen Eigenschaften wie zum Beispiel dem Schmelzpunkt und der hohen Neutronenausbeute ideal für ein Feststofftarget als Spallationsquelle.

Spallation ist die attraktivste Methode um Neutronen zu erzeugen, wenn es auf die Leistungsdichte pro Neutron ankommt. Der Spallationsmechanismus initiiert intra-nukleare Kaskaden (INC) mit anschließender Abregung der Atomkerne durch Verdampfung, Multi-Fragmentierung oder Spaltung. Sowohl die INC als auch die Abregungsprozesse führen zur Produktion von Neutronen und Spallationsprodukten. Das Energiespektrum der Spallationsneutronen ist härter als das für Spaltneutronen. Das Monte Carlo Toolkit Geant4 ist für die Simulation von Teilchentransport benutzt worden. Binary cascade wird verwendet, um die INC zusammen mit der Neutrondatenbank G4NDL für niederenergetische Neutronen (<20 MeV) zu simulieren.

Aus der Systematikstudie der einfallenden Projektiltypen (Proton, Deuteron und ^{4}He) geht hervor, dass die Neutronenausbeute bei Protonen und Deuteronen in der Regel höher als die für ^{4}He ist. Dabei haben bei höheren Energien Deuteronen die höchste Neutronenausbeute. Angesichts der niedrigeren kinetischen Energie der Protonen (600 MeV) und aufgrund der Tatsache, dass die Beschleunigungskosten mit zunehmender Projektilmasse steigen, werden Protonen im aktuellen System verwendet. Die Energiekosten der Neutronenproduktion ist am niedrigsten für Protonen von Energien zwischen 800 - 1000 MeV. Die nukleare Kollisionswahrscheinlichkeit steigt mit zunehmender Protonenenergie und erreicht einen Sättigungswert bei etwa 1 GeV für Wolfram und beträgt etwa 80% für 600 MeV Protonen.

Um eine maximum Wechselwirkung zu gewährleisten, muss die Targetlänge gleich der Eindringtiefe der Protonen sein. In Wolfram beträgt diese ca. 15 cm für Protonen mit einer Energie von 600 MeV. Die Neutronenausbeute kann über eine Anpassung des Targetradius optimiert werden. Während kleinere Radien das Austreten von energetischen Sekundärteilchen ohne weitere Neutronenbildung bewirken, erhöhen größere die parasitäre Absorption. Für Wolfram stellt ein Radius von 10 cm eine optimale Größe dar, um eine gute Neutronenausbeute zu gewährleisten.

Etwa 70% der Strahlleistung geht durch Targetaufheizung bei alle Materialien für 600 MeV Proton verloren. Protonen sind, sowohl als primäre als auch als sekundäre, mit 80% maßgeblich für die Leistungsdichte im Target verantwortlich. Um eine ausreichende Kühlung des Targets zu erleichtern und die Neutronenausbeute entlang der Länge des Targets zu verteilen, ist eine Segmentierung des Targets notwendig.

In einem monolithen Wolfram ist der Neutronenaufbau in der Nähe des Targetkopfs nicht geeignet, um den Reaktor zu beleuchten. Daher ist das Aufteilen des Targets in verschiedene Segmente mit unterschiedlichen Dicken notwendig, um ein homogenisiertes

Neutronenfeld zu erzeugen. Dies führt auch zu einer Verhärtung des emittierten Neutronenspektrums, welches für die Transmutation benötigt wird. Außerdem ermöglichen die Abstände der verschiedenen Segmente eine effiziente Kühlung und reduzieren die parasitäre Absorption im Target. Die Leistungsdichte in dem optimierten Target ist immer noch sehr hoch und es muss deshalb gekühlt werden. Die Fluidisierung des Targets mit Kugeln statt festem Material ist physikalisch möglich und technisch realisierbar. Thermohydraulische Studien des ersten Segments des optimierten Kugelhaufentargets zeigen, dass die maximale Temperatur in einer Wolframkugel etwa 670 °C erreicht, was deutlich unter sowohl der Rekristallisationstemperatur von 1350 °C als auch des Schmelzpunkts von 3410 °C liegt. Das Hauptproblem des optimierten Targets ist das Austreten von hochenergetischen Protonen.

Strahlenschäden wurden unter Verwendung der NRT-Theorie für ein Betriebsjahr unter Volllast pro mA Protonenstrom berechnet. Die Schäden sind in den ersten Abschnitten des Targets erheblich, verringern sich allerdings mit zunehmender Länge des Wolframs. Der maximale Schaden wird dem Ziel auf dem ersten Segment zugefügt und beträgt etwa 4,5 dpa, wobei der Gesamtschaden bei etwa 53 dpa liegt. Insgesamt beträgt die Heliumproduktion im Ziel etwa 7340 appm. Strahlenschäden in dem Aluminium-Protonenstrahlfenster (PBW) sind vergleichsweise niedrig (0,81 dpa und 149 Helium appm).

Insgesamt ist die spezifische Aktivität im Ziel nach dem Herunterfahren nach einem Betriebsjahr unter Volllast etwa $2{,}4\times10^{14}$ MBq / g pro mA. Der Produktionsquerschnitt des radiotoxischen Nuklids ^{148}Gd beträgt etwa 2,4 mb im Target. Andere Isotope tragen große Mengen an Aktivität im Target bei und sind Positronen-Emitter wie ^{172}Hf, ^{173}Lu, ^{174}Lu und ^{179}Ta. Der harte Gamma-Strahler ^{60}Co ist auch in signifikanten Mengen im Ziel vorhanden. Im Gegensatz zu den Aktiniden, die umgewandelt werden müssen, haben Radionuklide, die im Target produziert werden, eine vergleichsweise geringere Radiotoxizität und kürzere Lebensdauern. Wesentliche Radionuklide, die in PBW Kühlwasser gefunden werden, sind ^{7}Be und ^{11}C. Zusätzlich lassen sich im Aluminium ^{18}F, ^{22}Na und ^{24}Na nachweisen.

Spallation produziert hochenergetische Neutronen und Gammas, die abgeschirmt werden müssen. Eine zusätzliche Abschirmungsberechnung muss durch die hohen Energien der Neutronen erfolgen, die in Richtung des Protonenstrahls emittiert werden. Die Abmessung der Abschirmung kann reduziert werden, wenn sie aus boriertem Stahl und boriertem Beton zusammengesetzt wird. Zusätzlich bietet diese Zusammensetzung eine ausreichende Abschirmleistung. Dies reduziert auch die Menge des aktivierten Materials. Eine innere dicke Schicht aus Eisen ist jedoch erforderlich, um die hohen Energien der Neutronen zu dämpfen. Neutronen mit niedriger Energie werden effizient durch einen zusätzlichen Betonblock abgeschirmt. Mit der gleichen Konfiguration der Abschirmmaterialen können Gammas sogar schneller als die Neutronen gedämpft werden.

Acknowledgments

My first and foremost thanks to Prof. Dr. rer. nat. Bruno Thomauske for providing me an opportunity to pursue doctoral studies at the Institute of Nuclear Fuel Cycle (INBK), RWTH Aachen University and also for supervising the thesis. I am grateful for his valuable suggestions and regular evaluations during the different phases of the thesis work. I would like to acknowledge my advisor, Prof. Dr. Rahim Nabbi for his kind support and guidance throughout the course of the thesis. My earnest thanks to him for supporting me since my master studies at the Aachen University of Applied Sciences, Jülich.

I had a wonderful working atmosphere in Aachen, thanks to my colleagues at INBK. Social engagements with them in many different events have helped me to boost my morale and at times, very much needed. I would like to mention Klaus Biß and Stephan Rohmen, with whom I could share my ideas and experiences, often followed by creative and lively discussions. I would also thank them for setting up and maintaining the computer cluster at INBK, which was used to perform nuclear simulations.

I would like to thank the colleagues at the Forschungszentrum Jülich, who were concurrently working on the AGATE project, for exchanging ideas and information on various technical issues of the project. I would like to acknowledge Mr. Alain Boudard from CEA, Saclay and Mr. Nikolai Sobolevsky from INR, Moscow for their discussions on spallation models and ADS technology, which have helped me to deepen my knowledge regarding the subject.

My sincere thanks to Wissenschaftlich-Technische Ingenieurberatung (WTI) GmbH, Jülich for providing me with the scholarship, which had greatly supported me financially.

Contents

1 Introduction **10**
- 1.1 Background . . . 10
- 1.2 Objectives . . . 12
- 1.3 Partitioning and Transmutation . . . 14
- 1.4 Accelerator-Driven System . . . 17
- 1.5 Advanced Gas-cooled Accelerator-driven Transmutation Experiment . . . 22
- 1.6 Literature Survey . . . 23

2 Physics Principles of Spallation Reactions **28**
- 2.1 Mechanism of Spallation Reactions . . . 28
- 2.2 Characteristics of Spallation Neutrons . . . 34
- 2.3 Formation of Spallation Products . . . 37
- 2.4 Application of Spallation Neutron Sources . . . 40

3 Particle Transport Simulation Method and Tool **41**
- 3.1 Monte Carlo Method . . . 41
- 3.2 Geant4 Toolkit . . . 42

4 Particle Production Study in Spallation Reactions **47**
- 4.1 Effect of Projectile Type and Energy on Neutron Yield . . . 47
- 4.2 Effect of Target Material and Geometry on Neutron Yield . . . 51
- 4.3 Particle Production in the Target . . . 55
- 4.4 Energy Deposition Behavior in the Target . . . 60

5 Target Module Development **62**
- 5.1 Beam and Target Material Specification . . . 63
- 5.2 Target Configurations . . . 66
- 5.3 Optimizing Power Density Distribution . . . 68

6 Nuclear Simulation of the Target and Auxiliary Components **74**
- 6.1 Particle Transport Simulation in the Target . . . 74
- 6.2 Particle Transport Simulation in the Proton Beam Window and Stop . . . 80

7 Radiation Damage Calculations **85**
- 7.1 Radiation Damage Phenomenon . . . 85
- 7.2 Mechanism of Atomic Displacements . . . 87
- 7.3 Radiation Damage in the Components . . . 88

8 Radiological Safety Aspects **92**
8.1 Calculation of Radionuclide Inventory 93
8.2 Simulation of Shielding Behavior 98

9 Conclusions and Outlook **105**

Bibliography **109**

A Appendix **121**

List of Figures

1.1 Projections of future nuclear capacity development in the world 10
1.2 Composition of spent nuclear fuel 14
1.3 Ingestion radiotoxicity of 1 ton of spent nuclear fuel 15
1.4 Transmutation of ^{245}Cm isotope using neutron 16
1.5 Ratio of fission-to-capture cross section for ^{240}Pu, ^{243}Am and ^{245}Cm 17
1.6 DTL prototype in assembly stage 18
1.7 The 590 MeV ring cyclotron at PSI 19
1.8 Virtual layout of the AGATE complex 23
1.9 Virtual layout of the AGATE reactor 25

2.1 Illustration of spallation reaction 28
2.2 Nuclear potential wells for neutrons and protons according to the Fermi-gas model 30
2.3 Total and elastic cross section for p-p and p-n scattering, together with experimental data 31
2.4 Course of nuclear cascade in spallation reaction 31
2.5 De-excitation modes of an excited residual nucleus 32
2.6 Probability distribution of evaporation neutrons 33
2.7 Comparison of fission and spallation neutron spectrum 35
2.8 Neutron multiplicity distributions for a 10 cm radius tungsten target bombarded by protons of 600 MeV energy 36
2.9 Double differential cross section for neutron emission from lead spallation . 37
2.10 Angular distribution of neutrons in different energy groups for a 10 cm diameter tungsten target bombarded by protons of 600 MeV energy 38
2.11 Distribution of spallation products in Hg target due to 1.334 GeV protons 39

3.1 Random walk of particles in monte carlo method 42
3.2 Double differential cross section for neutrons produced in proton scattering at 7.5 degrees by 256 MeV protons 44
3.3 Double differential cross section for neutrons produced in proton scattering off lead 45
3.4 Double differential cross section for tritium production in proton scattering off nickel 45
3.5 Comparison of absolute neutron fluence data in the TARC experiment with the Geant4 simulation data 46

4.1 Projected range of protons with different energies in some materials 48
4.2 Comparison of neutron yield in lead due to p, d, and ^{4}He with the experimental data 49

4.3 Comparison of neutron yield in Pb, Hg and W due to protons with the experimental data . . . 50
4.4 Neutron yield in Pb, Hg and W normalized to proton energy . . . 51
4.5 Mass number distribution of spallation products in Pb, W, ^{nat}U and Sn targets irradiated by 1.6 GeV protons . . . 52
4.6 Neutron yield due to protons in W targets of different radii . . . 53
4.7 Neutron yield along the length of W target with 600 MeV protons . . . 54
4.8 Neutron multiplicity due to 1.8 GeV protons on a W target of 15 cm in diameter and various thicknesses . . . 55
4.9 Energy deposition along the length of W target with 600 MeV protons . . . 55
4.10 Neutron production in W, Hg and Pb targets due to 600 MeV protons . . . 56
4.11 Lateral neutron yield in W, Hg and Pb targets due to 600 MeV protons . . . 57
4.12 Lateral straggling of incident protons of various energies in a W target . . . 57
4.13 Gamma production in W, Hg and Pb targets due to 600 MeV protons . . . 58
4.14 Spallation Products in W, Hg, Pb targets due to 600 MeV protons . . . 59
4.15 Total energy deposition in W, Hg and Pb targets normalized to beam energy 60

5.1 Scheme of an accelerator-driven sub-critical system . . . 63
5.2 Technical specification of beam parameters . . . 64
5.3 Radiative neutron capture cross section for ^{184}W . . . 65
5.4 Diagram illustrating the split-target concept and its different configurations 66
5.5 Optimized tungsten target for the AGATE concept . . . 67
5.6 Individual segment thickness of the optimized target . . . 67
5.7 Energy deposition in W, Hg and Pb targets due to protons with different energies . . . 69
5.8 Rotating tungsten target arrangement of a 3 MW spallation source . . . 70
5.9 Schematic illustrating the effect of inclined target on the beam footprint . 71
5.10 Flowing powder target as a solution to the challenges at high power . . . 72
5.11 First segment of the optimized tungsten target fluidized using layers of pebbles . . . 72
5.12 Simulation of power density distribution in a pebble and temperature profile in the first layer of the pebble bed target . . . 73

6.1 Power density in monolith tungsten target . . . 75
6.2 Neutron flux in monolith tungsten target . . . 75
6.3 Power density in segmented tungsten target . . . 76
6.4 Neutron flux in segmented tungsten target . . . 76
6.5 Power density in optimized tungsten target . . . 77
6.6 Neutron flux in optimized tungsten target . . . 77
6.7 Comparison of laterally leaking neutron energy spectrum for different targets 79
6.8 Comparison of leaking proton energy spectrum for different targets . . . 80
6.9 Total incident proton cross section for ^{27}Al, ^{48}Ti and ^{56}Fe . . . 81
6.10 Simplified model of aluminum PBW implemented in simulation . . . 82
6.11 Power density in aluminum PBW . . . 83
6.12 Temperature profile in aluminum PBW (outer and inner shells) . . . 83
6.13 Power density in graphite beamstop . . . 84
6.14 Neutron flux in graphite beamstop . . . 84

7.1 Schematic diagram illustrating the defects produced in lattice by PKAs . . . 85

7.2 Transmission electron-microscopy micrographs of typical radiation induced defects in metals 86
7.3 Displacement cross section for tungsten due to secondary neutrons and protons 88
7.4 Kinetic energy of generic ions produced in the tungsten target 89
7.5 Comparison of compression stress/strain results for irradiated tungsten . . 91

8.1 The spallation target module along with the circulation of He coolant . . . 92
8.2 Decay of nuclide inventory in the target after one FPY operation 94
8.3 Total neutron interaction cross section for ^{56}Fe 100
8.4 Neutron and gamma spectrum leaking from the target 100
8.5 FLUKA model used in the simulation of shielding behaviour 101
8.6 Neutron spectrum in different layers of the shielding (forward direction) . . 101
8.7 Neutron spectrum in different layers of the shielding (sideward direction) . 102
8.8 Neutron spectrum in different layers of the shielding (forward direction) including transmutation zone 102
8.9 Gamma spectrum in different layers of the shielding (forward direction) . . 103
8.10 Gamma spectrum in different layers of the shielding (sideward direction) . 104

List of Tables

1.1 Radioactive characteristics of isotopes in spent nuclear fuel 14
1.2 List of main parameters of the AGATE concept 24
1.3 Main parameters of some existing spallation neutron sources 25

2.1 Features of some mechanisms for neutron production 34

4.1 Experimental coefficients for neutron yield due to p, d and ^{4}He on lead target 48
4.2 Nuclear collision probabilities for protons of different energies on tungsten . 50
4.3 Neutron production and leakage in W, Hg and Pb targets due to 600 MeV protons 58
4.4 Gammas and spallation products produced in W, Hg and Pb targets due to 600 MeV protons 59
4.5 Energy deposition in W, Hg and Pb targets due to 600 MeV protons . . . 61
4.6 Contributions from various particle types to energy deposition by 1.1 GeV protons on a slab target 61

5.1 Effect of target material density on power deposition 69

6.1 Performance comparison of the different target configurations 79
6.2 Composition of elements in AlZnMgCu1,5 in mass %, other than aluminum 81

7.1 Radiation damage and helium production in the target segments 90
7.2 Radiation damage and helium production in the PBW surfaces 91

8.1 Nuclides with half life shorter than one year, and present in the target at shutdown in amounts of more than one MBq after one FPY operation . . . 95
8.2 Radionuclides present in the aluminum PBW at shutdown after one FPY operation 96
8.3 Radionuclides present in the cooling water of PBW at shutdown after one FPY operation 97
8.4 Radionuclides present in the graphite beam stop at shutdown after one FPY operation 97

A.1 Physical properties and abundance of period 6 elements 121
A.2 Isotopic composition of natural tungsten 121
A.3 Atomic and physical properties of tungsten 122
A.4 Material data for helium 122
A.5 Properties of different PBW materials 123
A.6 Recommended values for displacement threshold energy 124
A.7 Radiation weighting factors 124

A.8 Flux-to-dose conversion factors for neutrons 125
A.9 Flux-to-dose conversion factors for photons 126
A.10 Comparison of properties of shielding materials 126
A.11 Mechanical and thermal properties of different types of concrete 127
A.12 Composition of boronated steel 127
A.13 Composition of boronated concrete 127

List of Abbreviations

ADS	Accelerator-Driven System
ADSS	Accelerator-Driven Sub-Critical System
AGATE	Advanced Gas-Cooled Accelerator-Driven Transmutation Experiment
appm	atomic particles per million
ATW	Accelerator Transmutation of Waste
BIC	Binary Cascade
CCDTL	Cell-Coupled Drift Tube Linac
CERN	European Organization for Nuclear Research
CTR	Controlled Thermonuclear Reactions
CW	Continuous Wave
DPA	Displacements Per Atom
DTL	Drift Tube Linac
EA	Energy Amplifier
ED	Energy Deposition
EFIT	European Facility for Industrial Transmutation
EM	Electro-Magnetic
ENSDF	Evaluated Nuclear Structure Data File
EUROTRANS	European Research Program for the Transmutation of High-Level Nuclear Waste in an Accelerator-Driven System
FBR	Fast Breeder Reactor
FPY	Full Power Year
Geant4	Geometry and Tracking
HLW	High Level Waste
IAEA	International Atomic Energy Agency

IMF	Intermediate Mass Fragment
INC	Intra-Nuclear Cascade
J-PRAC	Japanese Proton Accelerator Research Complex
LBE	Lead-Bismuth Eutectic
LGE	Lead-Gold Eutectic
LHC	Large Hadron Collider
Linac	Linear Accelerator
MA	Minor Actinide
MC	Monte Carlo
MEGAPIE	MEGAwatt PIlot Experiment
MOX	Mixed-Oxide
MP	Melting Point
MYRRHA	Multi-purpose Hybrid Research Reactor for High-tech Applications
P&T	Partitioning and Transmutation
PBW	Proton Beam Window
PKA	Primary Knock-on Atom
PMQs	Permanent Magnet Quadrupoles
PSI	Paul Scherrer Institute
QMD	Quantum Molecular Dynamics
RDM	Radioactive Decay Module
RF	Radio Frequency
SC	Super Conducting
SINQ	Swiss Spallation Neutron Source
SNF	Spent Nuclear Fuel
SP	Spallation Product
STM	Spallation Target Module
TARC	Transumatation by Adiabatic Resonance Crossing
TEF	Transmutation Experimental Facility
TRUs	Transuranic Elements
XT-ADS	Experimental ADS

CHAPTER 1

Introduction

1.1 Background

Energy is in demand. The consumption of energy in the form of electricity is ever increasing in the world. Nuclear power is an important source of electricity. The self-sustained chain reaction in fission reactors is used in the production of nuclear power. At the end of the year 2010, there were 441 nuclear power reactors in operation worldwide with a total capacity of 375 GW_e [IAEA, 2011]. This corresponds to about 6.5% of the total electricity consumption [CIA, 2009]. Moreover, the number of nuclear power reactors being built is rising. Figure 1.1 displays the projections of future nuclear capacity development in the world according to IAEA. It shows that the nuclear power production will increase at least by a factor of two if not less across the subcontinents in the world by the year 2050, implying that the number of nuclear power reactors will also increase by about the same magnitude in relation to the present scenario. The generation of nuclear power is associated with the nuclear waste, emerging as the byproduct in the spent nuclear fuel (SNF). Because nuclear waste is radiotoxic, its disposal and effects on the biosphere are concerning, even more in a situation when the demand for nuclear power is increasing.

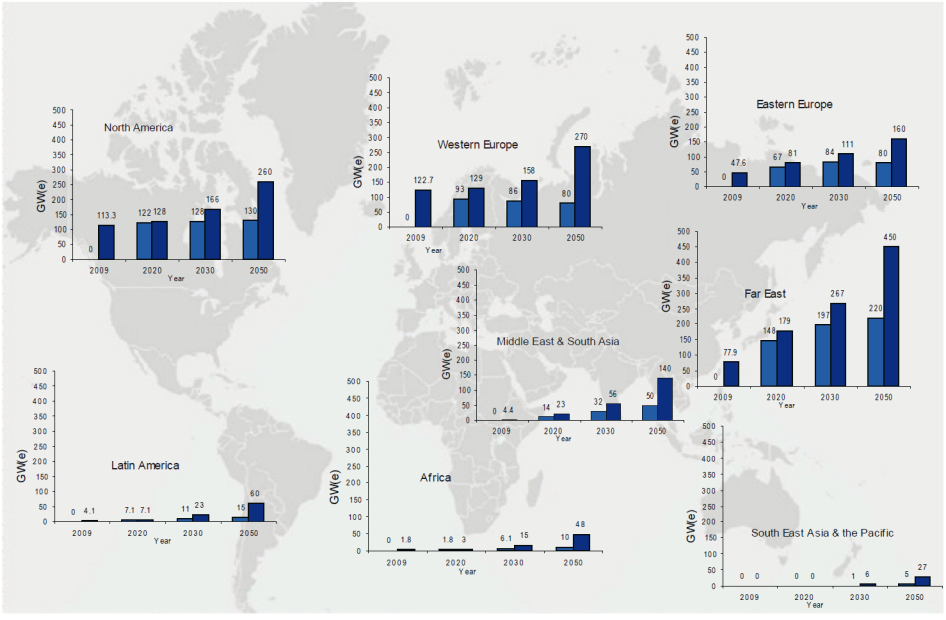

Figure 1.1: Projections of future nuclear capacity development in the world [IAEA, 2010]

Reprocessing of the SNF based on the solvent extraction process exists allowing for the separation of three main streams of nuclides [IAEA, 2008b]:

1. uranium
2. plutonium
3. waste (fission products and minor actinides)

The extracted actinides are recycled in the form of mixed-oxide (MOX) fuel in fast breeder reactors (FBR). This results in the reduction of the volume of high level waste (HLW), restricting the waste inventory to fission products and minor actinides (MA).

The final HLW inventory is composed of radionuclides some of whose half-lives are so long that the decay profiles of these radionuclides match the geological time periods. Furthermore, they are radiotoxic and with no obvious applicability, are simply let to decay. Proposed disposal strategies include launching them into outer space, burning them in dedicated nuclear facilities and storage in deep underground facilities specially designed for this purpose [Herrera-Martínez, 2004]. In the wake of current situation, geological disposal is the realistic strategy. On the other hand, the development of such disposal sites are under constant public agitation.

To counter the deadlock involving nuclear waste as described above, Partitioning and Transmutation (P&T) is envisaged as a viable solution. This way, the radiotoxic component is separated from the spent fuel through the process of Partitioning and is recycled to recover the contained energy in useful way through the process of Transmutation, overall mitigating the toxicity and potential health hazard of nuclear waste while optimizing benefit for the society [Mueller, 2009]. The long-lived nuclides are transmuted into stable or safer nuclides thereby reducing the burden on the geological repositories. P&T can be implemented either in a critical or a sub-critical system. Owing to the limited safety margins of MAs as a fuel in the critical reactor, the latter approach of burning them in a sub-critical reactor is preferable.

A sub-critical reactor is driven by an Accelerator-Driven System (ADS) to compensate for the loss of neutron economy which otherwise would have been self-sustaining in a critical reactor. In an ADS, energetic light charged particles such as protons are bombarded on a target to produce a very intense source of neutrons which can be consequently multiplied in the sub-critical reactor surrounding the target [IAEA, 1997]. The collection of physics reactions in play behind the interaction of charged particles with the material is collectively called as spallation process.

The "spalled" target nuclei is the source of neutrons and other hadrons which find further applications not only in the framework of P&T but also in thermal neutron beam sources, materials irradiation studies, isotope production, and power generation [Broome, 1996]. Spallation process depends on the material properties, the kinetic energy of the projectile and the geometric configuration of the target. The beam power of the projectiles in the technology incorporating spallation process ranges up to a few megawatts, hence presenting a formidable challenge in the design of the target and related accessories. This work addresses the various aspects in relation to the design of a high power spallation target module (STM) for an ADS driven transmutation and the study of its particle transport behavior.

1.2 Objectives

This section discusses the tasks that were stipulated which were seen as mandatory in an holistic approach of developing the spallation target module. Simultaneously, providing details on the flow of work and structure of the document.

The principle of P&T is elaborated in section 1.3. The nature of nuclear waste to be transmuted and their interaction with neutrons is discussed in detail. The neutronic requirements in efficiently transmuting the long-lived radionuclides into short-lived or stable nuclides and the impact of final storage in geological repositories on the biosphere are assessed, also the various implementation strategies. In section 1.4, the working philosophy of an ADS system is highlighted. The description of different components starting from the ion source front-end, through the accelerating part and till the beam reaching the target is made. The transmutation projects in the recent years which has regenerated the interest in ADS technology are summarized at the end. Advanced Gas-Cooled Accelerator-Driven Transmutation Experiment (AGATE) [AGATE, 2011] is one such project, for whose feasibility study, this report partly addresses the spallation target related issues. Section 1.5 has information on the design parameters of AGATE. In the final section 1.6 of chapter 1, literature survey is made on the works already completed. The research gaps are identified here and is used in the formulation of tasks that are necessary or have been well referenced.

Chapter 2 discusses the spallation process, which is main physics process under study in this work. Though this is not a new concept, with the advent of ADS systems and its practical realization of this process has evoked more interest than ever before. One of the most magnificent instance of spallation in nature happens when the cosmic-rays interact with the atmosphere. The evolution of spallation process from the high energy cascade reactions to the thermal ranges and the analytical expressions to describe quantitative neutron production as well as in spacial resolution have been enumerated here.

Design has been performed using monte carlo (MC) simulation. Given the numerous variables influencing the design, the analytical calculations can prove to be cumbersome. In such situations, MC methods come to the rescue. For this purpose, the toolkit Geant4 [Agostinelli et al., 2003] which incorporates MC methods has been used. It has applications in a broad range of areas such as high energy, nuclear and accelerator physics, as well as studies in medical and space science [Allison et al., 2006]. Chapter 3 introduces the toolkit itself and its functionalities. Appendix A contains the data of materials that have been used in the simulation.

It is important to understand the systematics involved with the interaction of projectiles with the matter. Through this, one can rationalize on the technical parameters to be set. In chapter 4, the systematics of projectile types and kinetic energies, target material and dimensions and particle production have been studied. Neutron leakage terms for targets made up of tungsten, mercury and lead have been quantified. Energy deposition behavior of the primary protons have been studied along with the contribution from other sources. This chapter draws proper argumentation for the choice of beam and target parameters that have been set for the AGATE concept.

The next chapters concentrate mainly on the design, radiation damage and radiological safety aspects of the target module. The beam extracted from the accelerator after being screened by detectors used to control the beam, reaches the target module. The beam may be intervened by the beam stop before this depending upon the operation circumstances. Unintervened, the first point of beam interaction is at the beam window. After minimal

distortion, the beam impinges on the target resulting in particle production. Hence target, beam window and beam stop are the three main components facing the beam directly and the beam-material interaction is studied here. Shielding is the other significant structure addressed in this work. In reference to this report, the term design deals exclusively to the the above components and shielding structure.

Chapter 5 develops with the selection of spallation target material, discussing the pros and cons. A basic model of the target (monolith) is studied for relevant entities, the shortcomings and the design requirements are implemented in the actual target model. The necessity arising due to the interaction of that target with the core and viable cooling has been kept in mind. The simulation results of the neutron and energy deposition profiles in and around the target have been depicted in chapter 6. Following this is the discussion on beam window and beam stop. The simulation results for the simplified model of these components have been discussed.

The intense radiation environment in the target module comprising of high energy hadrons is a plays a major role in the radiation induced effects. In order to asses the functional durability of the irradiated components, a measure of radiation damage is required along with gas production data. Chapter 7 quantifies both the damage and gas (helium) production in the target and the beam window.

Because spallation is associated with the production of radioactive nuclides and intense source of radiation, the report would be incomplete without mentioning the distribution of nuclide inventory and shielding measures that need to be taken in order to ensure the safe operation of the facility. Radiological safety aspects are included in chapter 8. More specifically, section 8.1 includes the nuclide inventory calculations. The radionuclides which contribute significant hazards in the operation environment, their implications on radiation protection are discussed. The decay characteristics of the long-lived nuclides, relevant for disposal are also elaborated. Section 8.2, deals with the radiation shielding measures, more in a qualitative way. The performance of shielding materials in terms of attenuating the radiation is illustrated.

All the major conclusions emerging as a result of this study are discussed in chapter 9. The present study has been undertaken under static conditions reserving a scope for further study of transient behavior of the target module. Outlook of this study and possible diversions that can be continued from the conclusions to address the unresolved agenda are summarized in the chapter.

1.3 Partitioning and Transmutation

1.3.1 Nuclear Waste Composition

Spent nuclear fuel is the source of nuclear waste. Figure 1.2 shows the nuclide distribution of SNF. Hazard from the SNF is mainly due to a few chemical elements – plutonium, neptunium, americium, curium (the latter three are classified as MAs) and some long-lived fission products such as iodine and technetium at concentration levels of grams per tonne and extended burn-ups or use of MOX fuel increases the amount of MAs produced [NEA, 2006]. Though the concentration of these nuclides are very minute in comparison to uranium, the hazardous nature stems from the fact that these nuclides have very long half-life and relatively higher radiotoxicity measured in Sv/Bq as shown in Table 1.1.

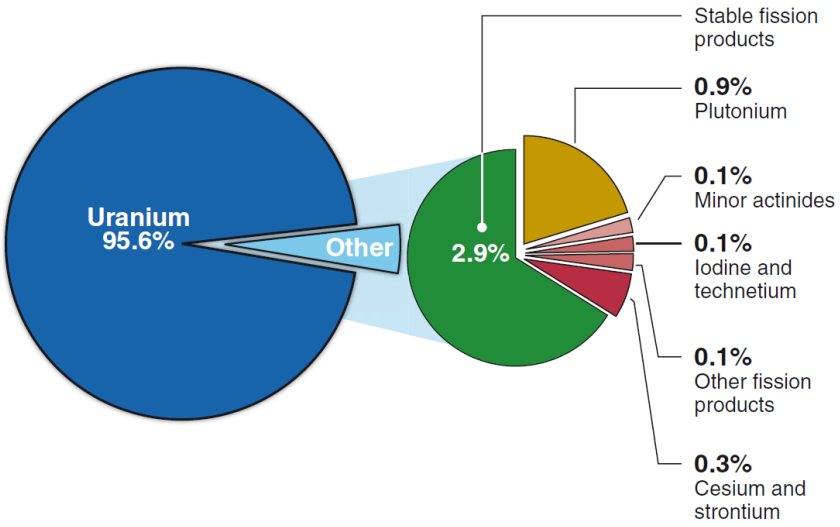

Figure 1.2: Composition of spent nuclear fuel [GAO, 2011]

Table 1.1: Radioactive characteristics of isotopes in spent nuclear fuel [NEA, 2006]

Nuclide	**Half-life**	**Specific activity**			**Dose coefficients**
	(years)	(Ci/g)	(W/g)	(Neutron min^{-1} mg^{-1})	(10^{-7} Sv/Bq)
^{237}Np	2.14×10^{6}	7.07×10^{-4}	2.07×10^{-5}	$< 7\times10^{-6}$	1.1
^{238}Pu	87.404	17.2	0.57	155	2.3
^{239}Pu	2.44×10^{4}	6.13×10^{-2}	1.91×10^{-3}	1.35×10^{-3}	2.5
^{240}Pu	6580	0.227	7.1×10^{-3}	53.7	2.5
^{241}Pu	14.98	99.1	4.06×10^{-3}		4.7
^{242}Pu	3.87×10^{5}	3.82×10^{-3}	1.13×10^{-4}	95.3	2.4
^{241}Am	432.7	3.43	0.1145	3.55×10^{-2}	2
^{242m}Am	144	10.3	3.08×10^{-2}		1.9
^{243}Am	7370	0.2	6.42×10^{-3}		2
^{242}Cm	0.445	3.32×10^{3}	122	1.21×10^{6}	0.13
^{244}Cm	18.099	80.94	2.832	6.87×10^{-5}	1.6
^{245}Cm	8 265	0.177	5.89×10^{-3}		3
^{252}Cf	2.64	537	38.3	2.3×10^{12}	0.98

1.3.2 Argument for Partitioning and Transmutation

Figure 1.3 shows the radiotoxicity evolution of LWR (UO_2) fuel at a burn-up of 50 GW·d/t HM. The different evolution scenarios of radiotoxicity has been compared to a reference level of 7.83 t uranium and its equilibrium products originally used to produce energy. As it can be seen from the figure, for the case of open cycle where the spent fuel is sent directly to long term storage without any kind of treatment, the total radiotoxicity of the spent fuel reaches the reference level in 130,000 years. In the first few years, radiotoxicity and heat emission is dominated by the fission products ^{137}Cs and ^{90}Sr. Actinides like plutonium, americium and curium isotopes are the main contributors to radiotoxicity later on until several thousands of years.

Given the continuous generation of nuclear power, repositories of the size of Yucca Mountain needs to be constructed every seven to ten years world wide for the nuclear waste stream disposal. Adding to the woe is the fact that the engineering barrier confining radiotoxic materials is insecure beyond 10,000 years implying higher probability of migration of long-lived radionuclides outside of the barrier and contaminating the biosphere as actinides remain influential even beyond 10,000 years. This situation calls for implementing P&T strategies to reduce radiotoxicity of actinide inventory by a factor of 100 or more in order to bridge the time needed to reduce radiotoxicity to the reference level.

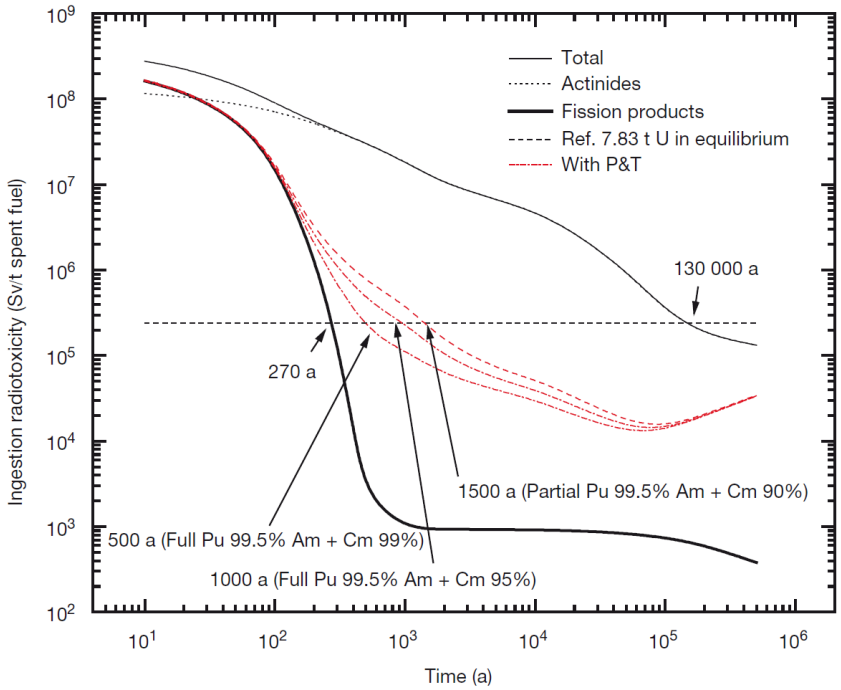

Figure 1.3: Ingestion radiotoxicity of 1 ton of spent nuclear fuel [IAEA, 2004]

The radiotoxicity evolution after P&T process with different efficiencies (full and partial multiple recycling of plutonium as well as americium and curium) have been depicted in figure 1.3 leading to the conclusion that P&T helps to reduce the time during which nuclear waste should be isolated from the biosphere from 130,000 years to between 500 and 1,500 years. Reference [IAEA, 2004] enumerates the main goals of P&T as:

- A reduction of the hazard associated with spent fuel over the medium and long term (>300 years) by a significant reduction of the inventory of plutonium and MAs.

- A reduction of the time interval required to reach a reference level of radiotoxicity inventory by recycling transuranic elements (TRUs).
- A decrease of the spent fuel volume by separation of uranium to enable more efficient storage or disposal.

1.3.3 Principle of Transmutation

As discussed in the previous sections, TRUs in the spent nuclear fuel are the major contributors to radiotoxicity. Separation of TRUs from the waste stream is achieved through partitioning. Then, nuclear fission is used in the transmutation of TRUs into short-lived or stable nuclides using neutrons [NEA, 2006]. Figure 1.4 illustrates the effectiveness of transmutation in reducing the overall radiotoxicity of the system. For example, ^{245}Cm with half-life of 8500 years is fissioned using a neutron. The fission products ^{100}Pd is stable and ^{134}Cs has a comparatively shorter half-life of two years.

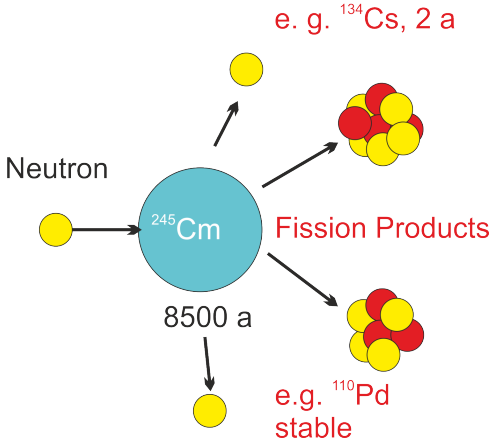

Figure 1.4: Transmutation of ^{245}Cm isotope using neutron

Figure 1.5 illustrates the ratio of fission-to-capture cross sections (normalized) for some TRUs upon neutron incidence. It depicts the competition between the fission and capture processes. In the thermal energy region, the fission-to-capture cross section is low. It increases dramatically after about 100 keV by several orders of magnitude for all the three isotopes. The observation holds true for all actinides including the fissile isotopes [Herrera-Martínez, 2004].

The lower fissile-to-capture ratio implies that transmutation in a thermal reactor is hampered by lower neutron economy. Other actinide species are created instead of the radionuclides being transmuted due to neutron capture reactions. In order to efficiently transmute actinides, a harder neutron spectrum is required which can be realized in fast reactors or in ADS.

1.3.4 Implementation Strategies for Transmutation

Fast Reactors

Fast critical reactors offer the hard neutron spectrum necessitated by the transmutation process. Loading fast reactors with fuel containing appreciable amounts of MAs compromises the safety parameters. The small delayed neutron fractions and undesirable

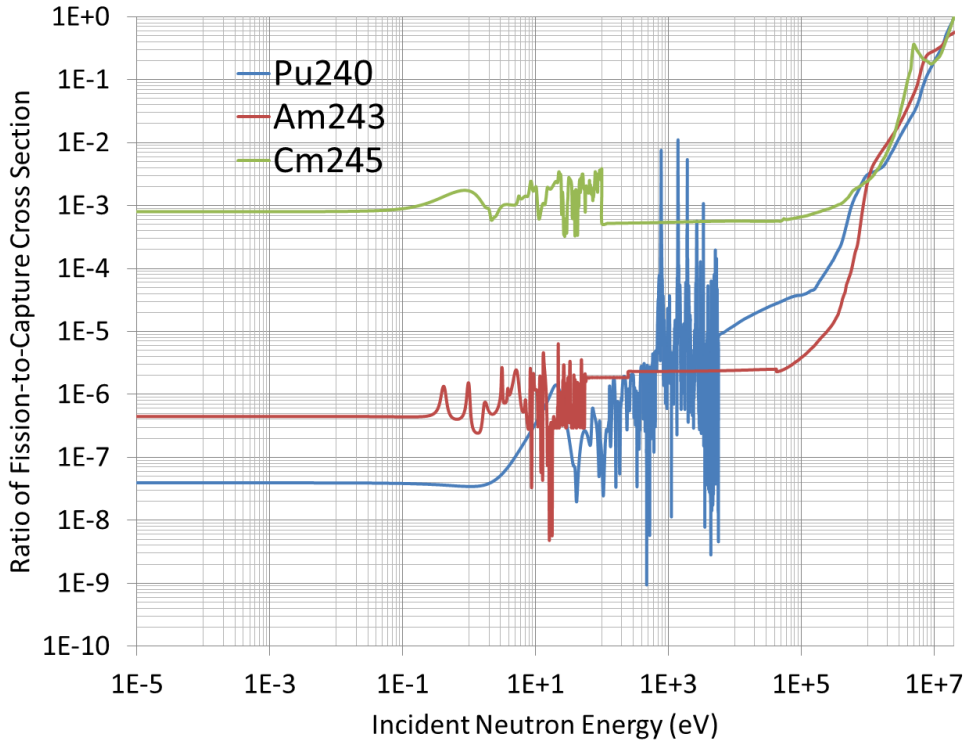

Figure 1.5: Ratio of fission-to-capture cross section for ^{240}Pu, ^{243}Am and ^{245}Cm

reactivity coefficients negatively influence the control of reactor by reducing the reactor period. Thus, fast systems are not feasible for transmutation of nuclear waste composed of MAs.

Accelerator Driven Systems

To offset the safety problems introduced by MAs in a critical reactor, a sub-critical reactor is more favorable for the purpose of transmutation. A sub-critical system is driven by an external neutron source, the ADS. High energy protons induce spallation process in a target of heavy material producing significant amount of fast neutrons. Direct usage of these neutrons is economically not viable due to the high cost of accelerator. Coupling the spallation target to a sub-critical core loaded with fuel containing MAs is reasonable as the spallation neutrons are multiplied in the sub-critical core through fission.

Accelerator-Driven Sub-Critical System (ADSS) offers substantial flexibility in overall operation while ensuring safe and efficient means of transmutation.

1.4 Accelerator-Driven System

1.4.1 Components of ADS

The advent of particle accelerators in the field of physics has opened up myriad of nuclear applications. These applications can range from material irradiation studies, isotope production, neutron sources, and transmutation of nuclear wastes or power production. Currently there are a handful of facilities around the world running high energy proton accelerators accommodating state-of-the-art devices like linear accelerator (linac) with

super conducting modules or cyclotron which can accelerate the protons close to relativistic energies. Negatively charged hydrogen ions (H^-) that are derived from an ion source are injected into the accelerating units. The ions are stripped of their electrons as they accelerate in the beam line as protons. Once the desired energy of the beam is reached, the protons are extracted from the accelerator to be delivered into the spallation target module.

H^- Ion Source

Ion source refers to the device producing ions combined with a beam forming and pre-acceleration apparatus. Radio frequency (RF) radiation is used to ionize the gas in the ion source to form gas plasma [Mauro, 2009]. As the kinetic energy of the H^- particles from ion source is about a few tens of keV, it is accelerated before being injected into linac. These particles are accelerated by a pre-injector using RF quadrupole because of its higher energy (several MeV) and a much smaller physical size added with higher beam brightness .

Linac

Linacs enable to accelerate H^- beam to full energy and at high currents. Particle velocity changes over a wide range during the acceleration and based on this, the linac is partitioned into low, medium and high energy parts [Chou, 2003].

Low energy part (below 100 MeV): Every proton linac in the world uses drift tube linac (DTL) for acceleration in this energy region. Drift tubes are equipped with permanent magnet quadrupoles (PMQs), used as focusing elements. PMQs can be accommodated compactly at medium magnetic gradients as they do not need current supply wires or power converters. The DTL cavities consist of a steel cavity, an aluminum girder, drift tubes assembled from pre-machined copper pieces, and accessories for mounting drift tubes in girders as well as for tuning, stabilization, support, vacuum pumping and alignment of the structures (figure 1.6).

Figure 1.6: DTL prototype in assembly stage [Mauro, 2009]

Medium energy part (100 MeV - 1 GeV): Cell-Coupled Drift Tube Linac (CCDTL)

technology has been used in all existing linacs. The highest energy using this technology reaches 800 MeV (LANSCE at Los Alamos). CCDTL is made of DTL-like accelerating tanks, connected by off-axis coupling cells bridging the focusing quadrupoles.

High energy part (above 1 GeV): Speed of particles in this energy range is comparable to the speed of light. Super conducting (SC) linac is the only economically viable option.

Cyclotron

As an alternative to expensive SC linacs, cyclotrons can be used to accelerate particles up to a few MW beam energy [IAEA, 2004]. Cyclotrons operate in continuous wave (CW) mode. The swiss spallation neutron source (SINQ) is driven by the ring cyclotron (figure 1.7) at Paul Scherrer Institute (PSI), Switzerland.

Theory of electrodynamics is applied in cyclotrons to produce particles of reasonably high energy in a relatively confined space [IAEA, 2008a]. The magnetic field in the acceleration chamber of the cyclotron causes particles to travel in circular orbits. Ions produced in an ion source at the center are accelerated out from the center by a high frequency electric field through two or more hollow electrodes called 'dees'. As the particles are accelerated, they pass from one dee to the next through a gap between the dees. A practical limit on the energy of the accelerated particle is reached on the basis of the magnet's diameter. This is due to the fact that the rotational frequency of the particles remain constant as the energy of the particles increases, the diameter of the orbit increases until the particle can be extracted from the outer edge of the machine.

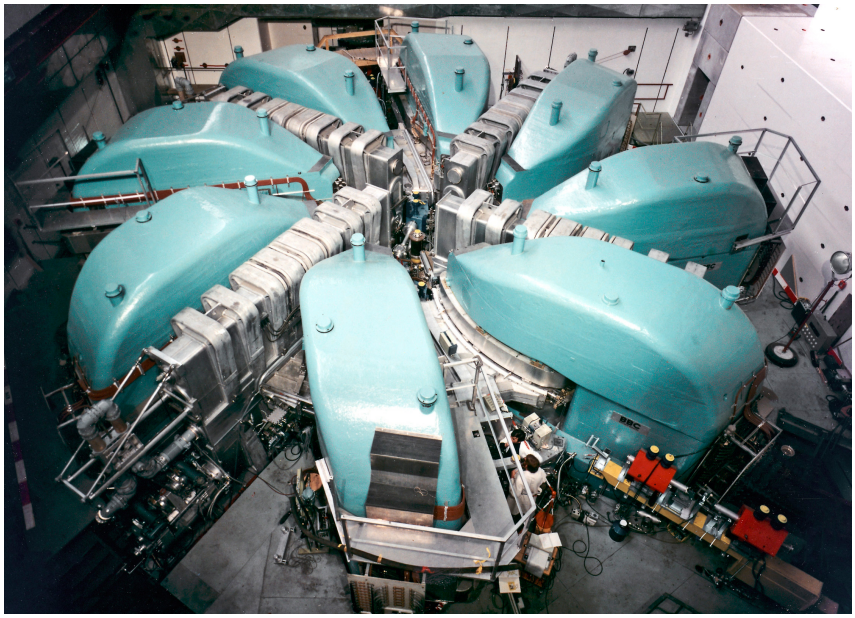

Figure 1.7: The 590 MeV ring cyclotron at PSI [SINQ, 2012]

Spallation Target Module

Design of the spallation target module is the interest of this work. It forms the interface between the accelerator and the sub-critical core in an ADS driven transmutation system [Satyamurthy et al., 2007]. The main purpose of incorporating an ADS system is realized here, i.e., the production of neutrons. High power beam of protons is received by the STM and is converted to neutrons in the spallation target which is then supplied to the

sub-critical core for multiplication. Pressurized gas or liquid is used as a coolant. PBW separates the pressurized STM from the accelerator vacuum. Several layers of biological shielding around the target serves for radiation protection.

Spallation Target Spallation target occupies the core of STM [NEA, 2005]. Materials of high mass number is preferred in order to maximize neutron yield [Carpenter, 1977]. Tungsten, lead and mercury are some of the materials used in their elemental form. A detailed discussion on the ideal properties and selection of material is elaborated in section 4.2.1. Interaction of high energy protons in a spallation target is a series of cascade reactions [Goldenbaum, 2003], eventually producing neutrons. Current understanding of spallation from various literatures is delved into detail in chapter 2 dedicated entirely to spallation physics.

Proton Beam Window Proton beam window acts as the interface between the vacuum region of proton beamline and high pressure region of STM. It avoids the diffusion of gaseous and volatile nuclides, some of which are radiotoxic from the target region to the beam-line region. Since the spallation target is irradiated outside beamline vacuum, therefore no breaking of the vacuum and pumping down afterwards is required when exchanging the targets simplifying target transfer and also significantly reducing beam-off time between successive irradiations [Hilscher et al., 2001]. Low mass number materials are chosen in order to minimize beam interaction with PBW. Section 6.2.1 has more to do on this topic.

Biological Shielding Section 1.3.3 points out the necessity of applying a hard neutron spectrum to transmute MAs. High energy neutrons impose stringent shielding requirements. The biological shield itself consists typically of a single or multi-layer combination of iron followed by concrete to keep the occupational dose for the personnel below the stipulated values by various regulatory agencies [Lindenbaum, 1961]. Design of the biological shielding and its implication on radiation safety follows in section 8.2.

Proton Beam Stop Though beam stop is not a part of the STM, it interacts directly with the beam like the spallation target but for a different purpose. A beam stop can be used to interrupt the charged particles and completely absorb the beam in case there is a failure of accelerating components. The part of the beam leaves the target without interaction is intercepted by beam stop, designed to handle any damage to other structural components which otherwise could have been caused. Section 6.2.2 evaluates the performance of a simple graphite beam stop.

Other Components

Beam current and position monitors, beam focusing devices, beam bending devices and devices that limit beam size and protect equipment forms the beam delivery system [NCRP, 2003]. A magnet is used to bend the beam to a new direction, acting much like a prism for light. Collimators are placed where the beam loss is most likely, i.e. where the points of big divergence from the optimum orbit and where sensitive equipment is located, for example near the current monitors.

The main auxiliary systems of the particle accelerators are high-voltage systems, micro-wave power systems, cooling systems and vacuum systems. Klystrons are microwave

power amplifiers used to generate the RF accelerating fields required for accelerators. Other auxiliary components include cooling and filtration systems to ensure smooth circulation of coolants, and suitable ventilations to vent out the radioactive and other gases, some of which may be chemically reactive or toxic, or even flammable or explosive (like H_2).

1.4.2 ADS Transmutation Programs

There are many P&T concepts that are being proposed or under investigation [NEA, 1994, Blomgren et al., 2010] at many organizations in the world, some of the ADS based transmutation programs are discussed below.

Transmutation Experimental Facility

Transmutation Experimental Facility (TEF) in Japan is composed of two experimental facilities, Transmutation Physics Experimental Facility (TEF-P) and ADS Target Test Facility (TEF-T) [TEF, 2012]. Physical and dynamic properties of ADS is studied in TEF-P at low power (10W) proton beam. TEF-P is equipped with a critical assembly to be loaded with uranium and TRUs. Liquid lead-bismuth spallation target installed in the TEF-T is irradiated by 600MeV-200kW proton beam. TEF-T is a facility to examine the experiments for material and thermo-hydraulics. The proton beam required by the facility is delivered from the Japanese Proton Accelerator Research Complex (J-PRAC) linac.

Accelerator Transmutation of Waste

Los Alamos has been studying transmutation under Accelerator Transmutation of Waste (ATW) program based on ADS since a decade [ATW, 2012, Beller et al., 2001]. A high energy, high current linac designed for the Accelerator Production of Tritium facility and since then much development has been completed. Both critical reactors and sub-critical accelerator driven reactors are being considered with the fuel/blanket options of molten salt thermal systems, liquid-metal cooled fast reactors (Na, Pb, or Pb-Bi), and gas cooled systems. While spallation target options include gas cooled tungsten, integral lead-bismuth target and others. In order to realize a hard spectrum, liquid metal is chosen as a coolant either sodium (reference coolant) because of extensive international experience or liquid lead–bismuth (preferred coolant) because of significant advantages over sodium as both a spallation target and as a coolant.

Multi-purpose Hybrid Research Reactor for High-tech Applications

Multi-purpose Hybrid Research Reactor for High-tech Applications (MYRRHA) is a multipurpose ADS for R&D [MYRRHA, 2012, Abderrahim et al., 2001] under development in Mol at the Belgian Nuclear Research Center SCK·CEN. It focuses primarily on research of structural materials, nuclear fuel, liquid metals and associated aspects, on sub-critical reactor physics and subsequently on applications such as nuclear waste transmutation, radioisotope production and safety research on sub-critical systems. It consists of a proton accelerator delivering 600 MeV-2.5 mA to a liquid lead-bismuth spallation target coupled to a lead-bismuth cooled, sub-critical fast nuclear core. MYRRHA has no PBW between the lead-bismuth free surface and the beam, an example of windowless design, in order to

minimize engineering difficulties and reduce energy losses . Other than the multipurpose nature of this program, one of the aims is to serve as a basis for the European ADS (eXperimental demonstration of Transmutation in an ADS). The project which started in 1997, is ambitious to have MYRRHA fully operational around 2022-2023.

1.5 Advanced Gas-cooled Accelerator-driven Transmutation Experiment

Under the European Commission's 6th Framework Program (FP6),the European Research Program for the Transmutation of High-Level Nuclear Waste in an ADS (EUROTRANS) was set up [IAEA, 2009]. The aim of EUROTRANS was to develop a concept for treating large amounts of plutonium, uranium and MAs (P&T), and to construct test facilities for the production of suitable fuels for future transmutation systems (industrial use). The two concepts that served as the objective of EUROTRANS were: Experimental ADS (XT-ADS) and European Facility for Industrial Transmutation (EFIT). Both concepts involved a spallation target made of liquid metal. While XT-ADS was designed for MOX fuel, which was to be accommodated in different loading zones, the EFIT concept was designed for the use of uranium-free fuels but with plutonium and minor actinides. Both designs were intended for an efficient and powerful superconducting proton linear accelerator. In XT-ADS, a liquid lead-bismuth eutectic (LBE) was used as a coolant, while liquid lead was used in EFIT. A helium-cooled variant, He-EFIT, was proposed and investigated as an alternative to the lead-cooled EFIT concept with solid tungsten as the target.

Initially, the focus of EUROTRANS was split between a gas-cooled ADS and an ADS cooled by heavy metal. However, as the project progressed, the partners involved began to concentrate more and more on the ADS concept with heavy-metal cooling (lead/lead-bismuth) for XT-ADS. However, the gas-cooled concept was considered as a back-up for EFIT. In order to diminish the discrepancy between science and technology (gas to heavy-metal cooling), the concept of a gas-cooled accelerator-driven transmutation experiment, AGATE [AGATE, 2011] was prepared. The aim of this study is to identify the opportunities and risks associated with P&T. And also to outline the necessary steps and the prerequisites for future R&D work on the components of a transmutation system. Advanced Gas-cooled Accelerator-driven Transmutation Experiment (AGATE) is a facility to demonstrate the concept of transmutation being investigated by the Institute of Nuclear Fuel Cycle (RWTH-Aachen), the Research Center Jülich (FZJ), the Frankfurt Institute for Advanced Studies (FIAS) and the SIEMENS company.

The gas-cooled system has a number of advantages over other ADS concepts:

- fewer corrosion problems
- higher burnup efficiency
- easier handling of the fuel elements
- no activation of the coolant (helium)
- easier inspection and repair

While, the disadvantages are low thermal capacity and high operating pressure.

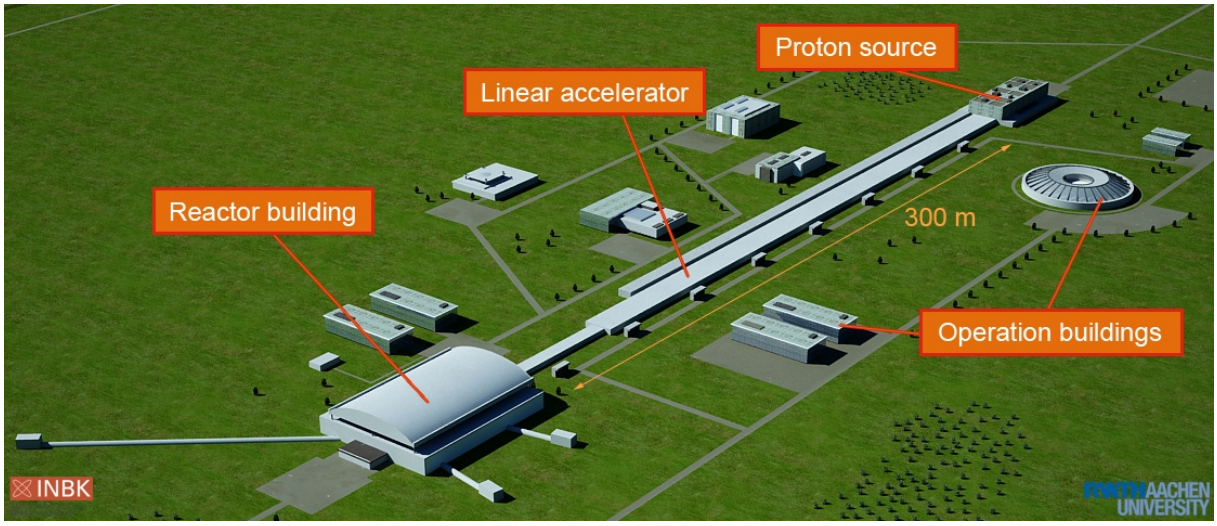

Figure 1.8: Virtual layout of the AGATE complex [AGATE, 2011]

The most important parameters are listed in table 1.2. In-line with the XT-ADS design, the source protons have 600 MeV kinetic energy being delivered by the SC linac. The proton current depends upon the sub-critical core configurations such as the fuel composition, multiplication factor and reactor geometry and a maximum up to 10 mA. The preferred mode of accelerator is CW so as to increase transmutation efficiency.

To summarize the design parameters extracted from the table related to STM are as follows. Plates (segments) of tungsten shall be used as the target. The total length of the target (including the gaps between the plates) shall be 1200 mm. This criteria has been set in order to homogeneously illuminate the fuel elements in the sub-critical core corresponding to a length of about 1500 mm. Helium is used to cool the target. The preferred material for PBW is wrought aluminum alloy cooled by water. Concept of different plates (pebble bed/perforated sheets/wires) and energy deposition parameters are derived after the design calculations presented in chapter 5.

This work is dedicated to compliment AGATE feasibility study by addressing the issues related to the STM especially the target design. Neutron production and energy deposition behavior in the target, PBW and beam stop are also investigated for each of the components individually. Then, the radiation protection aspects, i.e, activation and shielding studies are performed for STM. Finally, the radiation damage is calculated in the target and the PBW.

1.6 Literature Survey

1.6.1 Spallation Neutron Sources

Some of the existing spallation neutron sources [Gardner, 1998, NIST, 2012] are listed in table 1.3 ([SNS, 2012, KENS, 2004, Goldstone, 1991, LNSC, 2012, ISIS, 2012, SINQ, 2012]) along with their main parameters. Some neutron sources such as the IPNS in Argonne National Laboratory has already been shutdown after a long history of operation [IPNS, 2012]. Given the significance of spallation neutron sources in this era, many of the proposed ones are in the pipeline, for instance, the ambitious European Spallation Source with 5 MW beam power [ESS, 2012]. The vast pool of technical expertise built over the

Table 1.2: List of main parameters of the AGATE concept [AGATE, 2011]

Parameter	**Material/Value**
Accelerator	
Maximum beam power of the proton accelerator	6 MW
Preferred accelerator type	Superconducting linear accelerator
Energy of the protons with the linac	600 MeV
Maximum beam current with the linac	10 mA
Accelerator mode	Continuous wave (CW)
Alternative accelerator type	Two-stage cyclotron
Energy of the protons with the cyclotron	1 GeV
Maximum beam current with the cyclotron	6 mA
Proton window and spallation target	
Material of the proton beam window	Wrought aluminum alloy
Coolant for the proton beam window	Water
Design of max. heat deposition in the beam window	25 kW
Length of the spallation target	1200 mm
Type of spallation target	Segmented plate target
Material of the spallation plates	Tungsten
Concepts for the plates	Pebble bed/perforated sheets/wires
Energy deposition at a beam power of 6 MW	4.37 MW
Coolant for the spallation target	He
Sub-critical reactor	
Coolant for the reactor	He
Maximum thermal power of the reactor	100 MW
Fuel for the pilot phase	MOX
Plutonium fraction	$\leq$ 20 %
Total mass MOX fuel	4.25 t
Multiplication factor - k_{eff} (MOX)	0.95 - 0.97
Fuel for the transmutation phase	Innovative MA fuel
Multiplication factor - k_{eff} (MA)	0.9
Cladding material	HT-9
Gas pressure in the reactor	6 MPa
Active fuel element length	1500 mm
Pitch of the fuel rods	10 mm
Number of fuel rods	10374
Number of fuel elements	114
Structure of the fuel elements	Hexagonal
Radius of the fuel rod	3 mm
Inner radius of the cladding tube	3.05 mm
Outer radius of the cladding tube	3.55 mm

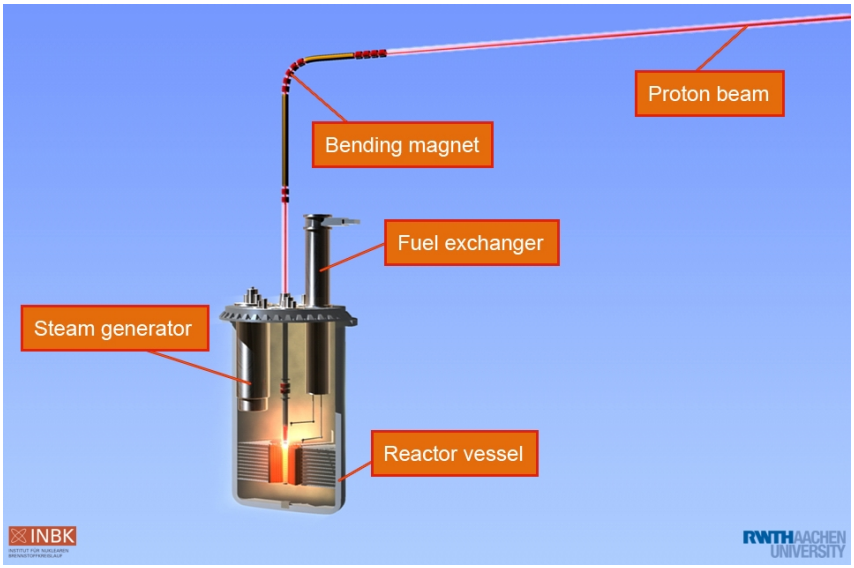

Figure 1.9: Virtual layout of the AGATE reactor [AGATE, 2011]

years in this regard, offers a rich resource of literature.

Table 1.3: Main parameters of some existing spallation neutron sources

	SNS Oak Ridge	**KENS** Japan	**LNSC** Los Alamos	**ISIS** Oxford	**SINQ** Villigen
Accelerator	Linac	Linac	Linac	Linac	Cyclotron
Proton kinetic energy	1.0 GeV	500 MeV	800 MeV	800 MeV	590 MeV
Average beam current	1.4 mA	10 μA	80 μA	200 μA	2.3 mA
Pulse repetition rate (Hz)	60	20	20	50	CW
Proton beam power	1.4 MW	5 kW	64 kW	160 kW	1.36 MW
Target Material	Hg	W (Ta Clad)	W	W (Ta Clad)	Pb Rods (in Zircaloy Tubes)
In Operation since	2006	1980	1985	1984	1996

1.6.2 Systematics of Spallation Reaction

From table 1.3, it can be seen that the different spallation sources use different materials for targets viz., lead, tungsten and mercury. Lead-bismuth was employed in the MEGAwatt PIlot Experiment(MEGAPIE) target [Latge et al., 2006], uranium had been used at ISIS [Watanabe, 1999], lead-gold eutectic (LGE) has been proposed as an alternative target material for high power spallation sources [Medarde et al., 2011] and lead-tin alloy was considered for the ultra-cold neutron source at PSI [Atchison et al., 2005]. Probably, there are some more materials that have not been considered as candidates for spallation material. In order to weigh the prospects of the different spallation materials, a comprehensive systematics study of possible candidate materials is done in sections 4.2.1, 4.3 and 4.4. This study is extended to investigate neutron production and energy deposition behavior in the target. Understanding these systematics will refine the selection criteria of spallation materials.

Neutron emission data due to interaction of relativistic ions, both light and heavy [Yurevich, 2009, Fasil'kov et al., 1995, Yurevich et al., 2006] in spallation target materials for various energies [Ledoux et al., 1999, Trebukhovsky et al., 2005, Leray et al., 2002, Dementyev et al., 1996, Amian et al., 1993] and target radii [Letourneau et al., 2000] are measured in some experiments. These experiments help to arrive at the logic of the most appropriate choice of projectile, its energy and target dimension within the technical limitations. In his paper [Watanabe, 2003], Watanabe also provides arguments from the physical point of view complimenting the experiments. Geant4 simulations of these experiments are presented in sections 4.1.1, 4.1.2 and 4.2.2 respectively. Comparing the calculations against the experimental values is a way to benchmark Geant4 toolkit and its physics implementations. This instills confidence in applying the toolkit for further independent simulations. More importantly, the simulations provide a platform where design parameters can be optimized for the AGATE system. Some instances where Geant4 is used for simulation are viz., in proton extraction and transfer line at TRIUMF [Jones et al., 2009], neutron interrogation project [Canada, 2007], target optimization studies for ESS [Bungau et al., 2010], ISIS [Bungau et al., 2009] and ADS for transmutation [Bungau et al., 2008] and at Large Hadron Collider (LHC) [Heikkinen, 2009].

1.6.3 Spallation Target Design

Bauer has done extensive study of spallation targets [Bauer, 2010, Bauer, 2005]. He reports about liquid and different forms of solid targets, viz., plate, rod and rotating types. General aspects like neutron yield and angular distribution, radiation damage effects, power distribution in the target are elaborately looked into. Operational experiences of MW-class targets is documented in [Haines et al., 2011]. AGATE employs a solid tungsten target for neutron production. Energy deposition is often a problem in solid targets and as shown later in section 6.1.1, for MW power beam, high power density in the target makes cooling of a monolithic block of tungsten unfeasible. Hence, tungsten has to be split into segments [Russell et al., 1997]. Added advantage of a segmented tungsten target is that the parasitic absorption of neutrons is reduced [Russell et al., 1995]. Thermo-hydraulic performance of tungsten target is analyzed in [Ammerman et al.,] and innovative concept of target arrangement is developed. The target discussed so far produces neutrons in a compact spatial dimension. Such a target works well for a spallation neutron source as the main application is neutron scattering [Carpenter, 1977]. For implementing the target in an ADSS, modification in the target design is required to illuminate the fuel elements in the sub-critical core to ensure safety conditions. Design of an elongated tungsten target to produce an axially homogeneous distribution of neutrons is the main goal of this work. This target finds a significant role in an accelerator driven subcritical transmutation system.

Jansen has studied possible PBW materials and several PBW forms for an accelerator driven transmutation system in 1995 [Jansen, 1995]. He has also analytically derived the thermal properties and radiation damages in PBW. Since then, the understanding of spallation physics has evolved tremendously and monte carlo has taken over the cumbersome analytical approach. In a more recent reference of a PBW for high current densities as a part of ESS study [Butzek et al., 2003], basic design concepts have been developed. A particular design from this study has been investigated for energy deposition phenomenon, activation and radiation damage respectively in sections 6.2.1, 8.1.2 and 7.3.2. Whereas beam stop design has been covered in [Polsky et al., 2010, Murdoch et al., 2003,

Kim et al., 2006, Enparantza et al., 2010]. Based on the recommendations of the references, a basic model of a beam stop has been analyzed to asses neutron production and energy deposition in section 6.2.2.

1.6.4 Radiation Damage

Robinson [Robinson, 1994] uses an elementary approach to explain radiation damage production. He arrives at the damage energy "ansatz" based on LSS theory, other than explaining the production of energetic atomic recoils due to various nuclear processes. Gas production in the target also induces radiation damage effects [Watanabe, 1999]. There are many literatures available, discussing the radiation damage phenomenon in an ADS facility [Ullmaier and Carsughi, 1995, Wechsler and Sommer, 1984, Wechsler et al., 1997, Mansur and Coghlan, 1983, Green et al., 1988]. Resources providing displacement cross sections [Broeders and Konobeyev, 2005, Broeders et al., 2005] and calculated damage values [Green, 1984] are available. Often such resources are limited only for some materials and/or under particular irradiation condition. To overcome this limitation, a very general method [Norgett et al., 1975] has been implemented via Geant4 toolkit to quantify radiation damage values. This approach is very general and more reasonable as radiation damage can be calculated for the materials of choice and under irradiation condition as designated for AGATE concept.

1.6.5 Activation and Radiation Shielding

Interaction of high energy protons with the target results in the production of particle and spallation products in situ [Stankovsky et al., 2001, Gollon, 1976]. On-line identification of some nuclides in spallation products in the target is formidable because of their transient nature viz., radioactive decay or neutron capture reactions. Inverse-kinematic techniques for measurement of isotopic yields facilitate the identification of primary residues (spallation product) reactions [Enqvist et al., 2001, Schmidt et al.,]. Particle activation of spallation products and target material leads to induced activity [Wladyslaw and Pohorecki, 2006]. The activation products pose radiological protection concerns [Artisyuk et al., 2002], hence it is important to identify the nuclide vectors of relevant radionuclides and their implications (section 8.1).

Several studies regarding the shielding of high energy accelerators are available as references [Lindenbaum, 1961, Seltborg et al., 2005, Kato and Nakamura, 2001]. The angular dependence of energetic neutrons [Bauer, 2001] make radiation shielding calculations in an ADS very challenging. Different materials have been used in single-layered or multi-layered configurations [Hanslik, 2006], all in order to reduce the space occupied by shielding structures while ensuring effective biological protection. Koprivnikar has analyzed some compact shielding models [Koprivnikar and Schachinger, 2002] to shield against neutrons. While most of the shielding studies are done with neutrons in mind, there is hardly any literature on shielding against gammas in proton ADS. Given the occurrence of high energy gammas in spallation sources [Koprivnikar, 2001], this is a major shortcoming with respect to shielding analysis. Structures composed of borated materials are often attractive to reduce the shielding dimensions [Khripunov et al., 1997] and calculations for such structures are also rarely available. Study presented in section 8.2 on radiation shielding tries to fill these gaps, thereby reviewing shielding additionally for gammas and exploring borated material options for shielding structures.

CHAPTER 2

Physics Principles of Spallation Reactions

Nuclear Physics Academic press defines spallation as [Goldenbaum, 2003]:"a type of nuclear reaction in which the high-energy level of incident particles causes the nucleus to eject more than three particles, thus changing both its mass number and its atomic number." About 20 neutrons are created per incident GeV proton. As late as 1933, the high multiplicities of cascade particles produced were observed in nuclear reactions induced by light relativistic projectiles using cosmic rays [Benlliure, 2006]. With the development of high energy particle accelerators, the spallation reactions were discovered in the context of ADS at Berkeley in 1947 using a cyclotron [Krása, 2010]. The term "spallation" was coined by W. H. Sullivan and G. T. Seaborg in the same year.

The versatile nature of spallation reactions makes its accurate definition difficult. Rather, general observations of high energy proton interaction with matter viz., neutron multiplicities, fragments of residues and energy characteristics are summed-up. The typical case of central collision (deep spallation) of a proton with a target nucleus can be imagined from the illustration in figure 2.1. The nucleons from a target nucleus are "spalled" or knocked-out due to the bombardment of an energetic proton, leaving behind fragments whose mass number and atomic number is smaller than the target nucleus itself.

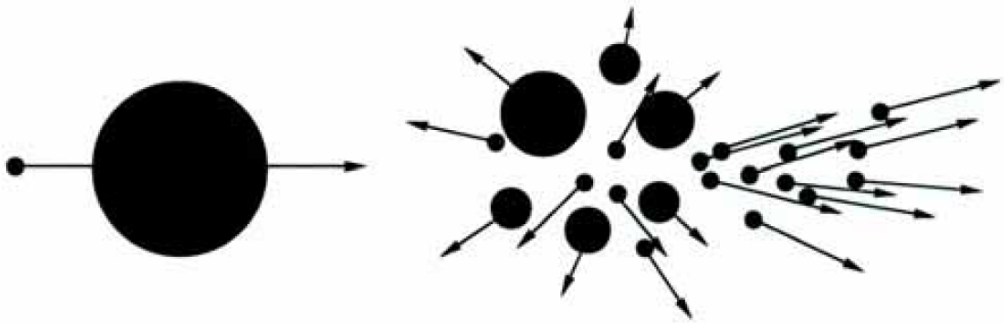

Figure 2.1: Illustration of spallation reaction

2.1 Mechanism of Spallation Reactions

Serber is the first one to come up with the theoretical description of spallation mechanism [Serber, 1947]. He proposed a two stage model, intra-nuclear cascade (INC) followed by

statistical de-excitation. According to this theory, the first step is regarded in terms of collisions between the incident particle and the individual nuclear particles, i.e., nucleon-nucleon collisions.

2.1.1 Intra-Nuclear Cascade

INC models are practically the only available tools to model hadron-nucleus interactions in the energy range from the pion production threshold (about 200 MeV) to high energies. The classical codes implementing this model are Bertini, INCL4, ISABEL [Shetty, 2010] and BIC. For hadron multiple collision processes in nuclei, the mentioned codes assume target to be a cold Fermi gas of nucleons in their potential well. Free hadron-nucleon cross sections are used to calculate the hadron-nucleus cross sections during collisions. Possible hadrons are limited to protons, neutrons and pions. Fermi motion is taken into account to compute the interaction cross section and to produce the final state of particles.

The wavelength of hadron motion must be much shorter than the hadron mean free path inside the target nucleus. To satisfy this condition, the projectile nucleon should have at least 200 MeV. The basic assumptions of a general INC model according to the lecture notes of Ferrari and Sala [Ferrari and Sala, 1996] are:

- Hadrons propagate like free particles in the nuclear medium under the influence of Fermi motion and local nuclear density.
- Classical approach is used to model the particle motion which can be subjected to an average nuclear mean potential.
- The nuclear mean field may result in curved trajectories of particle motion, according to energy and momentum conservation.
- Center of Mass System describes the collision of two hadrons.
- Interactions occur in a completely incoherent and uncorrelated way.
- Quantum effects are mainly limited to Pauli blocking.
- Secondaries are treated exactly like primary particles, with the exception that they start their trajectory inside the nucleus.

Scattering experiments with nucleons on nuclei have shown that the depth of the potential well is about 30 MeV and the minimum energy to eject a neutron is about 8 MeV (binding energy) [Nabbi, 1979]. For protons, the binding energy is greater than that for neutrons due to the Coulomb barrier, which makes neutron emission more probable. Fermi level is related to the binding energy of nucleons in a nucleus as shown in figure 2.2.

The Fermi level for protons ($E_f(protons)$) and neutrons ($E_f(neutrons)$) are given by the following relations:

$$E_f(protons) = 53(Z/A)^{2/3} MeV \tag{2.1}$$

$$E_f(neutrons) = 53\left[(A-Z)/A\right]^{2/3} MeV \tag{2.2}$$

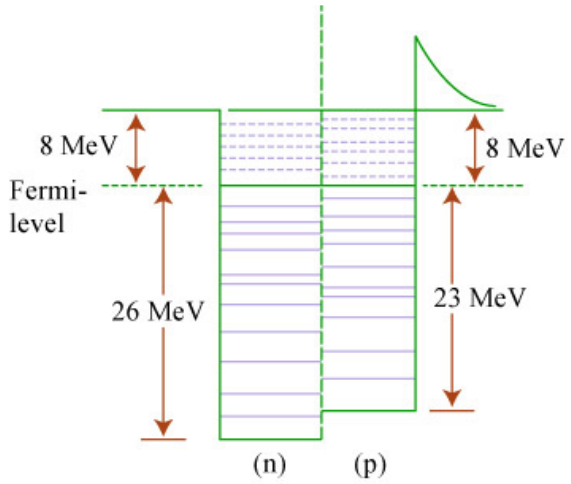

Figure 2.2: Nuclear potential wells for neutrons and protons according to the Fermi-gas model [MIT, 2012]

where A and Z are respectively the mass and atomic numbers.

The cascade build-up in the nuclear material is mapped according to the mean-free-path ($\lambda_{p,E}$) for a proton (p) of given energy (E) as:

$$\lambda_{p,E} = \frac{4\pi}{3} R^3 \left[(A-Z)\sigma_{np,E} + Z\sigma_{pp,E}\right]^{-1} \tag{2.3}$$

where R is the radius of the nucleus and $\sigma_{np,E}, \sigma_{pp,E}$ are the free hadron-nucleus cross sections (see figure 2.3).

Hadronic Cascades

The result of INC is a forward-directed component of high energy hadrons. For sufficiently thick targets, i.e, thickness much longer than the nuclear mean free path of the hadrons, these hadrons proceed to produce additional collisions in the neighboring target nuclei, inducing an inter-nuclear cascade, or "hadronic" cascade [Armstrong et al., 1981]. This process continues until the energy of secondary hadrons for initiating such cascades falls below the threshold.

Figure 2.4 illustrates the course of cascade reactions. A proton projectile with high energy such as 600 MeV, hits the target nucleus initiating INC. Nucleons or clusters of nucleons such as alpha particles are ejected from the nucleus, accompanied by prompt gammas. Some of these ejectiles may propagate INC to further levels. Life time of an INC is very small, about 10^{-22} s. Hence, the nuclear media has no memory of the present state and interactions are completely incoherent. Due to the high energetics involved in INC, particles emitted are characterized by an overall fast spectrum.

Pre-equilibrium Stage

Because of the aforementioned physics assumptions, accuracy of predictions by the INC decreases at lower energies. An intermediate step between the INC and de-excitation is proposed to overcome the weakness of inaccuracy, which is described as the pre-equilibrium stage. This stage is characterized by the emission of high-energetic nucleons

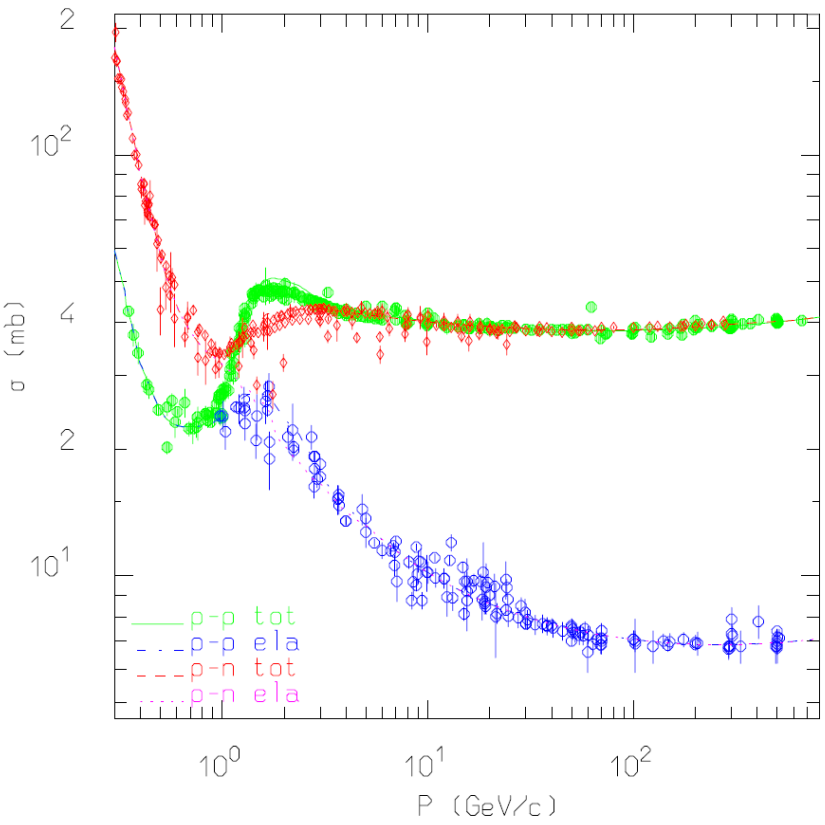

Figure 2.3: Total and elastic cross section for p-p and p-n scattering, together with experimental data [Ferrari and Sala, 1996]

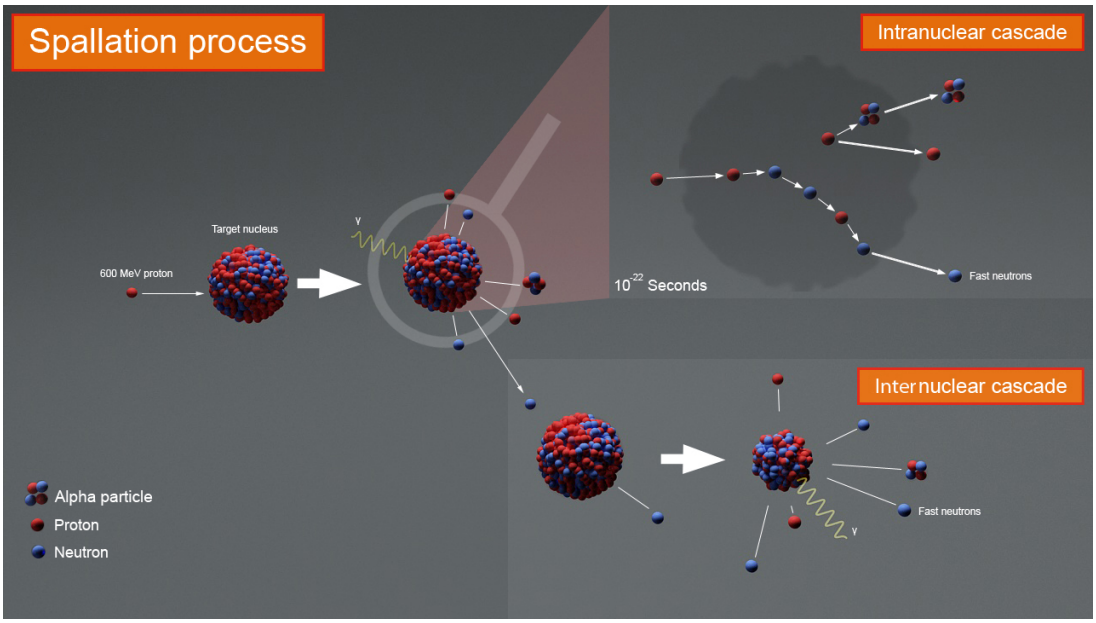

Figure 2.4: Course of nuclear cascade in spallation reaction

and light fragments. These particles of pre-equilibrium have kinetic energy higher than those of the particles emitted during de-excitation. The goal of the insertion of a pre-equilibrium stage between the cascade and the evaporation is to decrease the energy of the pre-fragment with the emission of rapid particles, i.e., a transition from INC to final thermalization. It allows increasing the production of residues near the projectile and decreasing the residues more distant of the projectile at the end of the evaporation. It also sets the initial conditions - mass loss, excitation energy, angular momentum of the pre-fragments – for the consecutive statistical de-excitation stage. Coupling this stage to INC models have improved the correlation of simulation results with the experimental data.

2.1.2 Statistical De-Excitation

Figure 2.5 illustrates the different modes of de-excitation of an excited nucleus, namely, evaporation, multi-fragmentation and fission. During de-excitation, these modes are in constant competition with each other depending upon the physical parameters. Some models capable of simulating this stage are Dresner, RAL and ABLA.

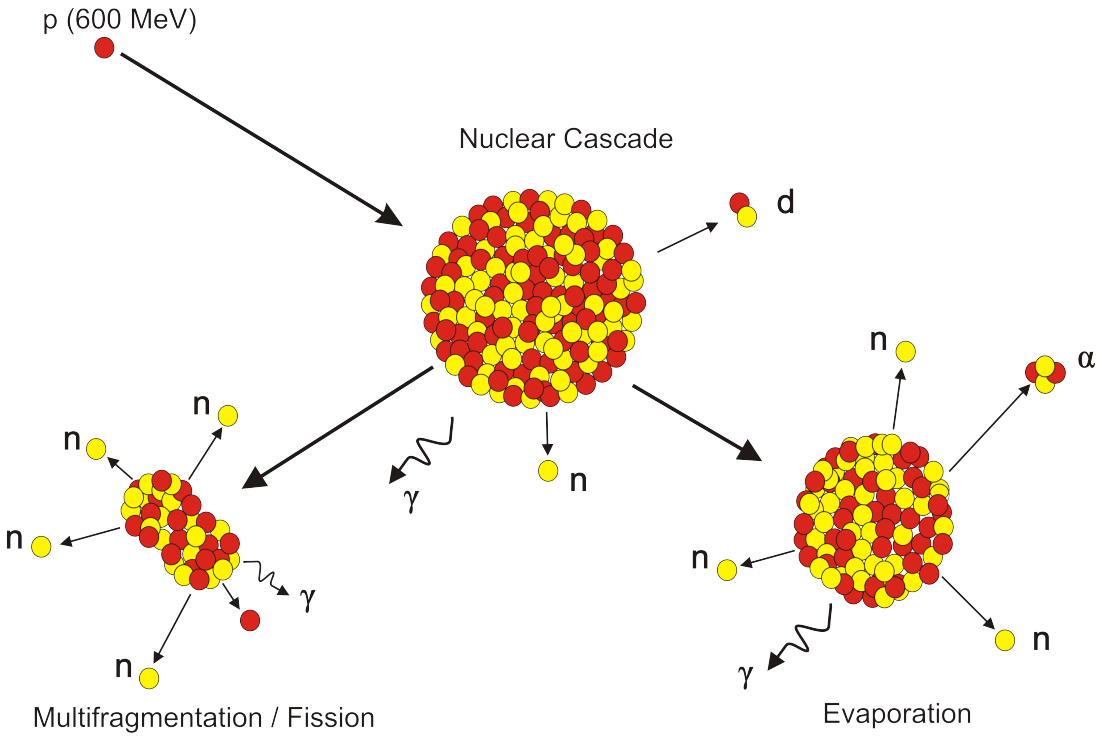

Figure 2.5: De-excitation modes of an excited residual nucleus

Evaporation

After the INC, the residual nucleus is left in an equilibrium state, in which the excitation energy is shared by a large number of nucleons. If the excitation energy is greater than the binding energy of particles, emission of nucleons and light fragments (α, d, t, ^{3}He) and other reaction channels are possible. The emission process is well described as an evaporation from a hot system, given by Weisskopf [Weisskopf, 1937]. According to this model, the evaporation probability ($P(E_j)$) for a neutron of energy E_j from an excited

nucleus with temperature T_f is:

$$P(E_j)dE_j \propto \sigma(E)E_j\, exp(-E_j/T_f)dE_j \tag{2.4}$$

where $\sigma(E)$ is the cross section for evaporation of the neutron from the compound nucleus of energy E. The emission spectrum of evaporation neutrons abides Maxwell distribution as seen in figure 2.6.

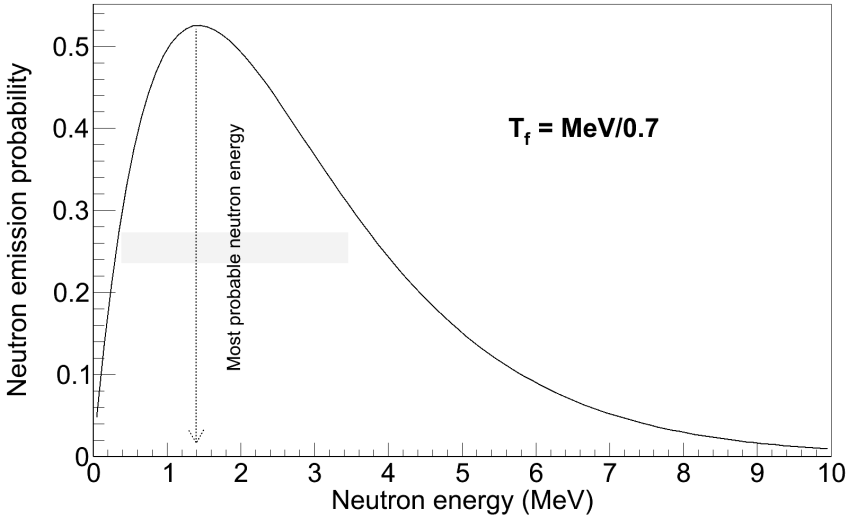

Figure 2.6: Probability distribution of evaporation neutrons

Fission

Even in the case of a not very fissile nucleus, the available energy can lead to the fission of the nuclei in two fragments. It is referred to as "hot" fission for energy higher than 50 MeV. But, this phenomenon is remarkable only for nuclei of charge number higher than 75 and at very high energies.

Multi-fragmentation

With sufficient energy, near the energy of separation of the nucleus, mechanical instabilities break the nucleus in several fragments (more than two). The higher the energy is, the larger the number of fragments will be and their size will be small. Multi-fragmentation can be considered as a very asymmetric fission process. This decay channel is characterized by the complete disintegration of the nucleus into several simultaneously emitted intermediate mass fragments (IMF).

Gamma De-excitation

Following the emission of nucleons and their clusters, residual excitation energy is dissipated by emission of gammas, i.e., when the excitation energy becomes lower than the binding energies for nucleons and fragments. Though gamma emission occurs even along with the above mentioned de-excitation stages, the branching ratio is rather small. Gamma de-excitation proceeds through a cascade of consecutive photon emissions, until the ground state is reached.

2.2 Characteristics of Spallation Neutrons

A basic reason for considering the spallation mechanism for intense neutron sources in general is that the thermal power density limit is lower i.e., the heat load per neutron obtained is less than for other mechanisms, as shown in table 2.1, except for controlled thermonuclear reactions (CTR), whose time of practical availability is uncertain [Armstrong et al., 1981]. This inherent advantage, coupled with steady progress in accelerator technology and the practical realities related to the present trend resisting fission reactor construction, makes the spallation method a very attractive alternative.

Table 2.1: Features of some mechanisms for neutron production

Process	Example	Yield	ED
			(MeV/n)
DT solid target	400 keV deuterons on tritium in Ti	4×10^{-5} n/d	10000
Deuterium stripping	35 MeV deuterons on liquid Li	2.5×10^{-3} n/d	10000
Electron bremsstrahlung photoneutron	100 MeV electrons on ^{238}U	5×10^{-2} n/e	2000
Fission	^{235}U(n,f)	1 n/fission	180
Spallation	800 MeV protons on ^{238}U	30 n/proton	55
D-T CTR	Laser or ion-beam imploded pellet	1 n/fusion	3

The neutron production channels in spallation mechanism are [Yurevich, 2009]:

- INC
- Evaporation of neutrons from excited fragment nuclei
- Emission from the hot residual nucleus
- Multi-fragmentation

for central collisions and at large angles. The former two channels, additionally contribute to peripheral collisions. At small angles, the hardest part of neutron spectrum is due to:

- Elastic and quasi-elastic nucleon–nucleon interactions
- Fragmentation of the projectile nucleus

Moving Source Model provides the interpretation and description of the double differential cross sections ($d^2\sigma/dEd\Omega$) for neutron production in the collisions of high energy protons and light nuclei with heavy nuclei in the energy range above 0.5 GeV per nucleon [Yurevich et al., 2006], such as for figure 2.9. Neutron emission at the cascade stage, neutron emission at the stage of the fragmentation of a highly excited residual nucleus, and neutron evaporation at the last stage on completion of the first two faster processes are considered as the basic mechanisms making the leading contribution to the neutron energy distributions. The cascade process is distinguished into central and peripheral collisions. According to this model, the experimental data has the the form:

$$d^2\sigma/dEd\Omega = \sum_{i=1}^{4} pA_i \times exp\left\{-\left(\frac{E+m-p\beta_i cos\theta}{(1-\beta_i^2)^{1/2}}-m\right)/T_i\right\} \tag{2.5}$$

where $p = \sqrt{E^2 + 2Em}$ is the neutron momentum, E is the neutron kinetic energy (in MeV) in the laboratory system, m is the neutron mass (in MeV), and θ is the neutron emission angle in the laboratory system. There are four sources in the model which includes neutron emission in the cascade stage (i = 1), in the peripheral and central collisions (i = 2), in the fragmentation process (i = 3), and in the evaporation stage (i = 4). Each moving source is characterized by the amplitude A_i, temperature T_i, and velocity β_i measured in units of the speed of light.

2.2.1 Energy Spectrum

Comparison of Fission and Spallation Neutron Energy Spectrum

Figure 2.7 compares the fission and spallation neutron yield spectrum normalized to unity. The fission neutron spectrum for ^{239}Pu has been derived using the Maxwellian distribution function [Bauer, 2001]:

$$n(E) = \frac{2E^{1/2}}{\pi^{1/2} {E_T}^{3/2}} exp\left(-\frac{E}{E_T}\right) \tag{2.6}$$

with E_T=1.33 MeV. The spallation case is for 600 MeV protons on a tungsten target. Apparently, the spallation spectrum extends up to incident proton energies, while that for fission spectrum is limited below 20 MeV. From the figure it is conclusive that the spallation neutrons are relatively harder than the fission neutrons.

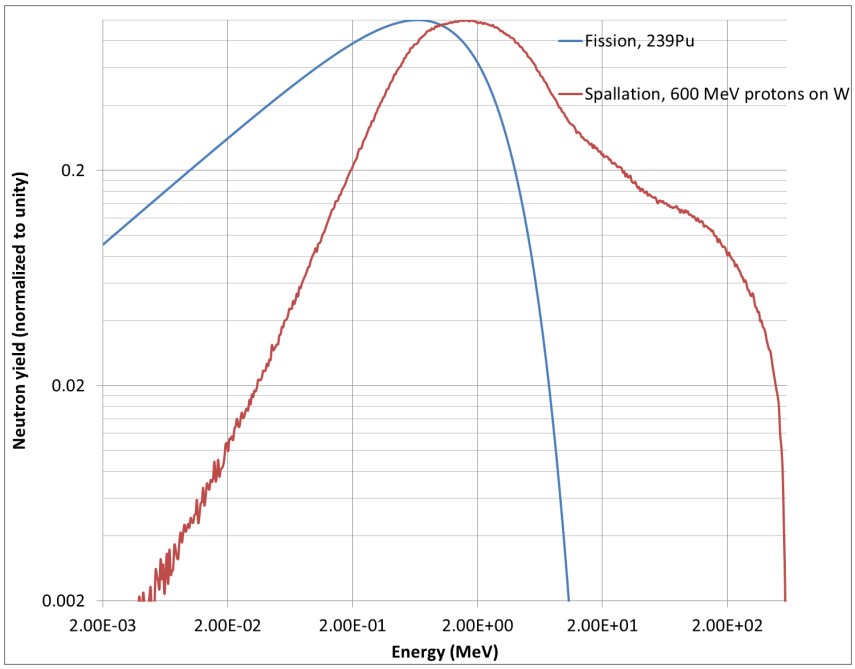

Figure 2.7: Comparison of fission and spallation neutron spectrum

In spallation reactions, mean neutron multiplicity (M_n) depends on the mass number (A_t) of the target nucleus and the energy (E_p in GeV) of the incident protons up to 2 GeV. It almost varies linearly with A_t, slightly increases with increasing beam energy, according to [Yurevich, 2009]:

$$M_n = (0.0803 + 0.0336 ln E_p) A_t \tag{2.7}$$

Further, neutron multiplicity could be separated into contributions from the cascade process and evaporation, according to the following parameterization:

$$M_n = {M_n}^{casc} + {M_n}^{evap} = (a_1 A_t + a_2) + b_1 {A_t}^{b_2} \tag{2.8}$$

where a_2 ≈0.02, b_2 is about 1, and the values of other parameters depend on the proton energy.

Simulation results of neutron multiplicity distribution for 600 MeV protons impinging on a thick tungsten target is shown in figure 2.8, along with the fit parameters according to equation 2.9. Neutron multiplicity distribution ($d\sigma/dM_n$) is more informative for studies of neutron yield than the integral value of the mean neutron multiplicity and is approximated by an parameterized expression consisting of two terms [Hilscher et al., 1998]:

$$\frac{d\sigma}{dM_n} = \frac{S_G}{s\sqrt{2\pi}} exp\left(-\frac{(M_n - {M_n}^{max})^2}{2s^2}\right) + \frac{S_E}{T_n} exp\left(-\frac{M_n}{T_n}\right) \tag{2.9}$$

where the first term has the form of a Gaussian distribution and describes the peak at large neutron yields with the maximum at ${M_n}^{max}$ and the second term has the exponential distribution whose contribution decreases with increasing M_n

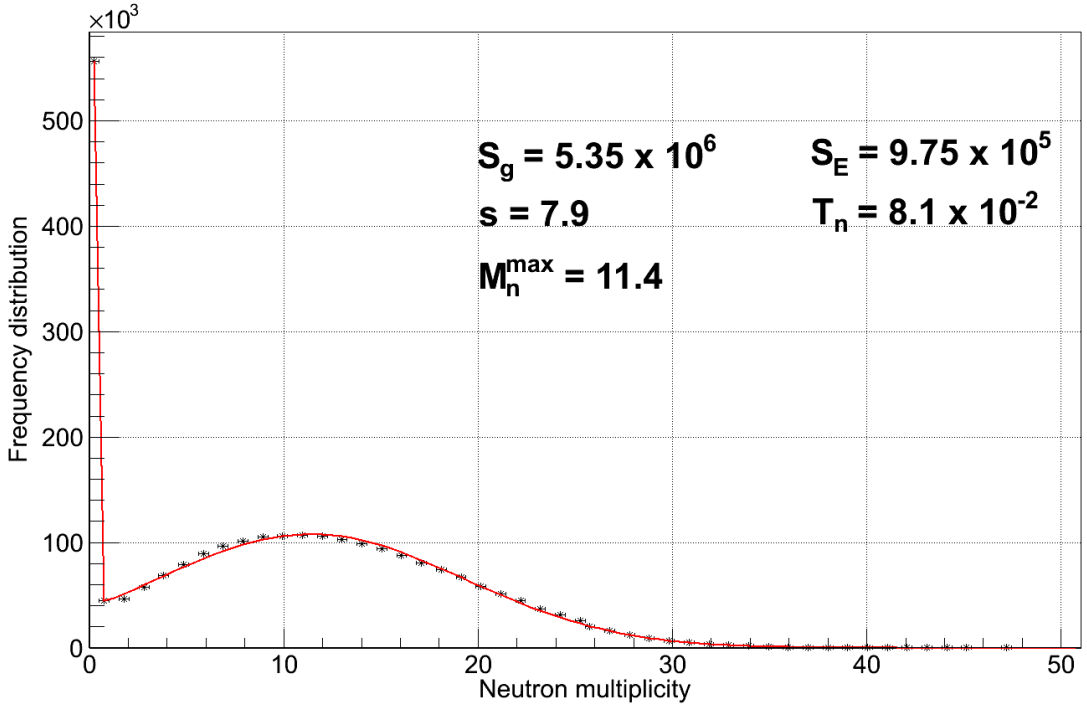

Figure 2.8: Neutron multiplicity distributions for a 10 cm radius tungsten target bombarded by protons of 600 MeV energy

From figure 2.8, it can be interpreted that the distribution has the form of a wide peak in the region of large neutron multiplicities and an exponentially decreasing contribution at small neutron multiplicities [Yurevich, 2009]. The peak becomes wider and shifts towards larger neutron multiplicities as both the incident proton energy and the mass number of the target nucleus increase. Neutron yield decreases in the exponential term as the mass number of the target nucleus increases. The two-component representation, probably, corresponds to collisions with different impact parameters, i.e., to central and peripheral ones.

2.2.2 Angular Spectrum

Unlike fission neutrons, angular distribution of spallation neutrons is not completely isotropic. Figure 2.9 shows the double differential cross section for neutron emission from a lead target of 3 cm diameter when bombarded with 800 MeV protons. As it can be seen, the low energy part of this neutron spectrum is fairly isotropic as they are mostly neutrons evaporating during the various stages of the spallation process. It is also interesting to note the behavior of the high energy tail of the spectrum, it increases with decreasing angles i.e., high energy neutrons are slightly forward-peaked. As most of energetic neutrons are produced during the inter-nuclear cascade (INC) process, they are emitted in the same direction as the impinging proton beam. In case of neutron energy spectra for small angles (θ <5^0), peripheral collisions make the largest contribution to the high energy part of the neutron spectra because of quasi-elastic and quasi-inelastic interactions [Cugnon et al., 1997].

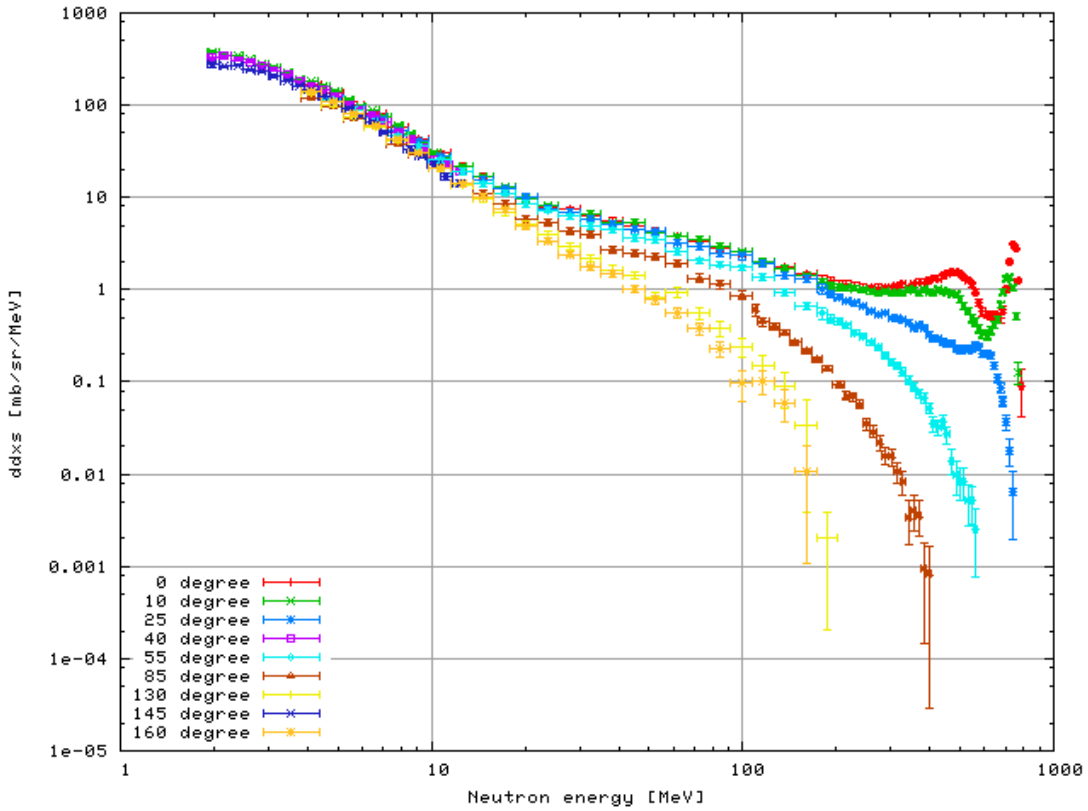

Figure 2.9: Double differential cross section for neutron emission from lead spallation [Leray et al., 2002]

The phenomenon of neutron angular distribution becomes more clear with figure 2.10. In this particular case, about 30% of the neutrons yielding from the thick spallation target have energy above 1 MeV.

2.3 Formation of Spallation Products

Spallation products are responsible for the initial accumulation of nuclides in a proton irradiated target. The secondary particles, mainly neutrons emitted through different

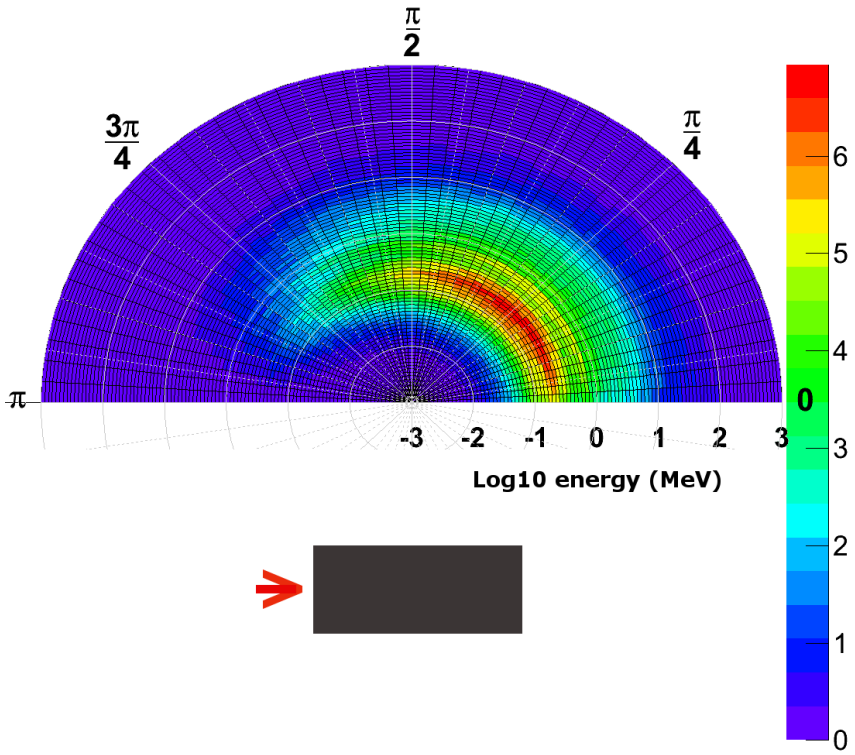

Figure 2.10: Angular distribution of neutrons (relative unit) in different energy groups for a 10 cm radius tungsten target bombarded by protons of 600 MeV energy

nuclear reactions transmute them as well as the target material. The equation governing the behavior of the spallation product formation is given by:

$$\frac{dN_i}{dt} = IY_i - (\lambda + \sigma\phi)_i Ni = 0 \tag{2.10}$$

where Y_i denotes the yield of a particular spallation product i at proton current I, together representing the accumulation rate of spallation products. And the depletion rate due to both natural decay and neutron induced reactions is represented by the second term. [Stankovsky et al., 2001]

Figure 2.11 shows the distribution of spallation products in the Hg target due to 1.334 GeV protons, according to the mass numbers of the nuclides. Products close to the target, corresponding to very peripheral collisions have limited excitation energy. Hence they populate the region near to the valley of stability by few neutron evaporation. For more central collisions, the excitation energy deposited in the pre-fragment is larger, and more neutron deficient isotopes are produced. Finally, for higher excitation energy, the evaporation of protons and composite particles become important. The nuclide distributions may be understood as the result of a delicate interplay between the excitation energy gained in INC and de-excitation processes. The mass distribution presents a sharp increase for the fragments very close to the target, produced in peripheral reactions. As the mass of the fragments decrease, a plateau is observed, followed by an exponential decrease, reflecting the limited excitation energy induced in the spallation process. [Benlliure et al., 2001]

Five distinctive classes of nuclides could be made which are explained as follows:

Evaporation Products Hadrons like protons and neutrons and other lighter nuclei which are evaporated from the excited nuclei during de-excitation of pre-fragments form

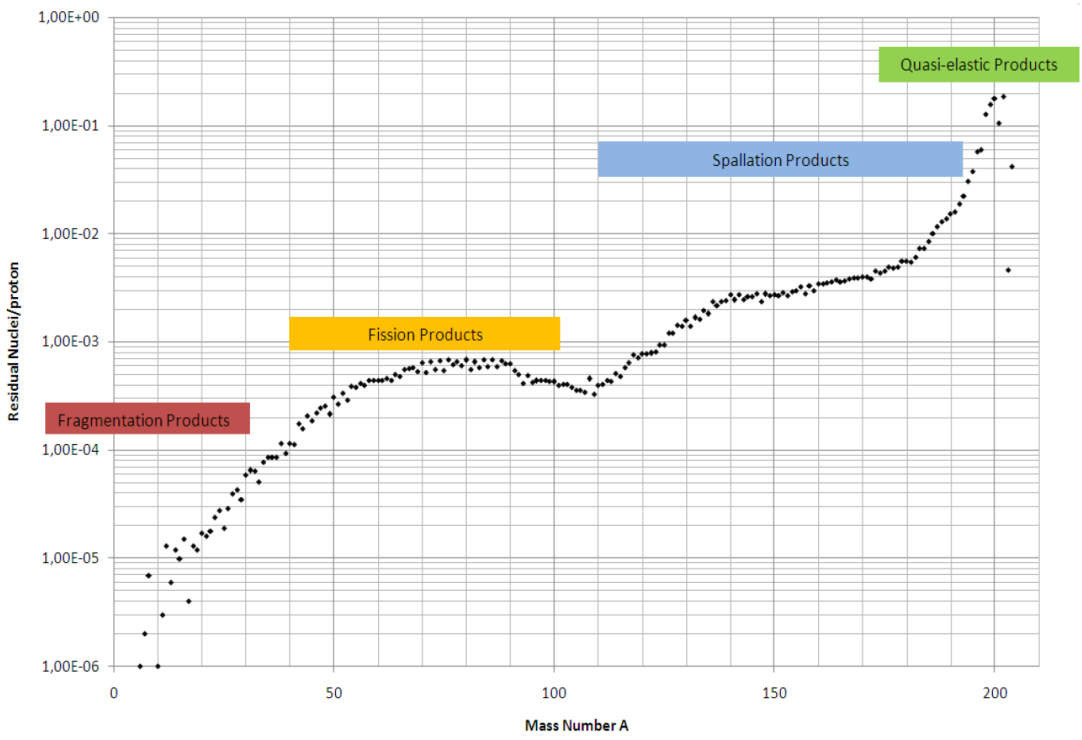

Figure 2.11: Distribution of spallation products in Hg target due to 1.334 GeV protons

this class of products (not visible in the figure).

Fragmentation Products Fragmentation process which constantly competes with evaporation during the whole of de-excitation leads to the formation of IMF (i.e., A<1/3 A_{target}).

Fission Products The fission residues populate the medium mass interval and have a symmetric distribution.

Spallation Products The products left over after the evaporation of the particles from the pre-fragments are the spallation products. They can be either due to peripheral collisions or due to more central collisions on the target nuclei. In the latter case deep spallation (i.e., mass loss $\Delta A > 30$) products are formed [Wang and Porile, 1987].

Quasi-elastic Products The charge pickup reactions (direct process) proceed either through a quasi-elastic collision between a proton and a neutron of the target and pre-fragment nuclei respectively, where the proton replaces the neutron, or through the excitation of a projectile (or target) nucleon into a resonance state and its subsequent decay [Gaarde, 1991]. Even double charge pickup reactions are possible. It explains the formation of the nuclides whose atomic/mass number is greater than that of the target itself, other than due to the neutron activation products.

2.4 Application of Spallation Neutron Sources

2.4.1 Scientific Applications

The book "Handbook of Spallation Research" [Filges and Goldenbaum, 2010] illustrates many applications and experiments of spallation. Neutrons are an ideal probe for investigation of the structural and dynamical properties of matter. Non-destructive study of matter is possible, as neutrons penetrate deep into the matter because of their electrical neutrality. The magnetic moment enables neutrons to explore microscopic magnetic structures and study magnetic fluctuations. The energies of thermal neutrons are similar to the energies of elementary excitations in solids and consequently molecular vibrations, lattice modes and the dynamics of atomic motions can be probed. In particular for light atoms, neutron scattering supersedes investigations using x-rays, because neutrons scatter from materials by interacting with the nucleus rather than the electron cloud of an atom. Streamlined application of neutrons in scientific areas include:

- Solid state physics
- Materials science and engineering
- Chemical structure, kinetics and dynamics
- Soft condensed matter
- Biology and biotechnology
- Earth and environmental science
- Fundamental neutron physics

2.4.2 Energy Amplifier Concept

Energy amplifier (EA) concept proposed by Rubbia [Roche et al., 1995] aims at the utilization of thorium in an ADS system. The EA is a large, passive device in which a proton beam is dumped and the heat generated by nuclear cascades is extracted. The delivered power is controlled exclusively by the current of the accelerator.

2.4.3 Isotope Production

By bombarding a specific material with a proton beam, the nuclei of the atoms in the target material are broken apart creating radioactive isotopes. A new project at the European Organization for Nuclear Research (CERN), hailed as MEDICIS [MEDICIS, 2012], will make it possible to produce a large variety of radioactive isotopes for medical research.

2.4.4 Transmutation of Nuclear Waste

Transmutation of nuclear waste is discussed in section 1.3.

CHAPTER 3

Particle Transport Simulation Method and Tool

3.1 Monte Carlo Method

Monte Carlo (MC) can be used to duplicate theoretically a statistical process (such as the interaction of nuclear particles with materials) or also sometimes deterministic process (such as integration) and is particularly useful for complex problems that cannot be modeled by computer codes that use deterministic methods [MCNPX, 2008]. The individual probabilistic events that comprise a process are simulated sequentially. The probability distributions governing these events are statistically sampled to describe the total phenomenon. In general, the simulation is performed on a digital computer because the number of trials necessary to adequately describe the phenomenon are usually quite large. The statistical sampling process is based on the selection of random numbers-analogous to throwing dice in a gambling casino,hence, the name "Monte Carlo". In particle transport, the MC technique is pre-eminently realistic (a numerical experiment). It consists of actually following each of many particles from a source throughout its life to its death in some terminal category (absorption, escape, etc.). Probability distributions are randomly sampled using transport data to determine the outcome at each step of its life.

Figure 3.1 represents the random history of a neutron incident on a slab of material that can undergo fission. Numbers between 0 and 1 are selected randomly to determine what (if any) and where interaction takes place, based on the rules (physics) and probabilities (transport data) governing the processes and materials involved. In this particular example, a neutron collision occurs at event 1. The neutron is scattered in the direction shown, which is selected randomly from the physical scattering distribution. A photon is also produced and is temporarily stored, or banked, for later analysis. At event 2, fission occurs, resulting in the termination of the incoming neutron and the birth of two outgoing neutrons and one photon. One neutron and the photon are banked for later analysis. The first fission neutron is captured at event 3 and terminated. The banked neutron is now retrieved and, by random sampling, leaks out of the slab at event 4. The fission-produced photon has a collision at event 5 and leaks out at event 6. The remaining photon generated at event 1 is now followed with a capture at event 7. This neutron history is now complete. As more and more such histories are followed, the neutron and photon distributions become better known. The quantities of interest (whatever the user requests) are tallied, along with estimates of the statistical precision (uncertainty) of the

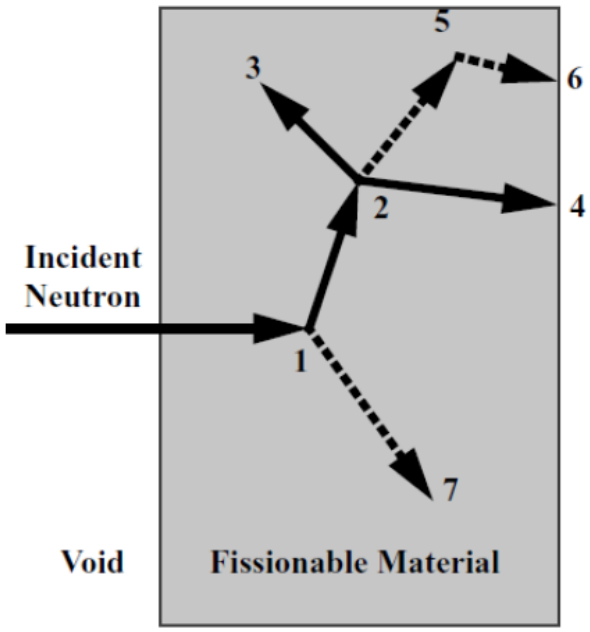

Figure 3.1: Random walk of particles in monte carlo method

results.

The first approach to compute the INC using the MC technique were made in early 1950's [Benlliure, 2006]. Progress in computer hardware and numerical methods helped to develop new models to describe spallation mechanism. MC particle transport simulations can be performed using computer codes like MCNPX [MCNPX, 2008], FLUKA [Battistoni et al., 2006] and Geant4 [Allison et al., 2006, Agostinelli et al., 2003]. Using these codes, histories of particles of different types and energy, as well as the generation of secondary particles and nuclides are simulated on the basis of nuclear data library and/or models. For this work, the Geant4 toolkit has been employed.

3.2 Geant4 Toolkit

Geometry and tracking (Geant4) is a toolkit for the simulation of the passage of particles through matter [Geant4, 2012]. The toolkit, in C++, makes building applications flexible and versatile. Its areas of application include high energy, nuclear and accelerator physics, as well as studies in medical and space science. Geant4 propagates particles - elementary particles and ions, both stable and unstable - through any geometrical arrangement of material. Many different models area available in Geant4, that have been derived from the domains of particle, nuclear and atomic physics [Geant4, 2010]. Electromagnetic processes such as bremsstrahlung, delta ray production, pair-production, Compton scattering, photo-absorption and multiple scattering are well described. In the area of nuclear and hadronic interactions, simulations are shaped either through data-driven (neutron data) or theoretical models (binary cascade) or both. The high precision neutron model (Neutron_HP) to describe low energy neutrons (<20 MeV) depends on an evaluated neutron data library (G4NDL) for cross sections, angular distributions and final state information.

3.2.1 The INC Model

The Binary Cascade (BIC) is a new approach to cascade calculations, based on a detailed 3-dimensional model of the nucleus, and exclusively based on binary scattering between reaction participants and nucleons within this nuclear model [Folger et al., 2004]. This feature makes it a hybrid between a classical cascade code, and a quantum molecular dynamics (QMD) model.

Interactions take place between a primary or secondary particle and an individual nucleon of the nucleus. The nucleus is modeled by explicitly positioning nucleons in space, and assigning momenta to these nucleons. This is done in a way consistent with the nuclear density distributions, Pauli's exclusion principle, and the total nuclear mass. Free hadron-hadron elastic and reaction cross section are used to define collision locations within the nuclear frame (such as in figure 2.3). Where available, experimental cross-sections are used directly or as a basis for parameterizations used in the model. Particles propagation in the nuclear field is done by numerically solving the equations of motion, using time-independent fields derived from optical potentials. The cascade begins with a projectile and the nuclear description, and terminates when the average energy of all participants within the nuclear boundaries are below a given threshold.

In BIC, the nucleus is a 3-dimensional model of the nucleus constructed from A nucleons and Z protons with coordinates r_i and momenta p_i, with i = 1,2,3,...,A. For nuclei with A > 16, Wood-Saxon form of the nucleon density $\rho(r_i)$ is used:

$$\rho(r_i) = \frac{\rho_0}{1 + exp\left[(r_i - R)/a\right]} \tag{3.1}$$

where ρ_0 is approximated as:

$$\rho_0 = \frac{3}{4\pi R^3}\left(1 + \frac{a^2\pi^2}{R^2}\right)^{-1} \tag{3.2}$$

Here a = 0.545 fm, and $R = r_0 A^{1/3}$ fm with r_0 = 1.16(1 - $1.16A^{-2/3}$) fm.

The nucleus is assumed to be spherical and isotropic using a random direction and r_i based on nuclear density. The momenta p_i of the nucleons are chosen randomly between 0 and Fermi momentum ${p_F}^{max}(r_i)$. The Fermi momentum is given as the function of nuclear density as:

$${p_F}^{max}(r_i) = \hbar c(3\pi^2\rho(r))^{1/3} \tag{3.3}$$

The total vector sum of nucleon momenta has to be zero, implies that the nucleus must be constructed at rest.

For protons and neutrons the potential used is determined by the local Fermi momentum $p_F(r)$ as:

$$V(r) = \frac{{p_F}^2(r)}{2m} \tag{3.4}$$

where m is the mass of the neutron or mass of the proton respectively.

The free particle cross sections are modified to effective cross sections due to Pauli's exclusion principle. The final state of nucleons created in the cascade occupy a state dictated by Fermi statistics where, nucleus is assumed to be in ground state and all states below Fermi energy are occupied. Thus, collisions and decays for which any secondary nucleon has a momentum p_i below the local Fermi momentum are suppressed.

Cascading continues till the kinetic energy of the participants is above a certain threshold (70 MeV) after which the residual participants and the nucleus in its current state are used to define the initial state for pre-equilibrium and subsequent de-excitation treatment, whose physics descriptions can be found in the Geant4 manual [Geant4, 2010].

A rich set of experimental data [IAEA, 2012] is available to verify neutron production by protons incident upon various targets for different proton energies. Neutron yield, their energies and angular dependence can be measured with good precision using time-of-flight techniques. The high energy part of the double differential neutron spectra is very sensitive to the physics models used to simulate cascade. According to the benchmark studies of spallation models [CEA, 2010], Geant4-BIC describes the data reasonably well and performs better than Geant4-Bertini. In particular, BIC agrees better with the data for neutron production, low and medium energy protons, light ion production and isotropic distribution.

Figure 3.2 shows the double differential cross sections for proton induced neutron production at forward angles for several materials. A very good prediction by BIC is seen for the description of the forward peak spectra in several materials. Figure 3.3 shows the neutron double differential cross sections at several angles for several incident proton energies in lead. Good agreement between the data and BIC prediction is found except for high energy neutrons at large angles. The short coming is attributed due to the absence of S-wave pion re-absorption on quasi-deuterons in the model for incident proton energies above the pion production threshold, in particular for large nuclei. Similarly, tritium production is also well predicted by the model (figure 3.4).

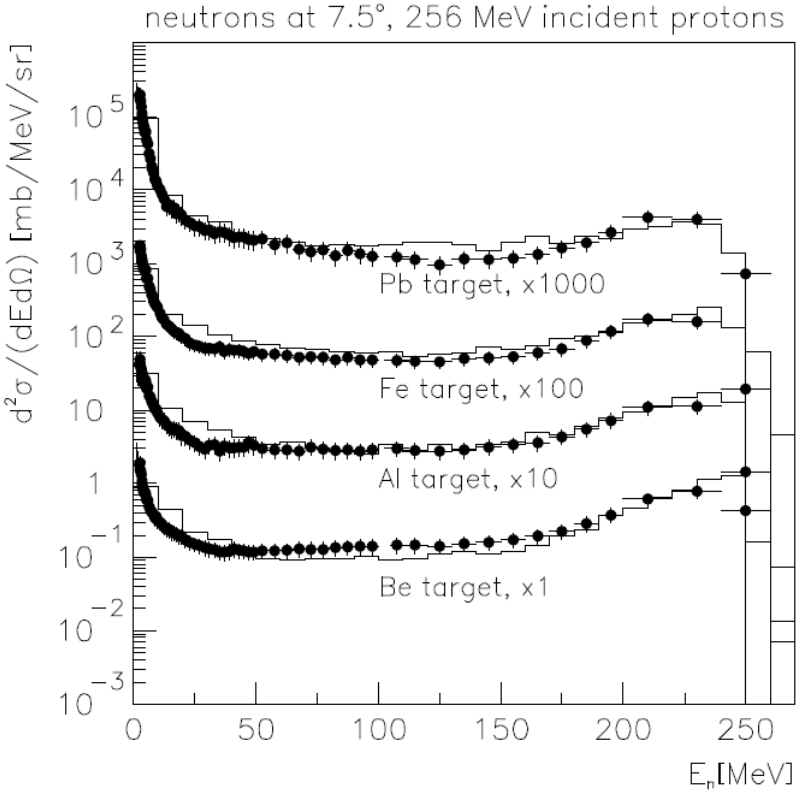

Figure 3.2: Double differential cross section for neutrons produced in proton scattering at 7.5 degrees by 256 MeV protons. Histograms: Binary Cascade predictions, points: data [Folger et al., 2004]

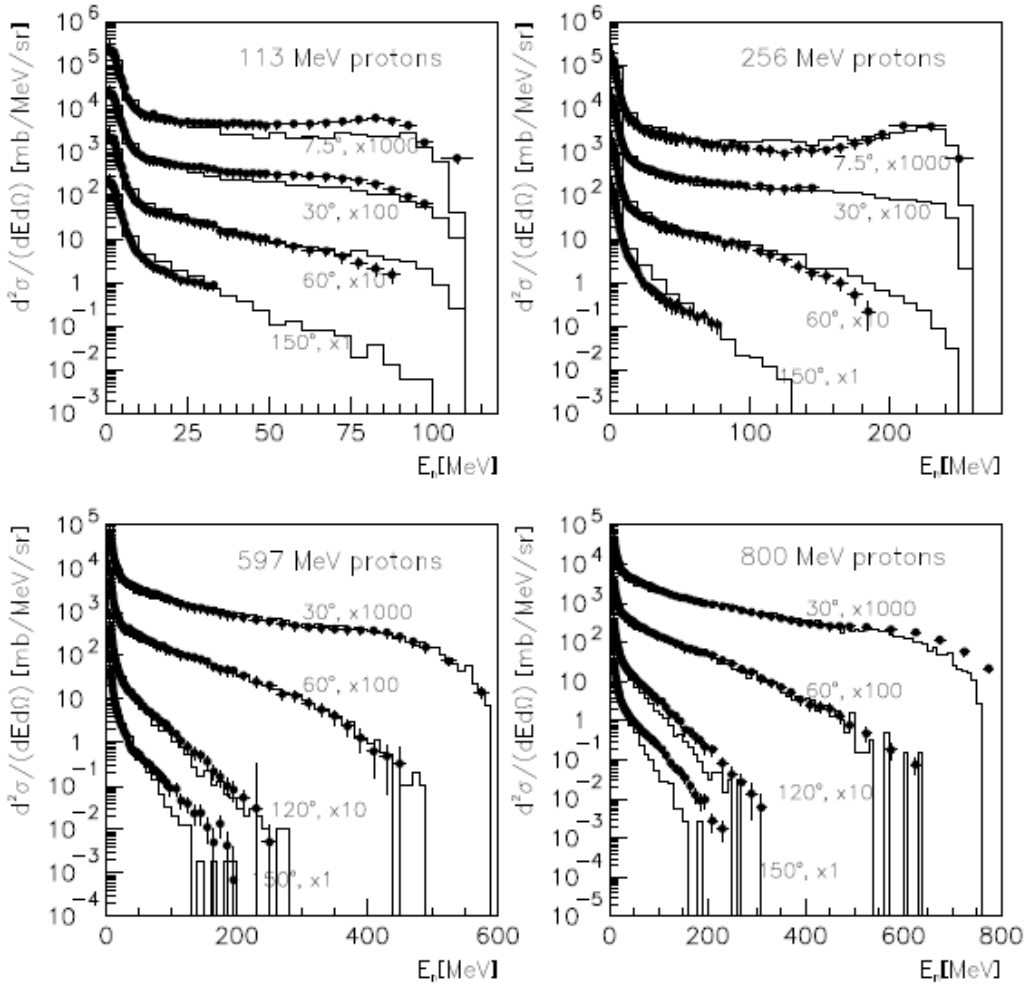

Figure 3.3: Double differential cross section for neutrons produced in proton scattering off lead. Histograms: Binary Cascade predictions, points: data [Folger et al., 2004]

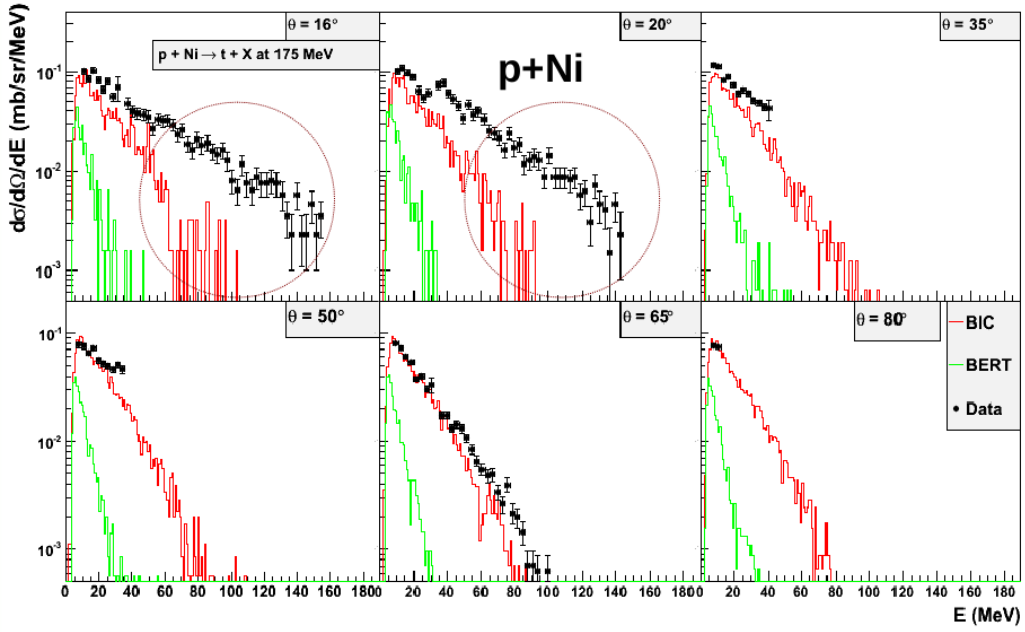

Figure 3.4: Double differential cross section for tritium production in proton scattering off nickel. Histograms: BIC and Bertini model predictions, points: data [IAEA, 2012]

3.2.2 Validation of Neutron Data and Model

The TARC experiment was conducted to study neutron driven nuclear Transmutation by Adiabatic Resonance Crossing. Neutrons production from a high purity lead target was measured due to 2.5 GeV/c and 3.5 GeV/c protons.The experiment was simulated using Geant4 to validate neutron transportation in the toolkit [Howard, 2006]. Many neutron processes such as primary and secondary neutron production, moderation and transmutation over a broad energy range could be analyzed using the high quality of data obtained from TARC. This data proves to be a good benchmark for validation of neutron data and model.

For this simulation in Geant4, binary cascade model is used for high energy cascades along with Neutron_HP package for low energy neutrons. Neutron_HP handles neutron interaction, transportation, elastic scattering and capture. Further, binary cascade is coupled to pre-equilibrium model to describe the transition from high energy cascade to low low energy domain, followed by de-excitation model. The absolute neutron fluence measured in the TARC experiment has been compared with the simulation data obtained from Geant4 in figure 3.5. In the figure, neutron fluence is plotted as a function of neutron energy from 0.01 eV up to 2 MeV.

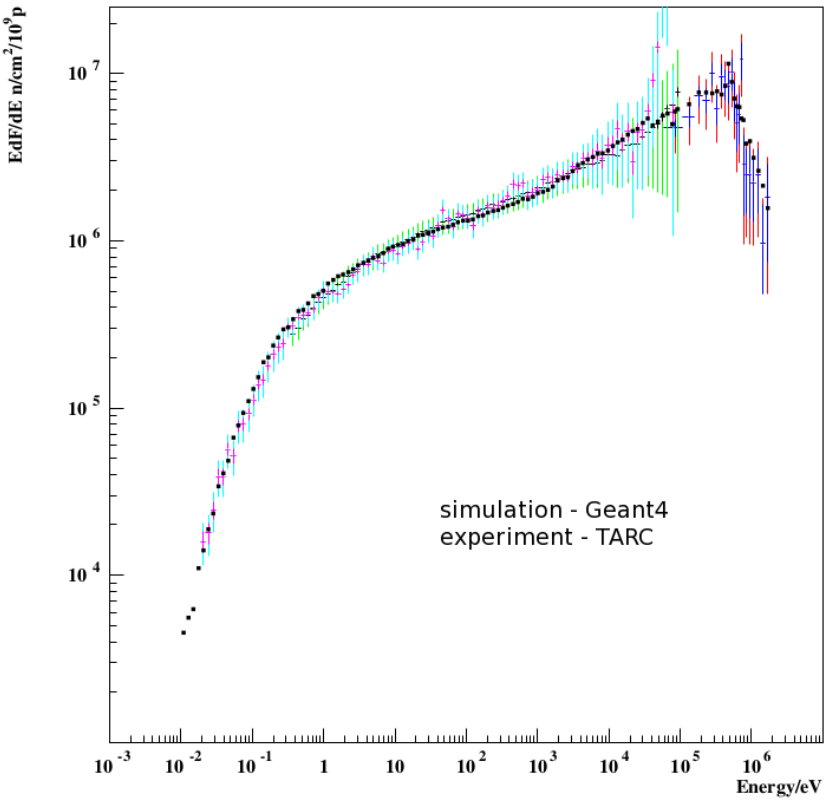

Figure 3.5: Comparison of absolute neutron fluence data (blue) in the TARC experiment with the Geant4 simulation data (black)

The simulation data is found to be within the systematic errors of the experimental data. The large proportion of evaporation neutrons that form the low energy part of the above spectrum results in smaller errors in the simulation data. On the other hand, errors in the simulation data increases with increasing neutron energy. This is true because the high energy tail of the spectrum is less populated. It is seen here that the experiment data is generally well reproduced by Geant4 simulation.

CHAPTER 4

Particle Production Study in Spallation Reactions

4.1 Effect of Projectile Type and Energy on Neutron Yield

4.1.1 Projectile Type

The range of an ion (R) in a matter can be expressed in terms of the range of a proton (R_p) at the same velocity [Turner, 2007],

$$R = M/z^2 R_p \tag{4.1}$$

where z is the charge and M is the mass of the ion respectively. This illustrates that the range of an heavier ion is smaller than that of the proton, given the energy and material are same for both the particles. In other words, heavier ion requires higher kinetic energy to travel the range set by a proton due to coulomb barrier. To illustrate this with an example, consider proton and oxygen ion on a lead target. The mean-free-path (λ) is 200 g/cm^2 and 135 g/cm^2 respectively [Armstrong et al., 1981]. To traverse one λ, a proton requires about 450 MeV, while it takes about 900 MeV for an oxygen ion [PSTAR, 2012]. To allow more nuclear collisions to occur, the ion range has to be sufficiently longer, this means increasing kinetic energy (figure 4.1). Since the cost accrued to accelerate heavier ions to higher energies at a reasonable current is extremely formidable, protons, by default become the ideal projectiles.

The nuclear collision cross section (σ) is approximately constant with energy and increases slowly with increasing ion mass,

$$\sigma \propto \left({A_i}^{1/3} + {A_T}^{1/3}\right)^2 \tag{4.2}$$

where A_i and A_T are respectively the mass numbers of projectile ion and target nucleus. The above equation suggests that the neutron multiplicity will be higher for heavier ions. In this interest, deuteron is a special case because (a) deuteron and proton have the same charge, and (b) nucleons of deuterons are weakly bound and easily "stripped" in nuclear collisions, resulting in a source of neutron and protons, each with about one-half of deuteron energy. Calculations indicate that for 1 GeV deuteron beam on lead target, improves neutron yield by 10% in comparison to proton beam with essentially no difference in heating.

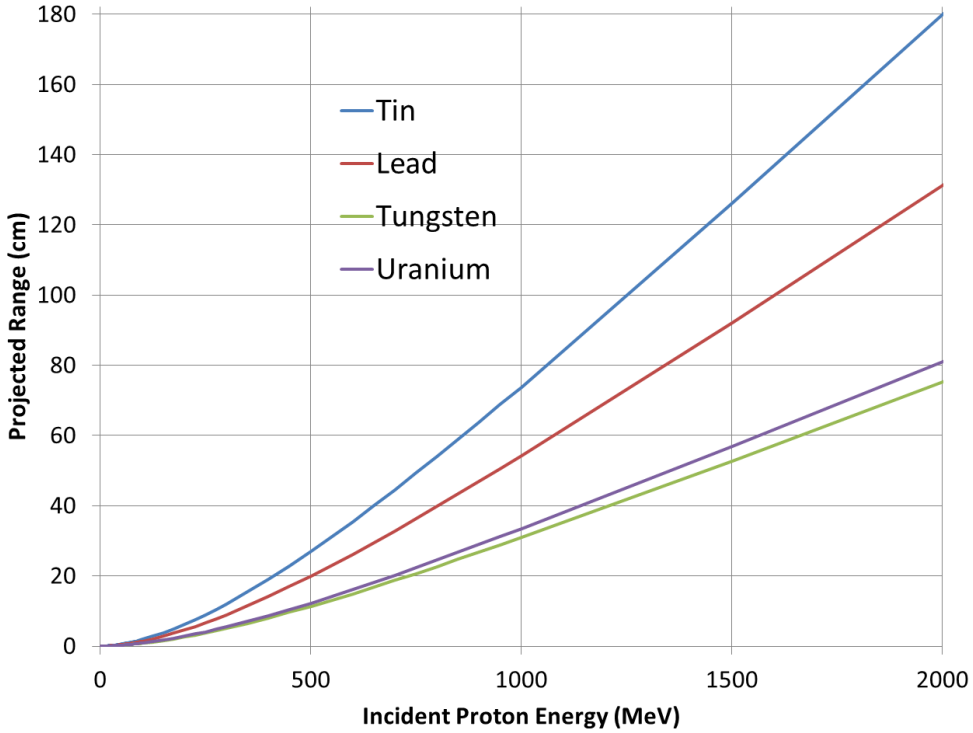

Figure 4.1: Projected range of protons with different energies in some materials

The experimental neutron yield (Y_i) of a 20×60 cm lead target in which an ion (p, d, ^{4}He) beam with energy E_i/Z_i in the interval - 10^2-10^3 MeV is absorbed can be satisfactorily parameterized by the expression [Fasil'kov et al., 1995],

$$Y_i/Z_i = a_i + b_i(E_i/Z_i)^c \tag{4.3}$$

where c = 0.75 for all ions. The coefficients a_i and b_i are presented in the table 4.1.

Table 4.1: Experimental coefficients for neutron yield due to p, d and ^{4}He on lead target

Ion	$\mathbf{a}_i$	$\mathbf{b}_i$	**Energy Range (GeV)**
p	-8.2	29.3	$0.4 \leq E_p \leq 8.1$
d	-9.2	33	$1.0 \leq E_d \leq 5.4$
^{4}He	-16.3	31.3	$1.0 \leq E_a/2 \leq 5.4$

Figure 4.2 shows the neutron multiplicity due to p, d and ^{4}He of different energies. In the lower energy range, neutron yield is generally higher for p and d than for ^{4}He. It is also interesting to note that the neutron yields due to p and d are almost similar up to 600 MeV. Then, d is more productive by about 10% at about 1 GeV, also as indicated in the report [Armstrong et al., 1981]. The weakly bound nucleus of d contributes an additional neutron source. The neutron yield for d increases at higher energies, for example about 20% more at 2 GeV, in comparison to protons. Hence, deuteron projectiles are reasonably effective in producing neutrons, say above 1 GeV. Protons are ideal projectiles at lower energies in the range of about 600 MeV, as the acceleration cost is comparatively lesser.

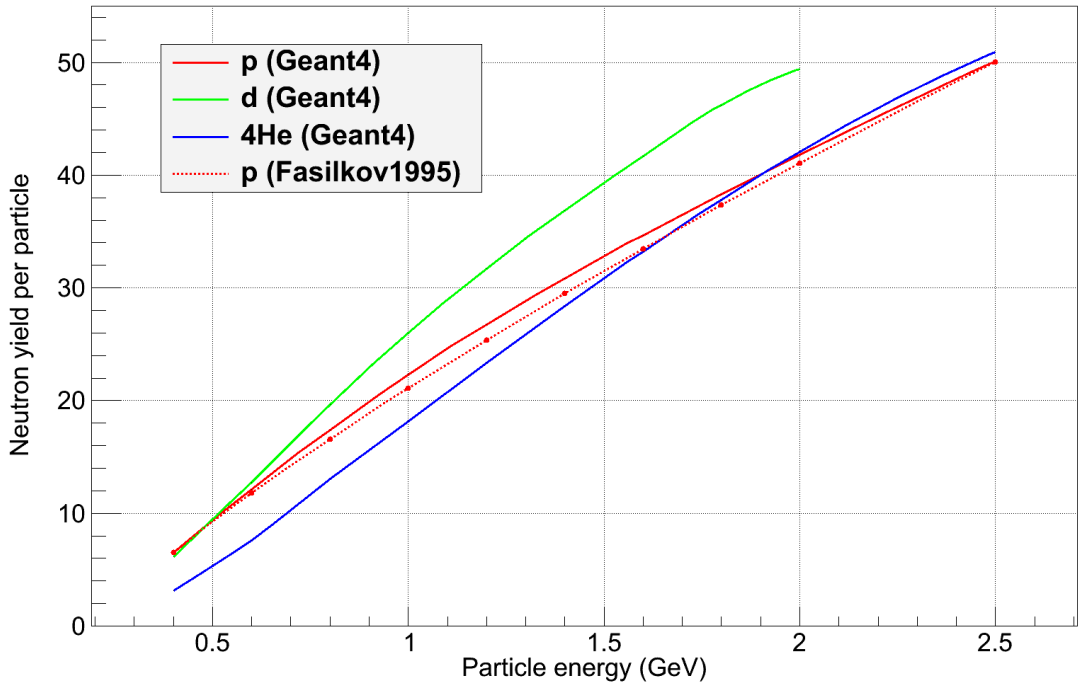

Figure 4.2: Comparison of neutron yield in lead due to p, d, and ^{4}He with the experimental data

4.1.2 Projectile Energy

The range of protons, which is a monotonically increasing function of energy, in the material should be sufficiently large compared to nuclear collision λ [Armstrong et al., 1981]. Nuclear λ for non-elastic collision is approximately given as

$$\lambda = 33A^{0.33}\ g/cm^2, \text{ for E} \geq 100 \text{ MeV and A} > 1 \tag{4.4}$$

Probability of nuclear collision (P_n) occurring before the proton reaches the end of its range (R) is

$$P_n = 1 - exp(-R/\lambda) \tag{4.5}$$

According to Bauer, 120 MeV is the "threshold" energy below which spallation becomes very improbable in competition with energy losses due to ionization [Bauer, 2001]. Table 4.2, shows P_n for different energies of proton incident on tungsten according to equations 4.4, 4.5 and figure 4.1. It becomes clear that P_n increases with increasing energy and at 1 GeV (or above 3λ), it is almost 100%. Hence, substantial nuclear collisions can be obtained to produce neutrons at a proton beam energy of several hundres of MeV, or more. This holds true for other materials as well, because λ is constant above 100 MeV.

Experimental data [Letourneau et al., 2000] is available for neutron yield in Pb, Hg and W targets, each 15 cm in diameter and about 35 cm long due to protons of 1.2, 1.8 and 2.5 GeV. The experiment has been reproduced through a Geant4 simulation and the results are displayed in figure 4.3, also compared with experimental values. The maximum deviations between the experiment and the simulation are about 5%, 2% and 10%, respectively for Hg, Pb and W. Neutron yield increases with increasing incident proton energy, being almost linear w.r.t. energy up to 1 GeV. In this energy range, the

Table 4.2: Nuclear collision probabilities for protons of different energies on tungsten

Energy MeV	**Range (R)** g/cm^2	**R/λ**	**P$_n$**
200	50.31	0.27	0.24
400	154.6	0.84	0.57
600	287.2	1.56	0.79
800	436.4	2.37	0.91
1000	595.5	3.23	0.96
1500	1016	5.51	1.00
2000	1449	7.86	1.00

neutron yield is similar for all the three materials. Above 1 GeV, neutron yield increases for W, followed by Hg and Pb, relating to the material densities 19.25, 13.55 and 11.34 g/cm^3 respectively.

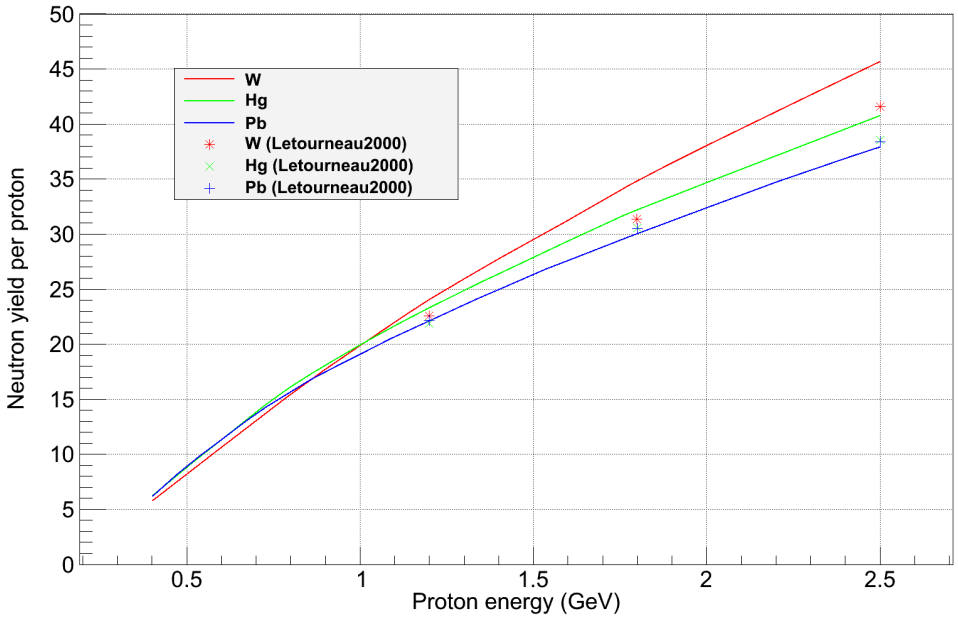

Figure 4.3: Comparison of neutron yield in Pb, Hg and W due to protons with the experimental data

Figure 4.4 shows neutron yield normalized per incident proton energy. This figure illustrates the energy cost required for production of neutrons. From the figure, one can see that the neutron yield for the three materials, increase with energy, reaches a maximum at about 800 - 1200 MeV and starts decreasing at higher energies. The conclusion is that the neutron yield is most economical, when the proton energy is about 800 - 1200 MeV. This is because, pion production dominates at the cost of neutron production above 1GeV [Armstrong et al., 1981]. Hence, this could be considered as a reasonable upper limit of proton energy in an ADS. According to the table 4.2, nuclear collision probability also reaches saturation value in this energy range. The fact that higher beam energies require larger accelerators, also justifies the proton energy to be about 1 GeV.

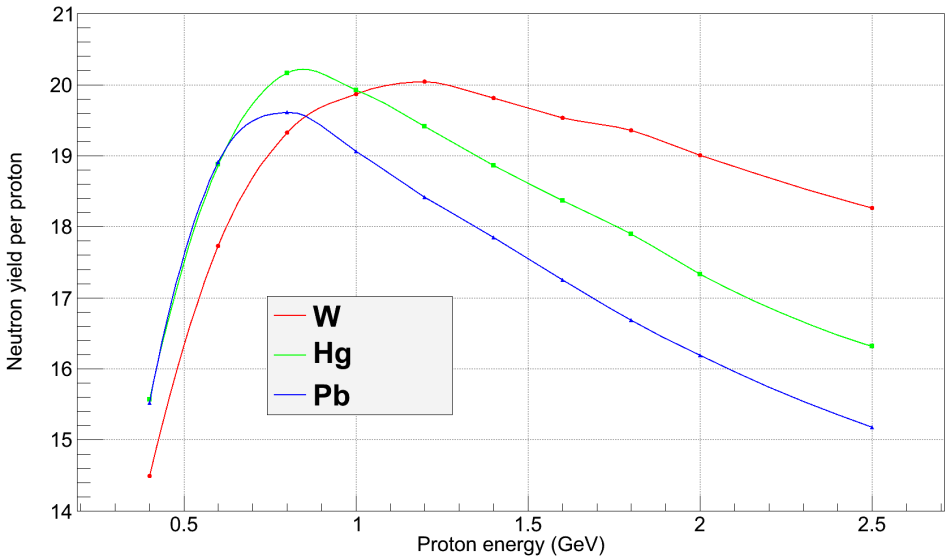

Figure 4.4: Neutron yield in Pb, Hg and W normalized to proton energy

4.2 Effect of Target Material and Geometry on Neutron Yield

4.2.1 Target Material

Probably the most important criteria while screening spallation materials is the neutron multiplicity. Since neutrons are the main product and their high multiplicity leverages spallation in comparison to others (table 2.1). Cugnon shows that the neutron multiplicity $< n >$ in proton induced reactions is roughly a linear function of the target mass (A_t) and is slowly increasing with incident energy (E_p) [Cugnon et al., 1997].

$$< n >= (0.0803 + 0.0336\, lnE_p)\, A_t \tag{4.6}$$

According to the above formula, for a nominal E_p of 600 MeV (as in AGATE) and to obtain $< n >$ of about 10 neutrons per incident proton, A_t of the target material has to be about 160. From the periodic table, naturally occurring and stable elements with mass number greater than 160 includes some lanthanides, period 6 elements and actinides. Keeping in mind about the quantity of spallation material required (from several kilograms to some tons), lanthanides are a scarce source from the economic exploitation point of view [USGS, 2012].

Fissile actinides, in contrast are very attractive because neutrons are created due to fission in addition to spallation neutrons, increasing the net neutron yield. For example, spallation in ^{238}U yields nearly twice as many neutrons per proton than in other heavy metals [Bauer, 2001]. However, as it can be seen from figure 4.5, natural U spallation products have extended mass numbers in comparison to spallation products from other materials. The sharp peak in the mass number curve for U spallation products indicate that much more actinides (nuclear waste) are formed, which is undesirable in spallation target to be implemented in a nuclear waste transmutation system. This observation is also supported by the theoretical description of the general magnitude of induced radioactivity in spallation targets [Armstrong et al., 1981],

$$A^s \approx 0.5\, MCi/mA, \text{ for non-fissionable targets} \tag{4.7}$$

$$A^s \approx 5\, MCi/mA, \text{ for fissionable targets} \tag{4.8}$$

where A^s is the saturation activity. Moreover, from operational experiences it is known that U spallation target suffers with severe service life shortage [Watanabe, 1999].

Table A.1 lists the stable elements from period 6 of the periodic table whose mass number is greater than 160. All the target materials in the current spallation sources around the world belong to this period viz., lead, mercury and tungsten. Bismuth used in LBE, to reduce the melting point, is responsible for the production of radiotoxic and volatile ^{210}Po about 1000 times higher than in lead [Wiehr, 2003] and is a potential safety concern [Russell et al., 1995]. Rhenium, Osmium, Iridium and Platinum are some of the rarest elements on earth's crust. Tantalum has already been proposed as a spallation target [Villagrasa-Roussel et al., 2006] and is used to clad tungsten targets (table 1.3) when water is used as the coolant. High radioactivity and after heat in tantalum, due to its relatively high neutron absorption cross section is a disadvantage. Gold is proposed in the form of LGE as an alternative to mercury and LBE, respectively because of its lower chemical toxicity and smaller amounts of alpha-emitting radionuclides in residues [Medarde et al., 2011]. The remaining two elements, hafnium (high MP) and thallium (low MP) , are suitable candidates for solid and liquid spallation targets respectively, which probably have not been explored so far.

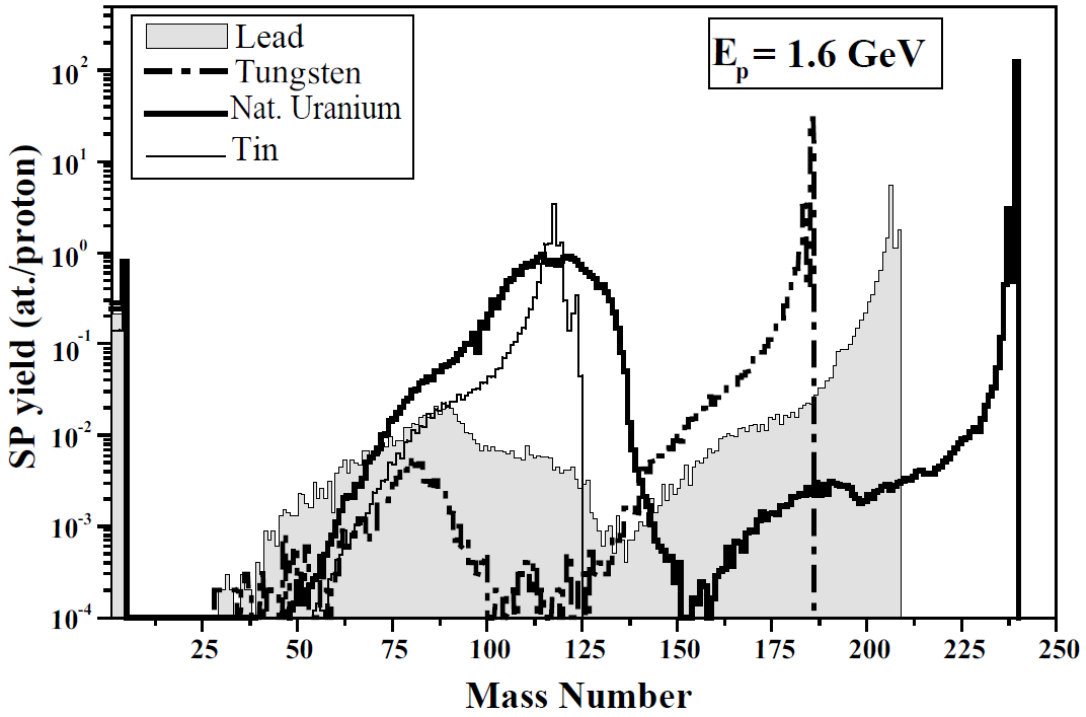

Figure 4.5: Mass number distribution of spallation products in Pb, W, ^{nat}U and Sn targets irradiated by 1.6 GeV protons [Stankovsky et al., 2001]

Tin, probably is the only low mass number material that has been considered as a spallation target [Atchison et al., 2005]. The use of lead-tin alloy reduces corrosion and from figure 4.5, it is visible that fewer spallation products are formed but at an obvious reduction in the neutron yield. Inadequate mechanical properties and operational lifetime has also been reported. From the figure, it can also be seen that the mass number of

spallation products is extended in case of lead in comparison to tungsten. It is natural because of the lower mass number of tungsten. This gives tungsten target an edge over lead target, when the question is about the presence of ^{210}Po in the residue. Tungsten also has very high melting point (3400 °C), making it an ideal candidate for a solid target. However, heat removal problems are generally associated with the solid targets.

4.2.2 Target Geometry

Other than the target dimensions, shape also influences the intensity and spatial distribution of neutron yield [Watanabe, 2003]. For 1.5 GeV protons on cylindrical and flat targets of Hg and LBE, neutron yield is comparatively higher in the latter case. In this section, cylindrical targets are studied for neutron yield as a function of radius and length.

Neutron Yield as a Function of Target Radius

Using the 4π-Berlin Neutron Ball, experimental values are available for neutron yield for different proton energies, target materials and dimensions [Letourneau et al., 2000]. Results of the simulation done according to this experiment, for tungsten target of 35 cm in length, is shown in figure 4.6 for different radii and proton energies. The maximum difference in the results between the experiment and the simulation is about 10%, for radius of 4, 6 and 7.5 cm.

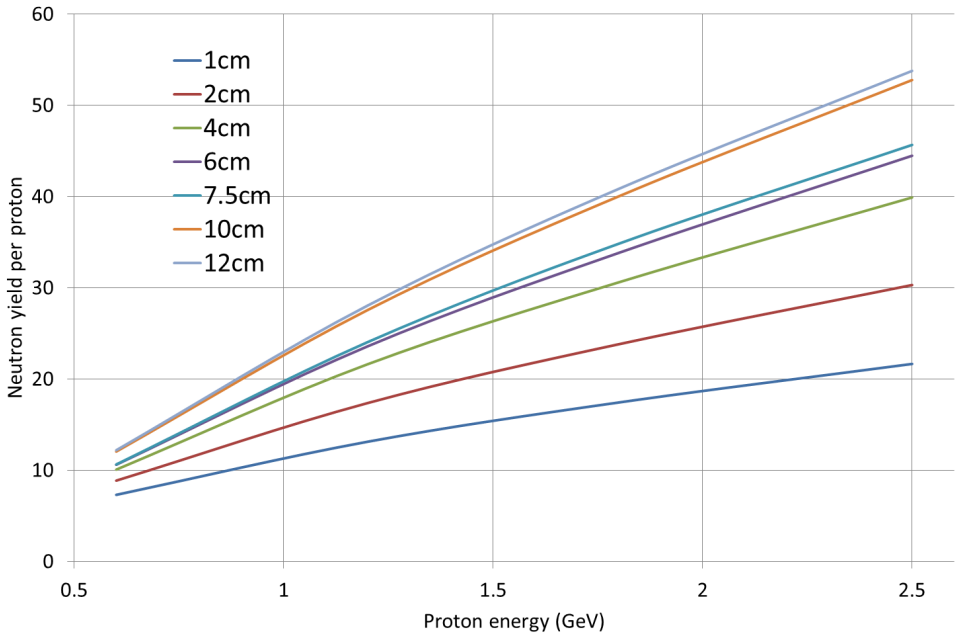

Figure 4.6: Neutron yield due to protons in W targets of different radii

From the figure, it can interpreted that at lower energies, the neutron yield is more or less independent of the target radii, except for 1 cm radius. This situation is imaginable, because the target with a smaller radius lets the cascade particles escape, inhibiting further interactions. At higher energies, target with 2 cm radius also gives relatively lesser yield and so on. It is interesting to see that for 10 and 12 cm radius, the neutron yield is consistent with each other. This is due to the parasitic absorption of neutrons outnumbering the leaking neutrons at larger target radii. So, if not pretty much accurate, target of radius 10 cm is a good value to start with.

Neutron Yield along the Target Length

The intensity of proton beam decreases exponentially along the axis of the target, so does the power deposition and the neutron yield [Bauer, 2001]. This is due to the competing processes such as ionization losses below 100 MeV, pair production and other effects at the high energy end. Parameterization of the axial distribution is obtained by the formula

$$n(z) = N_0 \left(1 - exp\left(\frac{-z - z_0}{\lambda_b}\right)\right) exp(-z/\lambda_a) \tag{4.9}$$

where n, N_0 could be neutron yield, power density, temperature or radial power integral. The parameters, z_0 is the extrapolation length (distance in front of the target at which the curve would cross zero), λ_b the buildup length and λ_a the attenuation length. The parameters depend on the target geometry and neutron energy range.

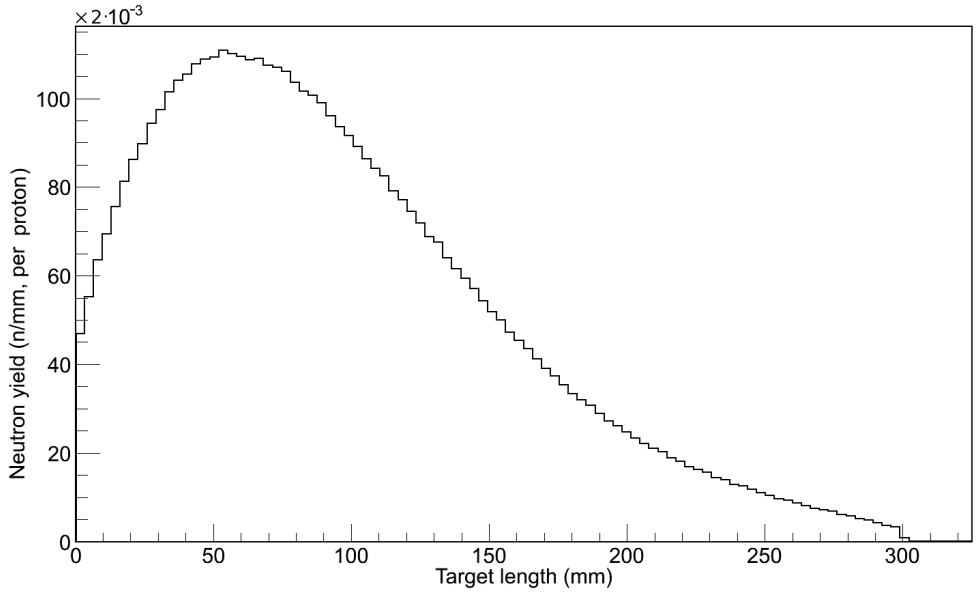

Figure 4.7: Neutron yield along the length of W target with 600 MeV protons

Neutron yield along the lateral surface in a tungsten target of 30 cm in length and 10 cm radius due to 600 MeV protons is presented in figure 4.7 (neutrons leaking from the forward and backward surface not shown). As expected by theory, after the build up of neutrons near the front face of the target, neutron yield decreases gradually along the length. Experimental results from figure 4.8, also indicates that the neutron production becomes stagnant at extended length of the target.

Total energy deposition is plotted in figure 4.9 for the same target block. The curve is characterized by a drastic decrease in energy deposition at about 15 cm, which in reality co-relates to Bragg peak. The energy deposition is dominated by cascade reactions (neutron production) up to this range and further downstream is due to the interaction of secondary particles as a result of the former, which still produces neutrons but at a lower probability. Hence, explaining the behavior of neutron yield curve in figure 4.7. This phenomenon at 15 cm, in other words is the range of 600 MeV protons in tungsten, responsible for about 80 % of nuclear collisions (table 4.2). So the target whose length is about the range of incident protons, should be sufficient for reasonable neutron production. This ensures that the incident protons interact completely within the target. The distance

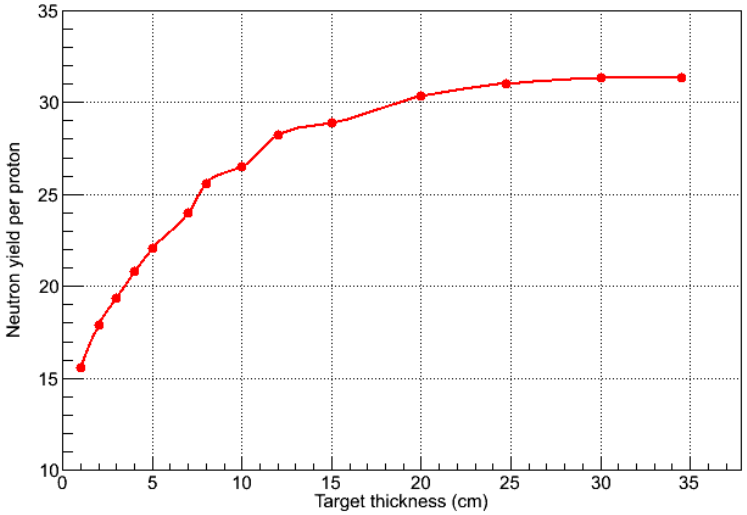

Figure 4.8: Neutron multiplicity due to 1.8 GeV protons on a W target of 15 cm in diameter and various thicknesses [Letourneau et al., 2000]

between the intermittent peaks decreases with decreasing proton energy and is related to the interaction length of protons in the material as a function of energy.

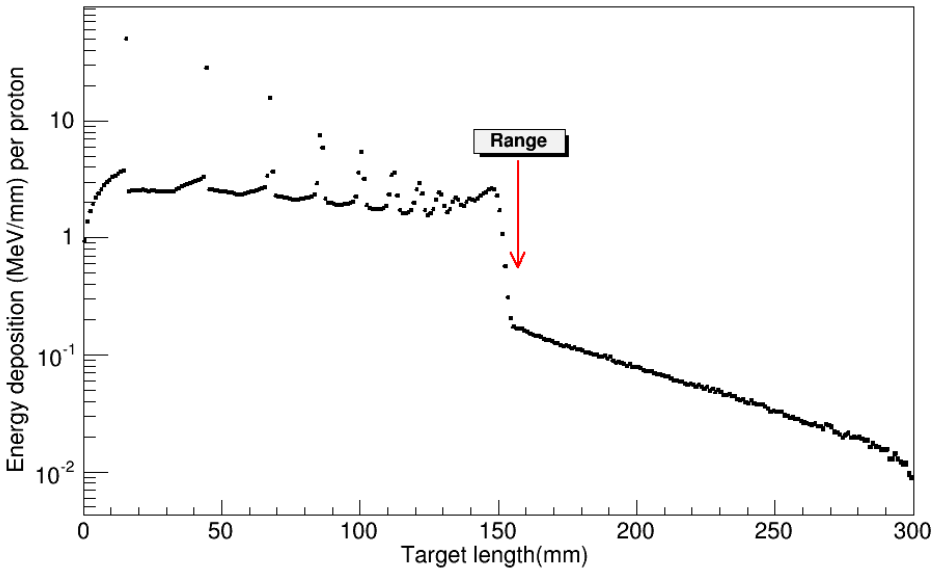

Figure 4.9: Energy deposition along the length of W target with 600 MeV protons

4.3 Particle Production in the Target

The most promising target materials, i.e, W, Hg and Pb are studied under the action of 600 MeV protons. The target dimensions are about 35 cm in length 7.5 cm radius. Energy spectra of neutrons, gammas and spallation products are discussed. While all the spectra are important from the radiation protection perspective, recoiling spallation products are also the main cause of radiation damage in the target. Since, pions are

relatively negligible in number and protons are mostly stopped within the target, their consequences are omitted in this section.

4.3.1 Neutron Production

Figures 4.10 and 4.11, respectively show the total neutron production in the target and the neutron yield, i.e., the number of neutrons that managed to leak from the target. Amongst the three targets, W produces the highest number of neutrons, followed by Hg and Pb. The descent in neutron production is according to the material densities. However, on closely examining figure 4.11, the neutron yield, seems to be indifferent to material property at 600 MeV. Because more neutrons are lost in W, followed by Hg and Pb, again relating to material density. For this energy and target types, material density is a boon and bane at the same time. For transmutation, it is interesting to note the hard energy spectra of neutrons, in the range of some MeV, ideal for incinerating MAs.

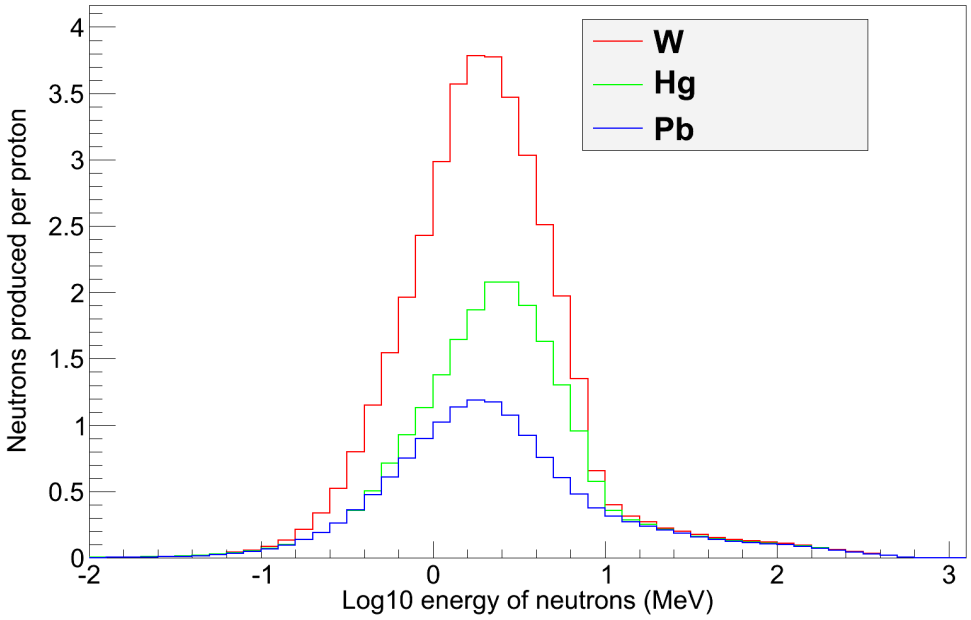

Figure 4.10: Neutron production in W, Hg and Pb targets due to 600 MeV protons

At higher energies (figure 4.3), W excels in neutron yield in par with others. This is probably due to the multiple scattering through small angles. A charged particle traversing a medium is deflected by many small-angle scatters due to Coulomb scattering from nuclei, and for hadronic projectiles, the strong interactions also contribute to multiple scattering [Eidelman et al., 2004]. Multiple scattering of protons results in small, cumulative directional changes that ultimately cause spatial broadening of the original focused beam. Range of proton increases with energy, hence increasing multiple scattering of protons, away from the axis of the beam, increasing beam spread. Hence, some neutron production sites are shifted closer to the outer surface of the target, thereby, leading to higher neutron leakage. Figure 4.12 actually shows that that the incident protons stray away from the beam axis with increasing incident proton energies in a tungsten target [Magill, J. et al., 2007].

Table 4.3 summarizes the neutron numbers. A significant portion of neutrons are reflected from the front face of the target in comparison to the side-leaked ones. This can be explained as there is a neutron buildup near the front face of the target, neutrons

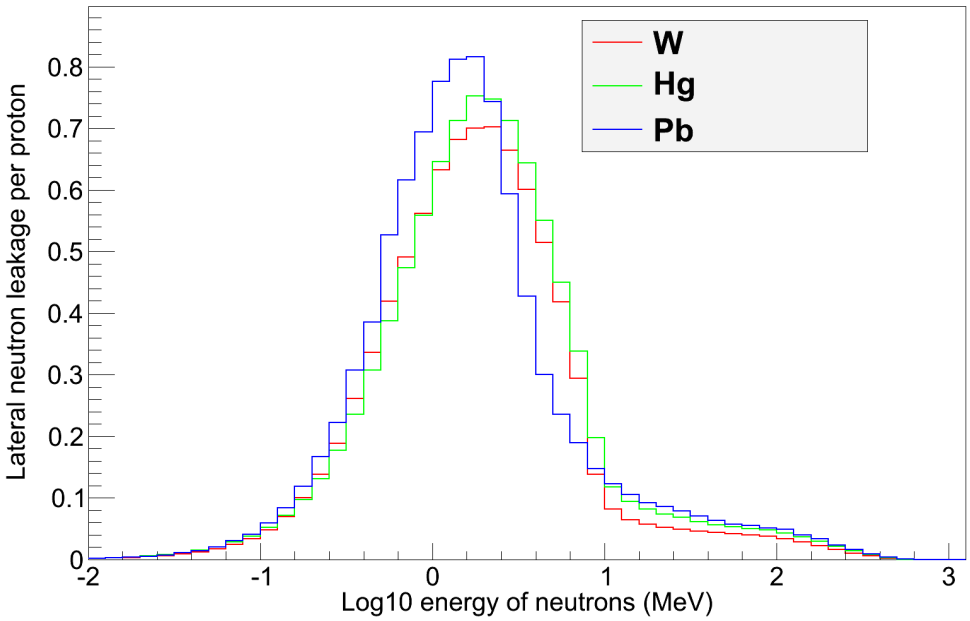

Figure 4.11: Neutron yield in W, Hg and Pb targets due to 600 MeV protons

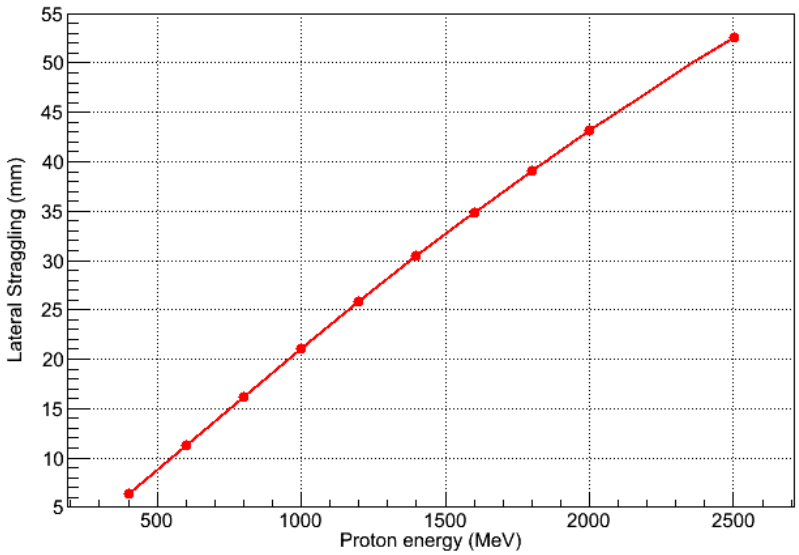

Figure 4.12: Lateral straggling of incident protons of various energies in a W target

scatter more easily backward than in any other directions. This is a major drawback provided that the lateral direction is more suited for application of neutrons through instruments or sub-critical core and that the backward leaked neutrons may reach the beam tunnel causing activation problems in the beam line structures. In this regard, it is sensible to to create a flux-trap, such that the neutrons are not lost due to backward scattering using the segmented target concept, discussed in section 5.2.

Table 4.3: Neutron production and leakage in W, Hg and Pb targets due to 600 MeV protons

Material	Total Neutrons	Leaked	Forward	Backward	Side
Tungsten	39.06	11.63	0.05	2.86	8.72
Mercury	22.37	11.52	0.14	2.12	9.26
Lead	15.02	11.35	0.18	1.83	9.34

4.3.2 Gamma Production

Gammas are emitted either promptly during INC, or during de-excitation stage of the pre-fragments produced aftermath of spallation reactions. Figure 4.13, depicts the energy spectra of gammas produced in the target due to spallation reactions. Many high energy gammas with energy close to 1 MeV are produced. The energy range extends up to 100 MeV for all the three materials. High energy gammas need to be considered along with the neutrons for radiation shielding, as they penetrate deep into the matter because of their neutral charge. As seen from table 4.4, gamma production is similar in W, Hg and Pb. About 30 gammas are produced in the materials per incident 600 MeV proton.

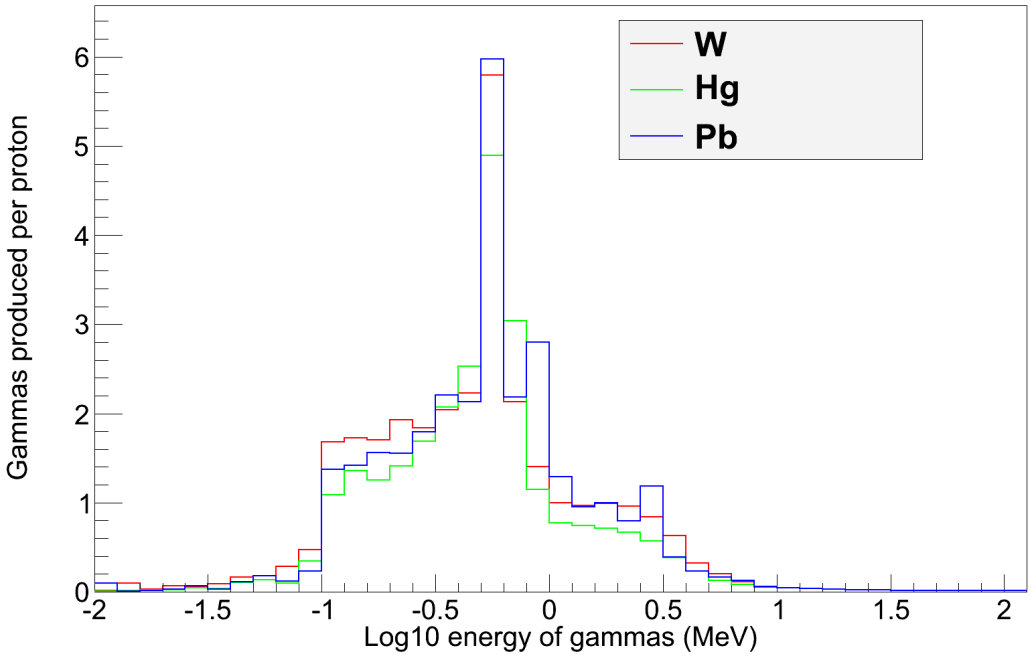

Figure 4.13: Gamma production in W, Hg, Pb targets due to 600 MeV protons

4.3.3 Spallation Residue Production

Residues produced in spallation reactions or spallation products (SP) cause significant radiation damage in the targets by introducing displacements in the material structures. Some spallation products are radioactive in nature, enforcing stricter radiation protection measures and disposal strategies. Figure 4.14 shows the energy spectra of spallation products. The energy is in the range of some keV. This is reasonable as the bulk of the energy is distributed to the lower mass ejectiles, such as neutrons or other light ions, in a nuclear reaction.

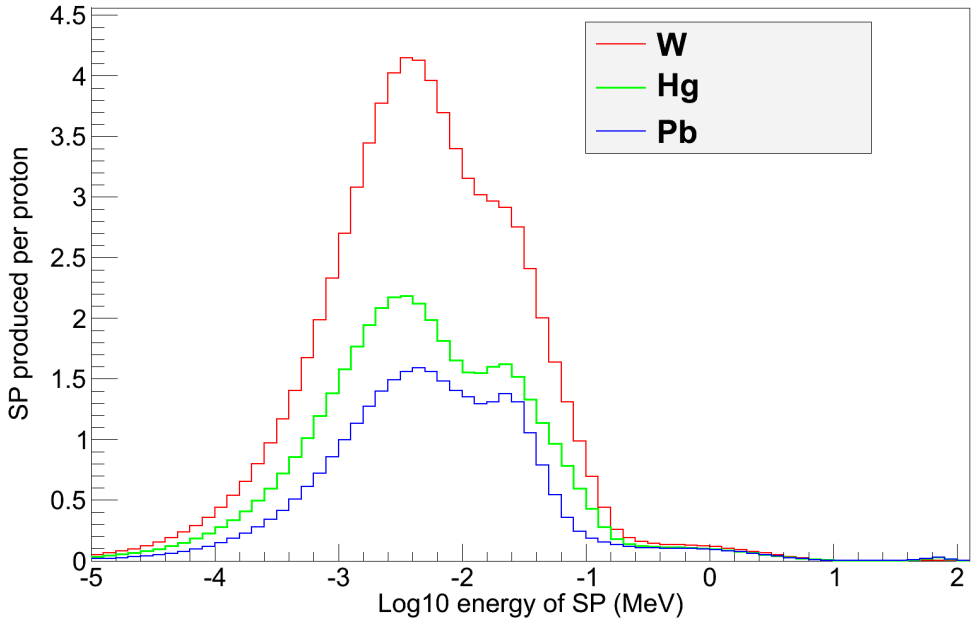

Figure 4.14: Spallation Products in W, Hg, Pb targets due to 600 MeV protons

Clearly, more spallation products are created in the W target. This can be related to the neutron production behavior (figure 4.10), to produce more neutrons, more impact with target nuclei is necessary, resulting in more spallation products. Table 4.4 displays the gammas and spallation products produced per 600 MeV proton. Number of gammas produced is fairly similar in all cases. In Pb, spallation products are more than 50 % lesser in comparison to W. An interesting point to be noted from the table is that two spallation products are required to produce a single neutron in the block targets, independent of material under consideration. A further analyis of activation products and their radiological implications is needed, in order to weigh the target prospects w.r.t. to spallation products.

Table 4.4: Gammas and spallation products produced in W, Hg and Pb targets due to 600 MeV protons

Material	**Gammas** per proton	**Spallation Products** per proton	**Neutron Production** per SP
Tungsten	30.30	76.08	0.51
Mercury	25.94	42.56	0.53
Lead	33.40	30.07	0.50

4.4 Energy Deposition Behavior in the Target

When a proton beam with a certain beam power interacts with the target, a part of the energy is lost along with the leaking particles and the rest is utilized in target heating. The energy loss of a heavy charged particle, such as a proton, is best described by the Bethe formula for stopping power. The secondary particles produced such as neutrons, gammas, electrons, etc., loose energy through a variety of nuclear mechanisms. Target heating leads to temperature rise and changes the functional properties of materials.

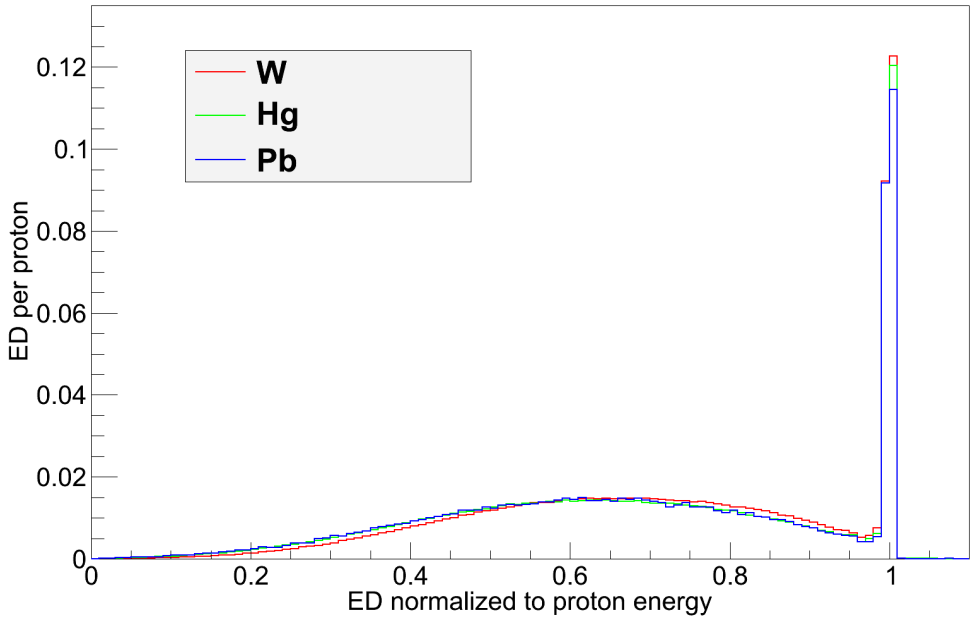

Figure 4.15: Total energy deposition in W, Hg and Pb targets normalized to beam energy

Some aspects of energy deposition (ED) along the length of the target is already made in subsection 4.2.2. Figure 4.15, shows the total energy deposited in W, Hg and Pb targets normalized per incident proton energy, 600 MeV. The energy deposition profile is about the same for all the materials. An observation in the figure is a wide distribution in the energy deposited, i.e., not all protons deposit the same amount of energy in the target. This phenomenon is attributed to energy straggling, due to the statistical nature (Gaussian shape) of nuclear collisions and amount of energy lost in each collision [Turner, 2007]. A similar analogy of range straggling can be applied, however, it is not large for heavy charged particles.

The other observation in figure 4.15, is that there is a peak at the extreme end on the right. This means, a significant amount of incident protons deposit all their initial energy in the target, i.e., there are no leakage particles. Unlike in the case of fission, the energy balance is limited to maximum beam power for a non-actinide spallation target. The numbers in table 4.5, quantifies the energy deposition in the target. According to it, for 600 MeV protons, about 70% of the beam power is lost into target heating in all the materials. About 87% of the target heating is due to protons, 7% due to electromagnetic (EM) particles, i.e., electrons and photons and the rest is due to neutron, pions and recoiling spallation products. Similar conclusions are drawn by Bauer [Bauer, 2001] about power dissipation in spallation targets (table 4.6).

For MW beam power, target heating is an extremely formidable situation, especially for solid targets. Very high operating temperatures can be reached and the material

Table 4.5: Energy deposition in W, Hg and Pb targets due to 600 MeV protons

Material	**Total Energy Deposit** MeV	**Proton Energy Deposit** MeV	**EM Energy Deposit** MeV
Tungsten	430.19	373.97	25.64
Mercury	417.29	365.71	21.52
Lead	414.24	360.55	25.61

properties can be compromised. It is not possible to advantageously manipulate nuclear collision as it is statistical in nature. A viable engineering solution would be to segment the target, letting the coolant to evacuate heat from the inside of the target and hence, reducing the operating temperature. This is in line with the segmented target concept

Table 4.6: Contributions from various particle types to energy deposition by 1.1 GeV protons on a slab target (76.5% Pb, 7% Al, 16.5% D2O)

Particle type	**Energy deposition**	
	MeV/proton	%
Primary protons	213	37
Secondary protons	233	41
Charged pions	17	3
Neutral pions	44	8
Muons	4	1
Spallation products	17	3
Spallation gammas	14	2
Low-energy neutrons ($\leq$ 15 MeV) (including secondary gammas)	29	5
	571	100

CHAPTER 5

Target Module Development

Target is the most important part of a spallation source system, be it neutron production for solid-state scattering research, or for nuclear waste transmutation, or for energy amplifying, or for basic science on neutrino and radioactive beam production [Filges and Goldenbaum, 2010]. The main aspects while optimizing neutron production in targets especially in high power accelerator applications are:

- Efficiency of neutron production and transport
- Heat removal
- Induced radioactivity and after heat
- Radiation damage
- Stress and fatigue

The first four points lie within the nuclear domain and have been analyzed in this work for a target, from the perspective of transmutation in an ADSS. In particular w.r.t. target engineering, the following goals are to be achieved:

Homogenized Neutron Field The AGATE sub-critical core is about 150 cm in length whereas the target thickness is about 18 cm (slightly longer than the range of 600 MeV protons in tungsten). Moreover, most of the neutrons are produced near the target head (figure 4.7). Neutrons emanating from the target resembles a point source when compared to the length of the fuel elements, increasing the power density in the core [Lamarsh and Baratta, 2001]. Hence, it is important to have an axially homogeneous neutron field distribution from the target, to uniformly illuminate the sub-critical core.

Hard Neutron Spectrum As seen in subsection 1.3.3, transmutation requires hard neutron spectrum, in order to burn the MAs. The target should be optimized to maximize fast neutron yield.

Efficient Heat Removal Increased power densities are reached in spallation targets, as significant beam power is lost to target heating (section 4.4). The target should facilitate efficient heat removal via gas cooling.
Additionally, nuclear analysis of proton beam window and beam stop is done, to compliment the system study of the spallation target module.

5.1 Beam and Target Material Specification

5.1.1 Beam Parameters

According to table 1.2, linac or cyclotron is used to deliver 600 MeV protons on to tungsten target in AGATE system. As discussed in section 4.1.1, at 600 MeV, protons are the most attractive projectiles for neutron production. The speed of 600 MeV protons corresponds to about 80 % the speed of light. This is also technically feasible and economically viable. At these energies, it is desirable to have higher proton current in ADS, to maximize neutron yield. For instance, the ring cyclotron in PSI, is already capable of delivering protons of about 600 MeV at over 2 mA, or the accelerator at SNS delivering 1 GeV protons at 1.4 mA.

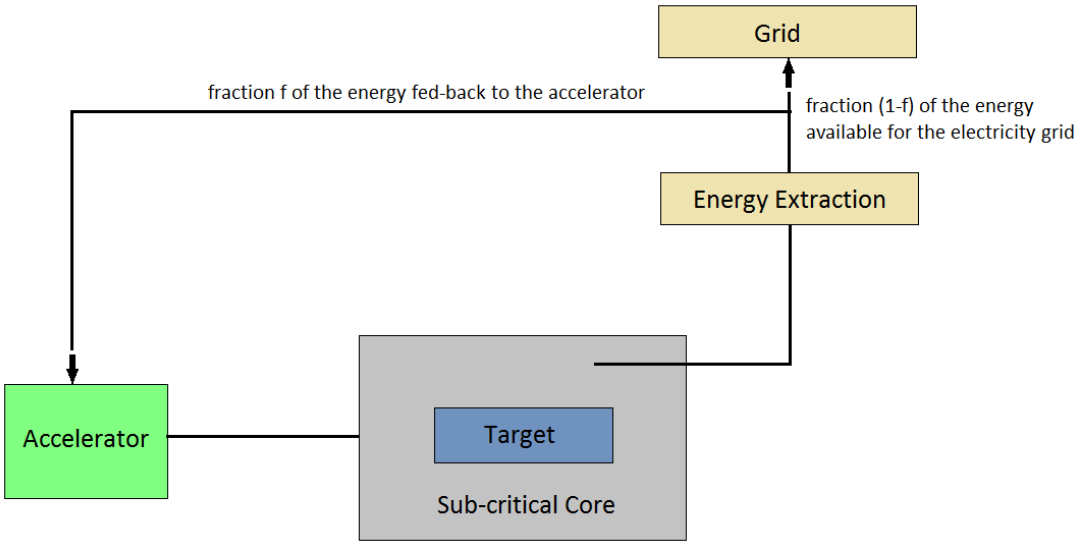

Figure 5.1: Scheme of an accelerator-driven sub-critical system (adapted from [Kadi, 2003])

Direct usage of spallation neutrons for transmutation of nuclear waste is economically prohibitive. By enhancing neutron economy in a sub-critical core, fission power can be extracted. Provided that the part of the fission power is fed back to the accelerating unit, as depicted in figure 5.1, transmutation is made more economically efficient. The fission power P_{fi} in such a system is given by [Kadi and Revol, 2002]:

$$P_{fi} = \eta_{sp} \cdot \frac{\varphi^* \cdot k}{\nu(1-k)} \cdot \frac{i}{C} \cdot E_f \tag{5.1}$$

where, k = neutron multiplication factor
φ^* = source importance ($\approx$1.5)
ν = neutrons emitted per fission ($\approx$2.5)
E_f = energy generated per fission ($\approx 3.1 \times 10^{-11}$ J)
i = accelerator current
C = charge of a proton ($\approx 1.6 \times 10^{-19}$ C)
η_{sp} = spallation neutron yield
According to equation 5.1, for a given power, accelerator current is a function of neutron multiplication factor. For AGATE, with P_{fi} = 100 MW, assuming k = 0.97 and η_{sp} = 7

neutrons per incident proton, the proton current to be delivered by the accelerator on to the tungsten target is about 3.8 mA.

For simulations of target engineering, it is assumed that the beam is Gaussian in lateral directions, as shown in figure 5.2a, with $\sigma_r = 3$ cm. The beam footprint on target is assumed to be circular, as shown in figure 5.2b, giving a peak current density of about 0.035 p/cm^2 per incident proton, which corresponds to a proton flux of about 2.2×10^{14} p/s·cm^2 per mA.

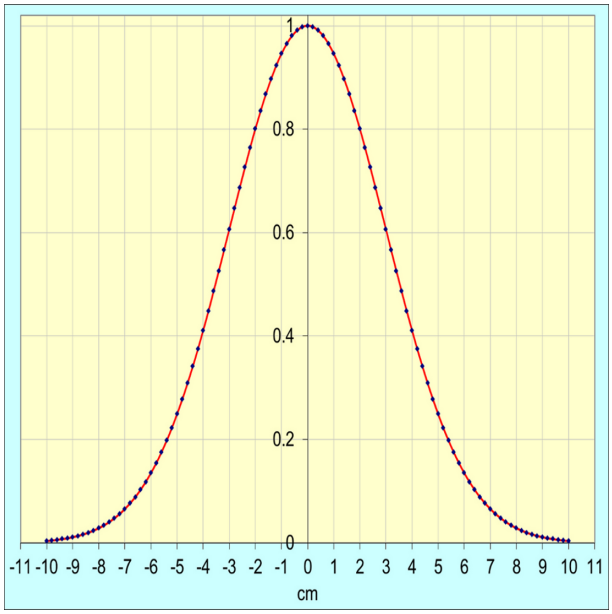

(a) Gaussian distribution of beam particles in lateral directions

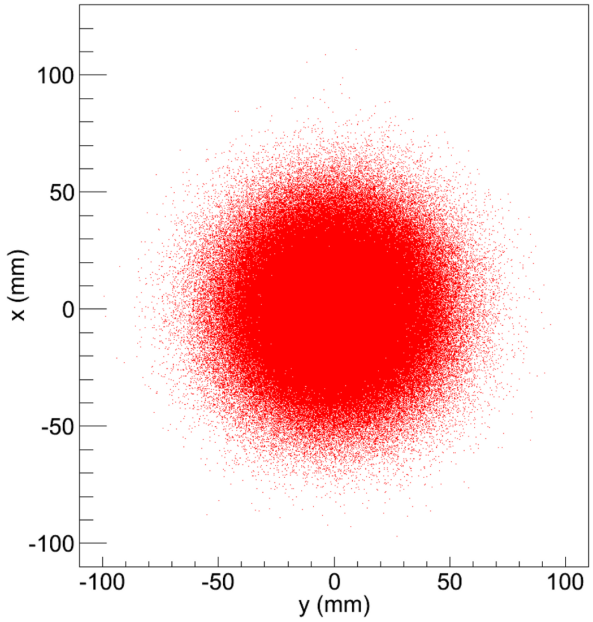

(b) Beam footprint on the target

Figure 5.2: Technical specification of beam parameters

5.1.2 Tungsten Properties

The desirable properties of a spallation target material, in general are [Broome, 1996, Bauer, 2010]:

- High atomic number
- High density
- High/Low melting point (solid/liquid)
- High thermal conductivity
- Chemically inert, low corrosion
- Resistance to radiation damage
- Low cross section for neutron absorption
- Good availability and low price
- Moderate activation and after heat production

In particular for solid targets, small thermal expansion coefficient to minimize thermal stress, good manufacturing and joining properties to other materials are also necessary. Tungsten is as an ideal candidate for solid spallation material, some of whose properties are listed in table A.3.

Tungsten is a grayish-white lustrous metal, which is a solid at room temperature. It has the highest melting point and lowest vapor pressure of all metals, and at temperatures over 1650°C has the highest tensile strength combined with excellent corrosion resistance and is attacked only slightly by most mineral acids [MTS, 2012]. Tungsten also exhibits good thermal conductivity even at elevated temperatures (130 W/(m-K) at 873 K).

For AGATE, the target material is pure tungsten (> 99.9 %) [AGATE, 2011]. This can be obtained, for example, as a semifinished product in the form of plates or rods. Stainless steels or titanium alloys can be used as structural materials. Tungsten corrodes with water under irradiation [Bauer, 2010], using helium as coolant is advantageous for this reason. Also, the activation of coolant can be avoided. However, the drawbacks include lower heat capacity of helium and high operational pressure in the target module.

From table 4.3, one can see that only a third of neutrons produced, leaks from the tungsten target for 600 MeV protons. This is because, for thick tungsten targets, neutrons of energy lower than 1 MeV increases [Abe, 1996], leading to their absorption based on the 1/v dependence of radiative neutron absorption cross section shown in figure 5.3. For tungsten, this effect is off-set by high neutron production and the leakage is comparable to other spallation target materials.

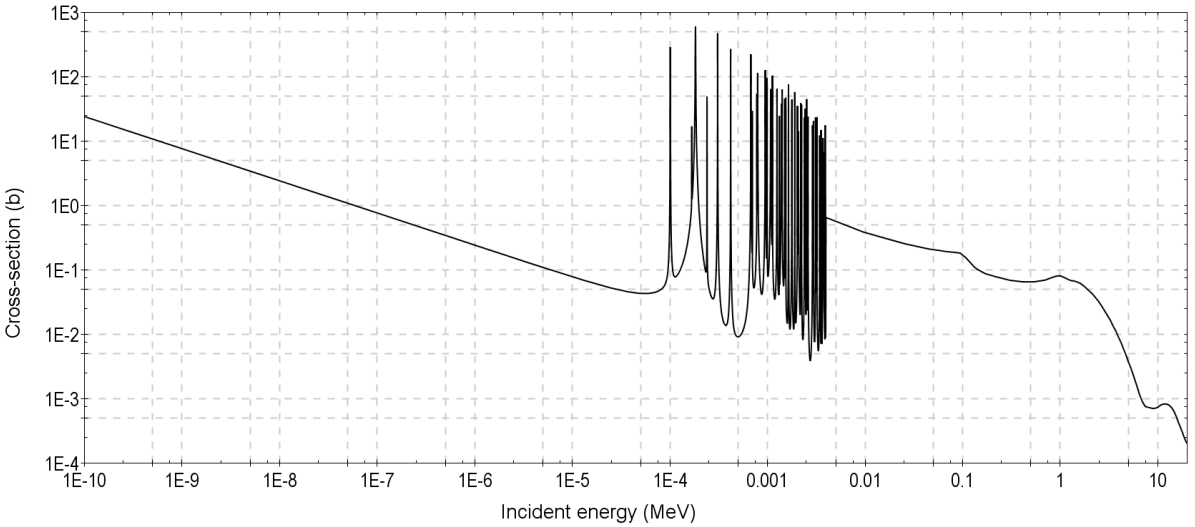

Figure 5.3: Radiative neutron capture cross section for ^{184}W (ENDF/B-VII.1)

Nuclear collision probability for 600 MeV protons with tungsten is about 80% (table 4.2). This probabilty reaches 100% above 1 GeV. Considering the practical availabiltity of 600-MeV accelerators at high current and substantial nuclear interactions at this energy, proton energy of 600 MeV emerges as a consistent choice for AGATE. The composition of natural tungsten assumed for simulation purposes is as depicted in table A.2.

5.2 Target Configurations

5.2.1 Segmented Target

As discussed in sections 4.3 and 4.4, segmentation of the monolithic target is envisaged as a feasible option to overcome heat removal problem and to enhance neutron leakage. In the split-target concept [Russell et al., 1995, Russell et al., 1997], a flux-trap is introduced in the solid block. Flux-trap refers to the spaces ($\geq$ 5cm) between the target segments of a split target. Incident protons are oblivious to the flux-traps and travel from target region to target region until the range is reached. The advantages of the split-target concept are as follows:

- Neutron production is spatially distributed deeper along the target axis.
- Neutron leakage is reduced from the front target surface. This allows the usage of large target diameters to reduce power densities.
- Increases low energy neutron leakage and reduces parasitic neutron absorption.
- Enables neutronic decoupling by employing absorbing material in and between target regions.
- Coolant circulation within the target is improved, thereby, making space for higher beam power.

The flux-trap also enhances leakage of high energy secondary particles, which otherwise would have caused spallation in the target material. A flux-trap of 14 cm lowers neutron leakage by 10% when compared to a solid target, for a parabolic proton beam profile. Chances that these leaked high enegy secondary particles cause stray radiation in structural material are also high. Neutron production also decreases as the flux-trap gaps increase. Further enhancement to split-composite target is possible, where total neutorn leakage is the overriding criteria, rather than peak flux. Improvising the split-target by making it radially composite, increases both low energy neutron leakage and production.

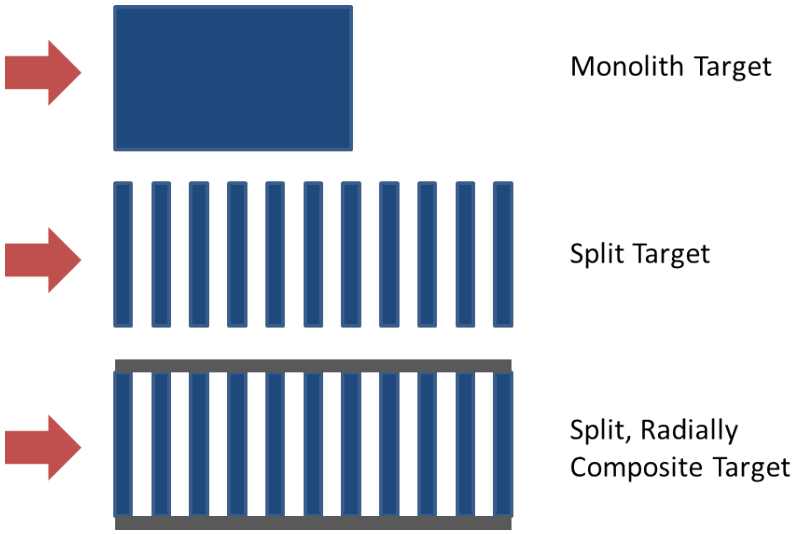

Figure 5.4: Diagram illustrating the split-target concept and its different configurations (adapted from [Russell et al., 1995])

5.2.2 Target Optimized for the AGATE Concept

The segmented target is optimized using monte carlo simulation. Though, the axial distribution of neutron yield from a monolith target could be estimated from equation 4.9, it requires parameters such as buildup and interaction length. Buildup length depends on the cascade development and cannot be quantified accurately using a deterministic approach, unless found out experimentally. The inclusion of flux-traps also alters the neutron yield behaviour.

In the monte carlo approach, simulations were iterated to determine the thickness of individual segments, such that each segment delivered about the same amount of neutron flux in order to homogenize neuron field along the length of the target. As a result, a target of radius 10 cm with 21 segments, each segment separated by 5 cm flux-trap and of varying thickness is obtained (figure 5.5). The thickness of each segment is shown in figure 5.6.

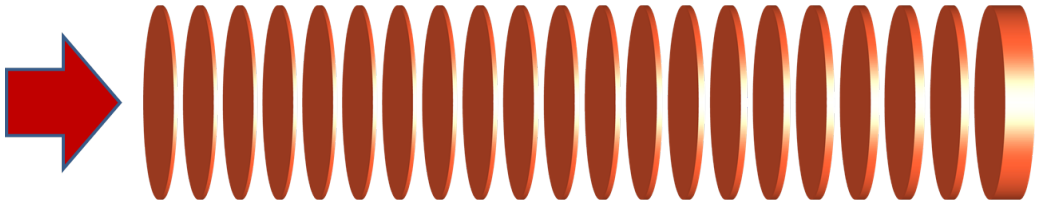

Figure 5.5: Optimized tungsten target for the AGATE concept

Thinner plates confront the beam directly, followed by segments of increasing thickness. A cascade of particles is created as the beam interacts with the target. The flux-traps allow the escape of some cascade neutrons and subsequent evaporating neutrons, hence maximizing overall neutron yield. Varying thickness of segments, thickness increasing along the beam path, homogenizes the neutron flux along the length of the target. The solid length of 18.8 cm ensures that the protons are stopped within the target. The final segment is intended to stop the residual beam, so that the damage to structural material is minimized in the forward direction w.r.t. the beam. The flux-trap of 5 cm not only elongates the target length by introducing space between the segments, but also letting the circulation of coolant thereby increasing the heat removal efficiency.

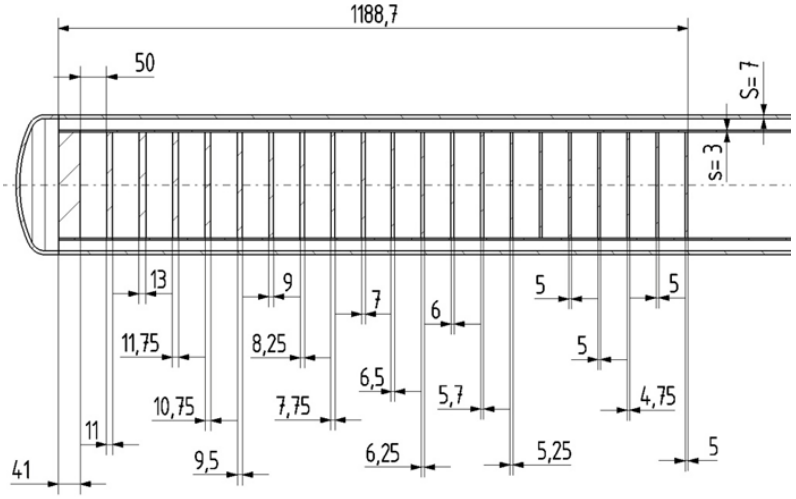

Figure 5.6: Individual segment thickness (mm) of the optimized target

5.3 Optimizing Power Density Distribution

The power density in a solid target reaches critical values and proves itself to be a bottleneck in the realization of a solid spallation target in the MW range. Hence, the parameters affecting power density are investigated in this section. Energy deposition in the target can be influenced by changing beam properties and/or targetry options. A combination of the below mentioned approaches can be implemented to substantially decrease power density.

5.3.1 Beam Options

Beam Transport

Beam transport system includes a series of dipole and quadrupole magnets, magnetic lenses, collimators and beam monitors, used to transport the beam to the desired location with desired shape and intensity at the destination [IAEA, 2008a].

Beam Focusing Quadrupole magnets can be used to smoothen the beam in accelerators to avoid 'hot spots', thereby distributing the beam more uniformly over the target surface. Increase in the area of beam footprint decreases the power density in the target due to beam energy deposition.

Wobbling and Rastering By wobbling and rastering the beam over the target surface, beam footprint shifts with time, overall lowering the power dissipation in the target. Dynamic beam delivery systems are required to enforce this technique.

Beam Energy

Figure 5.7 shows the energy deposition in W, Hg and Pb targets (35 cm length and 7.5 cm radius) due to different proton energies. Proton energy deposition in the targets decrease with increasing proton energies. For instance, the fraction of proton energy deposited in the W target decreases by about 15 % by increasing proton energy from 600 MeV to 1 GeV.

According to figure 4.4, the energy cost of neutron yield increases over 1 GeV and this energy can be considered as a reasonable upper limit of proton energy. The neutron yield increases at higher proton energies, which implies that lower proton current is required to produce the same number of neutrons at lower proton energy. Hence, decreasing power density as it is proportional to the proton current. Increasing beam energy is also desirable than increasing the current from the radiation protection point of view, as the number of stray particles in the beam tunnel increases at higher current.

5.3.2 Targetry Options

Target Material Density

Effect of target material density was studied for a tungsten target of 40 cm in length and 10 cm radius, due to 600 MeV protons. The results are tabulated in table 5.1. Decreasing density decreases the maximum power density proportionally in the target. This is due

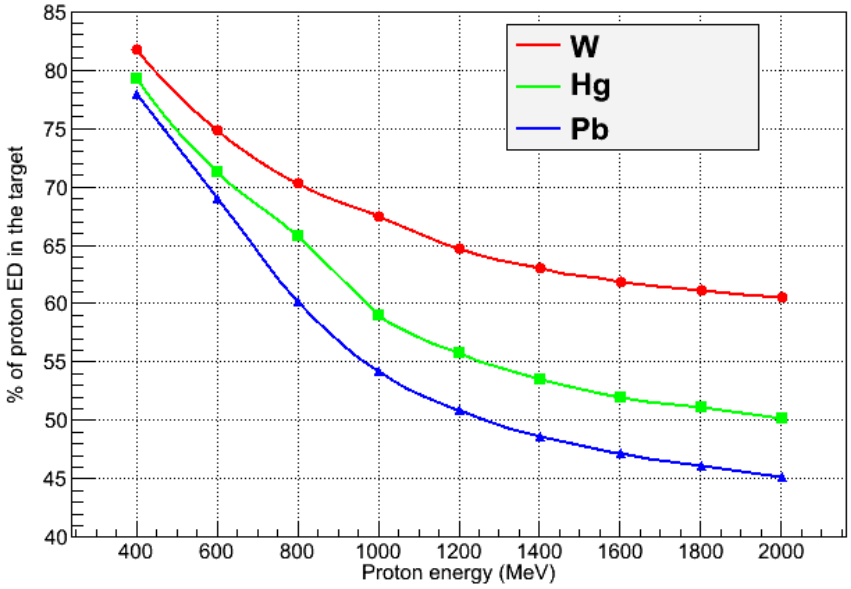

Figure 5.7: Energy deposition in W, Hg and Pb targets due to protons with different energies

to the fact that the total stopping power [Magill, J. et al., 2007] decreases, letting the protons to traverse a longer range in the target material.

Table 5.1: Effect of target material density on power deposition

Density (g/cm^3)	**% of Theoretical density**	**Max. power density** (kW/cm^3)	**Total stopping power** MeV/cm
19.3	100%	3.33	26.85
17.4	90%	2.83	24.20
11.6	60%	1.92	16.14

Tungsten with material density of 60-70 % of the natural density can be obtained using sintering methods [MTS, 2012]. Since the range of protons in low density tungsten is longer, the target length has to be accordingly adjusted. This obviously reduces the leaking neutron density, but the target neutronics at reduced material densities is yet to be investigated.

Target Radius

Increasing target radius, increases the overall volume in which the energy is deposited. Hence, decreasing the power density. This can be additionally combined with beam focusing, by delivering a flattened beam on to the target surface. In subsection 4.2.2, it is seen that the neutron yield increases with target radius up to an upper limit beyond which neutron absorption dominates in the target.

Rotating Target

Rotating the target w.r.t. beam is an alternative to wobbling and rastering, with the same intention of shifting the beam footprint with time, to reduce power deposition. Probably, the first attempt to implement a rotating target was for the German spallation neutron source project, SNQ [Armstrong et al., 1981]. The target is a flat cylinder of tungsten as in figure 5.8, for a 3 MW spallation source [McManamy et al., 2010]. For this particular design, tantalum clad tungsten target of 1.2 m diameter is rotated at a speed of 30-60 rpm to avoid the overlapping of beam pulses. Tantalum cladding allows water to be used as coolant significantly reduced remote handling requirements. Neutronic performance of the target is equivalent or better than the concurrent liquid mercury target at SNS.

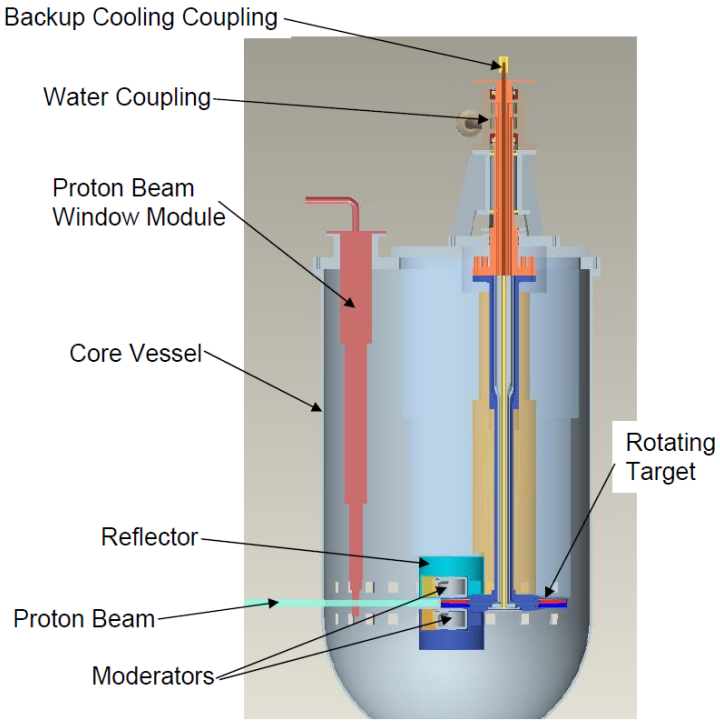

Figure 5.8: Rotating tungsten target arrangement of a 3 MW spallation source [McManamy et al., 2008]

Since the conceived material damage in the rotating target is low, service life of the target can be greatly enhanced. For instance, a service life of several decades is achievable using a rotating target of some 50 cm diameter in a medium power (500 kW) spallation source [Bauer, 2010]. Fins can be engraved on the target periphery to improve heat exchange with the coolant.

Inclined Target Segments

Inclining the target segments w.r.t. the beam, increases the total area on the target which the beam sees. For instance, inclining the segments by an angle of 30°, increases the lateral dimension by a factor of two. Since power density is inversely proportional to the square of the lateral dimension, power density decreases by a factor of four in this case.

Figure 5.9 illustrates the effect of inclined segment on the beam profile. A beam of circular cross section as seen by the vertical segment is projected on to the inclined

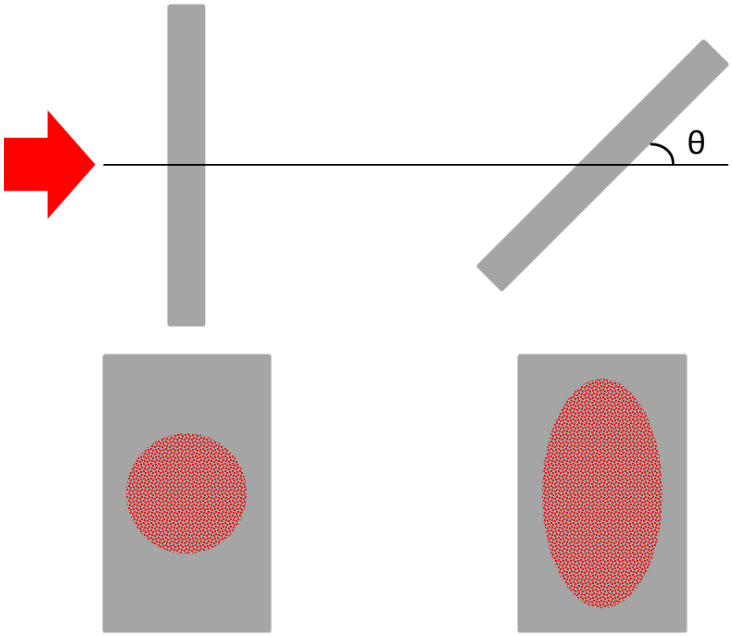

Figure 5.9: Schematic illustrating the effect of inclined target on the beam footprint

segment as a beam of elliptical cross section, increasing the overall area of beam footprint on the target. Playing with the curvature of the segments to adjust to the curvature of the beam is also a solution to decrease power density [IAEA, 2008a]. The closer the plate matches the beam curvature, the better is the distribution of the beam along the plate.

5.3.3 AGATE Pebble Bed Target

Fluidized Target

A single solid target can barely survive beam power of greater than 1 MW, so the solid target has to be degraded either as [Efthymiopoulos, 2011]:

- Fluidized powder targets, or,
- Granular targets (pebble bed), or,
- Solid wire targets

In MW class spallation targets, other than power density and radiation damage, thermal stress is also a limiting criteria for target performance. By implementing granular targets, the thermal stress is reduced as there is no stress transmission between the beads. A further transition to fluidized powder is possible, bridging the gap between the solid and liquid targets (see figure 5.10).

Flowing powder target is attractive because of the following reasons:

- the material is intrinsically damage proof even at high power densities
- no cavitation as in liquid targets
- high power densities can be absorbed without material damage
- shock waves constrained within the material grains

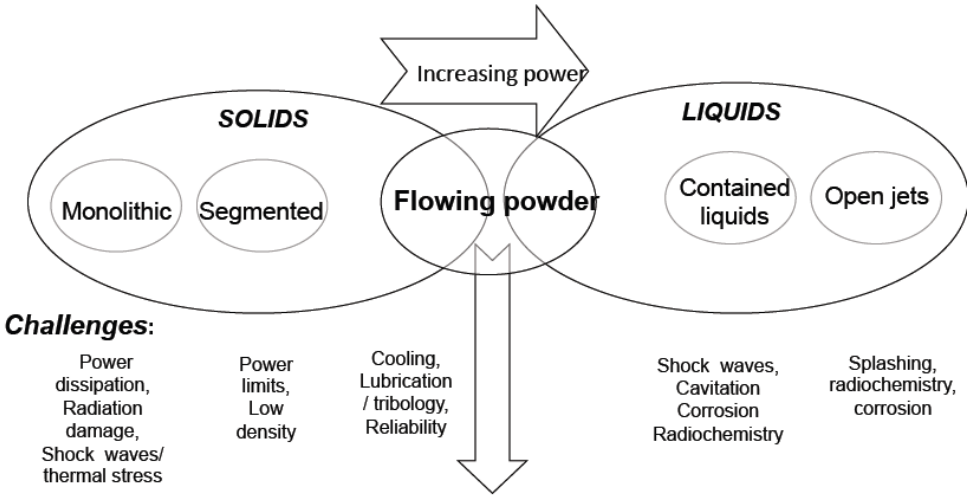

Figure 5.10: Flowing powder target as a solution to the challenges at high power [Efthymiopoulos, 2011]

- high heat transfer
- can be pumped away, cooled and externally circulated
- fluidized beds/jets is a mature technology

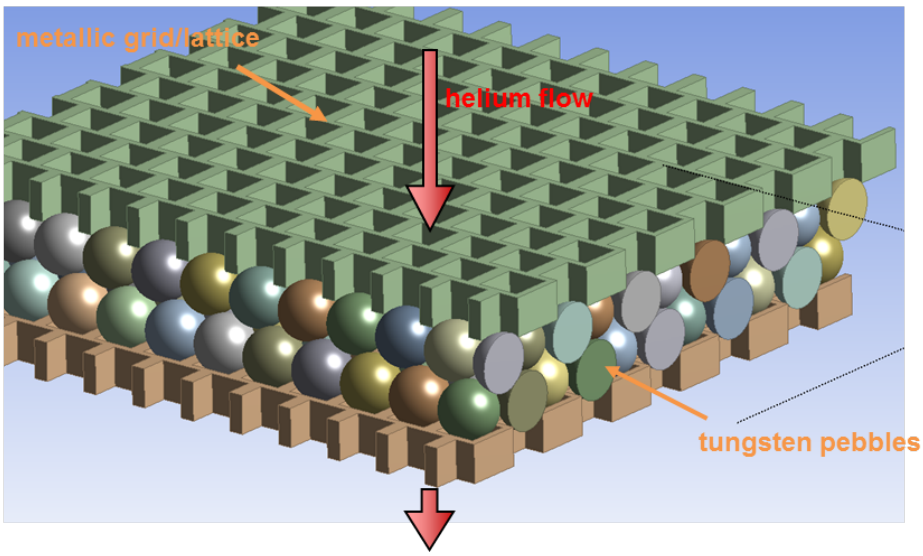

Figure 5.11: First segment of the optimized tungsten target fluidized using layers of pebbles (pebble bed target)[AGATE, 2011]

For the AGATE concept, fluidizing the target using pebble bed was the chosen strategy to minimize power density in the target. With an optimum ratio of volume to surface, heat transfer can be best realized by a densely packed pebble bed. Pebble bed pack with an assumed void content of 40 % gives rise to extremely high heat transfer coefficient. Figure 5.11 illustrates the principle of densely packed layers of tungsten pebbles enclosed in a grid/lattice structure corresponding to the first segment of the target. Depending

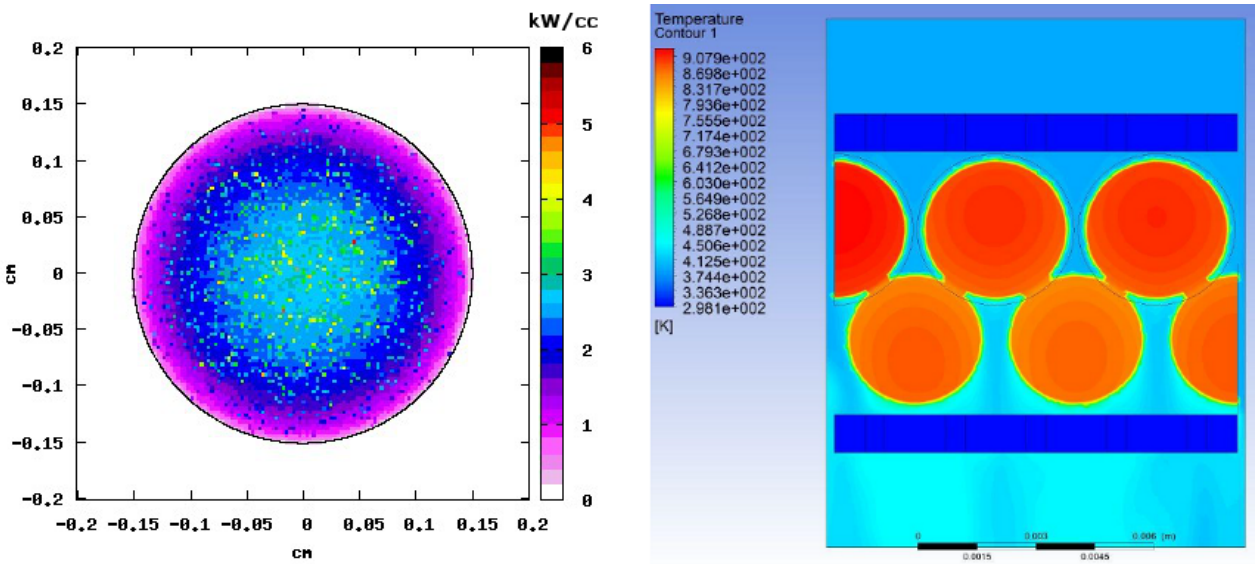

(a) Power density in a pebble

(b) Temperature profile in the first segment

Figure 5.12: Simulation of power density distribution in a pebble and temperature profile in the first layer of the pebble bed target

on the pebble diameter, the maximum temperatures in a pebble can be kept below the recrystallization temperature of tungsten.

Thermal hydraulic studies of the pebble bed target have been performed during the AGATE design study [AGATE, 2011, Coninx, 2011] for pebble diameter of 3 mm. Figure 5.12a shows the power density distribution in such a pebble from the FLUKA simulation. At a 600 MeV proton current of 5mA, the maximum power density in the target is about 3.3 kW/cm^3. Temperature profile in the first segment of the target is calculated for maximum power density of 5 kW/cm^3 with helium mass velocity of 2.8 kg/s at an inlet pressure and temperature of 60 bar and 120 °C respectively. The temperature profile in the target is displayed in figure 5.12b.

A maximum temperature of about 670 °C is reached in the segment, which is well below the recrystallization temperature (1350 °C) and melting point (3410 °C) of tungsten. Further design options of fluidizing the target segments using perforated plates, meshes and wires or rods made up of tungsten were also considered during the AGATE design study.

CHAPTER 6

Nuclear Simulation of the Target and Auxiliary Components

6.1 Particle Transport Simulation in the Target

6.1.1 Monolith Target

Nuclear analysis of a solid block of tungsten, whose dimensions are 18 cm in length and 10 cm radius, is done as a first step in design to learn the basic characteristics of neutron and energy deposition due to 600 MeV protons. Systematics study of neutron leakage and energy deposition along the length of a tungsten target are shown in figure 4.7 and 4.9 respectively. Neutron energy spectrum from this monolith tungsten is compared to that of optimized tungsten target in figure 6.7.

Figure 6.1 shows the power density distribution in the monolith target. Though the target length is 18 cm, energy deposition reduces drastically at about 15 cm. This length corresponds to the range of 600 MeV protons in tungsten. The drastic decrease in energy deposition near this length is due to protons loosing all their energy to ionization just before coming to halt at the end of the range (Bragg peak). Most of the energy is deposited within the first few centimeters of the target length. The maximum power density is about 0.79 kW/cm^3 per mA. This increases linearly with the proton current. Provided that the transmutation of nuclear waste (or any other application) requires proton current in the order of a few milliamperes, heat removal from the target is a major problem. The total beam power used up in heating the target is about 0.45 MW per mA. This signifies that about 70% of the beam power is lost into target heating, i.e., about 450 MeV of proton energy of 600 MeV.

Neutron flux profile for the monolith is displayed in figure 6.2. Just like the power distribution, neutron flux is concentrated in the initial part of the target length. It reaches to a maximum value of about 5.4×10^{14} n/s·cm^2 per mA at the center of the target. Lower order flux emanating from the target periphery is attributed to parasitic neutron absorption in tungsten. Neutrons leaking from the target leads to source brightness in the order of about 6.73×10^{16} n/s per mA. Higher flux can be achieved by simply increasing the 600 MeV proton current.

Monolith conical targets have also been studied [AGATE, 2010]. A conical target has the advantage of implementing windowless design, i.e. the target would also function as the barrier between the ultrahigh vacuum of the accelerator and the high-pressure area of the reactor. However, initial thermal calculations have shown that such a concept cannot

be cooled for the given proton beam power. Even in the best possible case, theoretical temperatures occur in the target that are well above the melting point temperature of the target material.

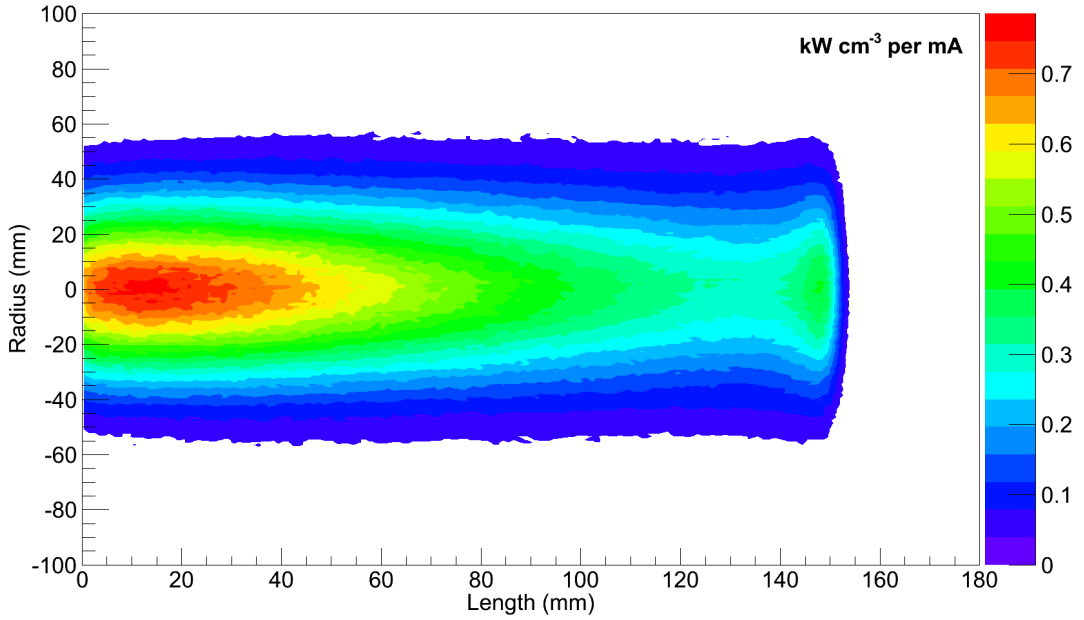

Figure 6.1: Power density in monolith tungsten target

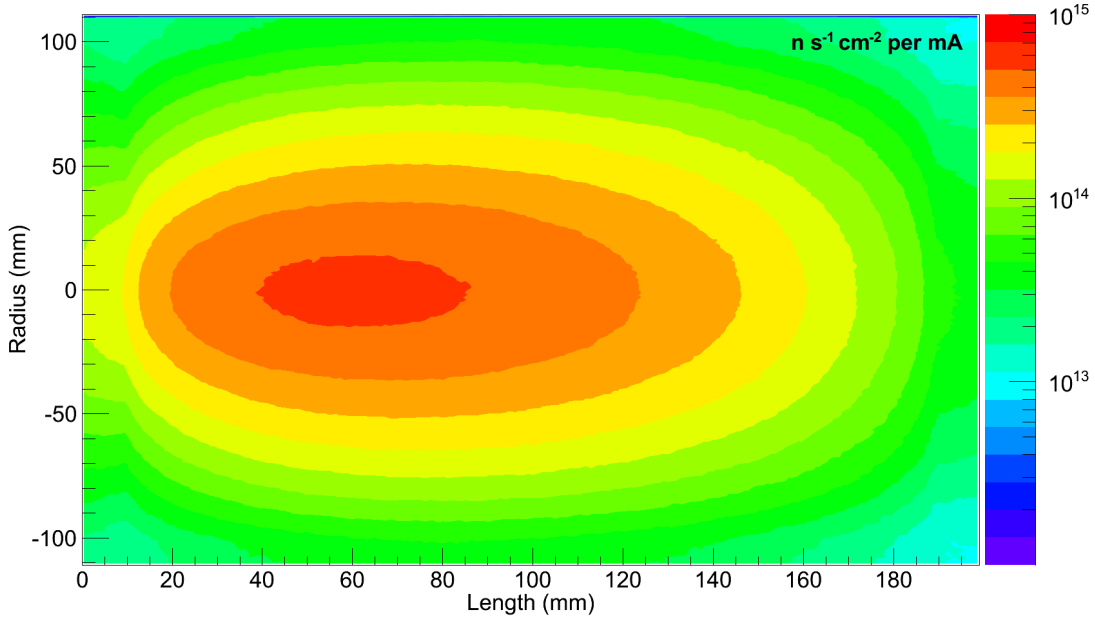

Figure 6.2: Neutron flux in monolith tungsten target

6.1.2 Segmented Targets

Two different configurations of the segmented target are studied. Firstly, the monolith discussed in the previous section is segmented into 18 equally thick plates, each plate separated by a "flux-trap" of 5 cm (segmented target). Secondly, the target optimized for the AGATE concept (optimized target), which is discussed in subsection 5.2.2.

Segmented Target

The simulation results, i.e., power density distribution and neutron flux profile, are illustrated in figures 6.3 and 6.4 respectively. The beam power deposited in the target is about 0.32 MW per mA, a considerable decrease when compared to the monolith case. Also, there is a slight decrease in the neutron intensity to about 5.23×10^{16} n/s per mA. However, the neutron flux is still concentrated within the initial length of the target. One of the target requirements necessitated by ADS transmutation is the ability to deliver a homogenized neutron field. To achieve this, the thickness of each segment needs to be adjusted, such that the neutron density leaking along the length of the target is homogenized.

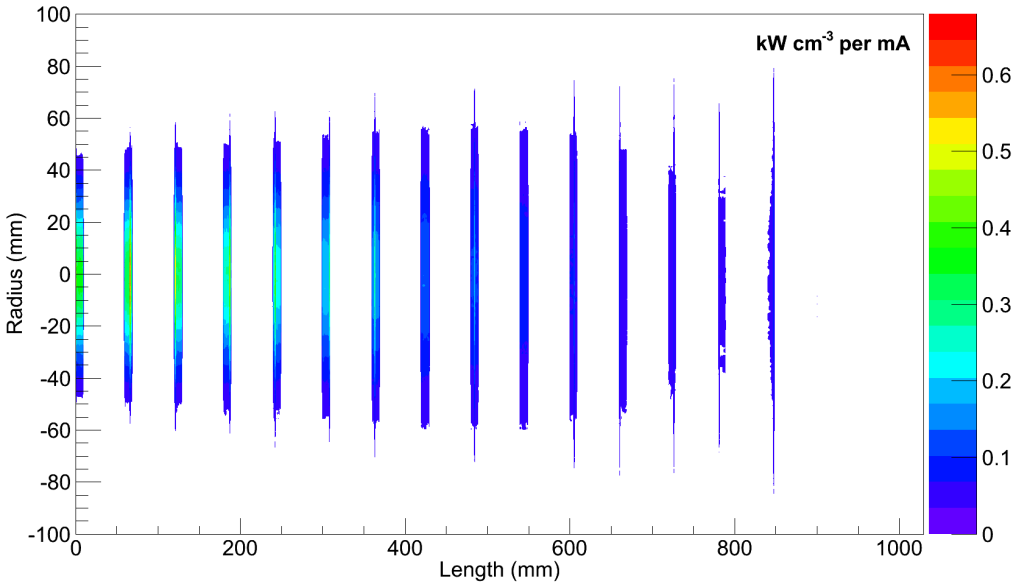

Figure 6.3: Power density in segmented tungsten target

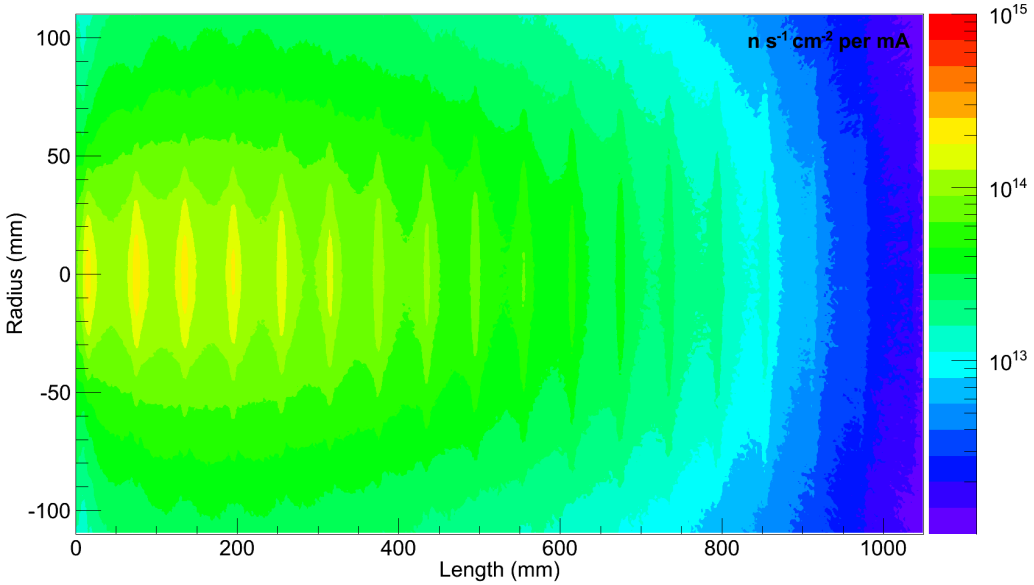

Figure 6.4: Neutron flux in segmented tungsten target

Optimized Target

Figure 6.5 shows the power density distribution in the optimized target. The maximum power density is about 0.69 kW/cm^3 per mA, occurring within the first centimeter of the solid target length. Though there is a slight decrease in power density when compared to other predecessor models, this value is still high, especially at higher currents. As discussed in subsection 5.3.3, a further configuration of the target segments is necessary to achieve reasonable heat removal through gas cooling.

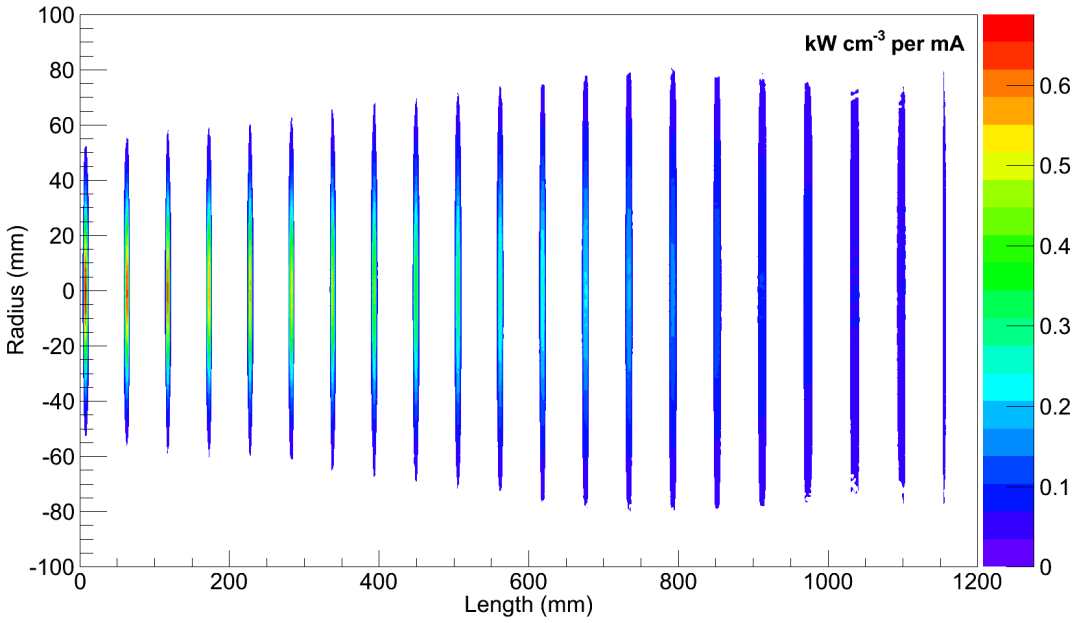

Figure 6.5: Power density in optimized tungsten target

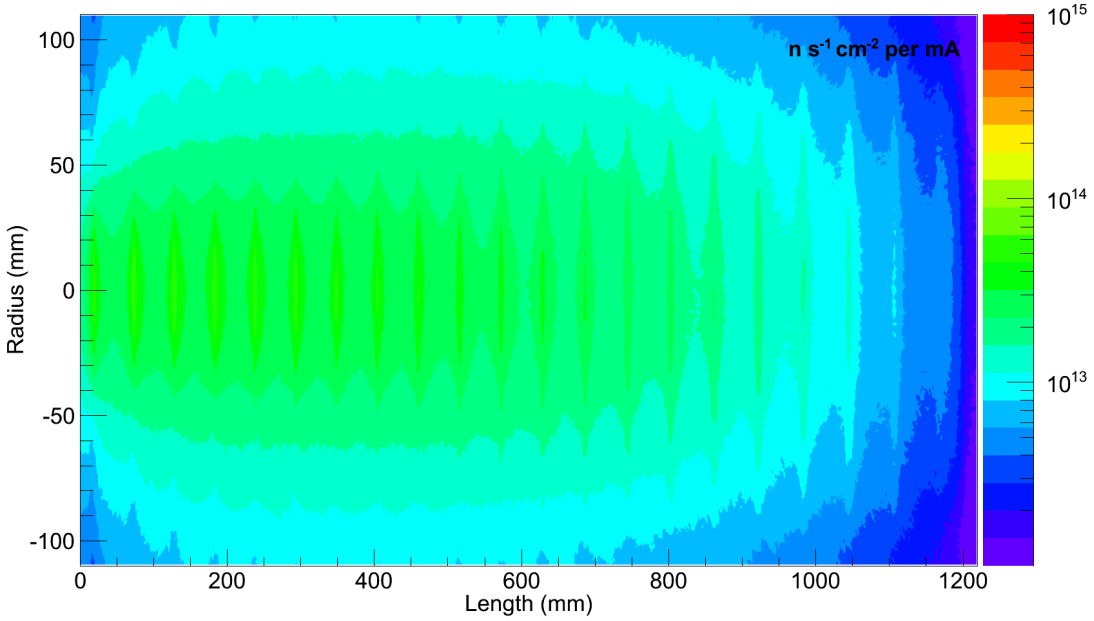

Figure 6.6: Neutron flux in optimized tungsten target

The beam power deposited in the target is about 0.35 MW per mA, more than 20 % decrease when compared to solid target. This means that the 20 % beam power is carried

away by the additionally leaking particles due to the intoduction of flux-traps, most of which are neutrons. Hence a higher neutron yield can be expected from this optimized target. In fact, from table 6.1, it can be seen that lateral neutron yield for this target is greater by about 15 %, in comparison with the monolith.

Figure 6.6 shows the neutron flux profile. Values of neutron flux are comparatively lower than the monolith. This is because of the reduction in neutron density attributed to the elongation of target length. Neutrons leaking from the target in the forward and backward directions w.r.t. beam are negligible when compared to the lateral neutron leakage. The lateral neutron intensity is about 4.72×10^{16} n/s per mA. Contours in the figure indicate that the neutron flux is better homogenized along the length of the target, a feature expected by the accelerator-driven transmutation system.

6.1.3 Comparison of Target Performance

Table 6.1 compares the performance of the targets w.r.t. different parameters. The first part of the table highlights the power density and neutron intensity of the targets. The maximum power density and the beam power deposited in the target are in decreasing order accordingly for monolithic, segmented and optimized targets. Though the total neutron intensity decreases in this sequence, the lateral neutron intensity is increasing. This is because of more neutron leakage from the front and back surfaces in the monolithic case, while more neutron leakage from the lateral surface in the other two cases. Given that the lateral neutron leakage is more suitable of applications, the optimized target is advantageous than its predecessor targets, in terms of power density and neutron intensity performance.

Gamma production in the optimized target is reduced by about a factor of four when compared to the monolith. About two spallation products are created per neutron produced in the monolith. Spallation products, which currently find no applications, contributes to the nuclide inventory and adds radiation damage in the target. In this regard, the situation in the optimized target is promising, as there is less than one spallation product created per neutron produced. Hence, nuclide inventory and radiation damage can be expected to be reduced by a factor of two.

Only about 30% of the neutrons produced leak from the monolith, while its about 70% in the optimized target. Flux-traps facilitate neutron leakage. Energy spectrum of laterally leaking neutrons is shown in figure 6.7, mean neutron energy within the brackets. As it can be seen, the mean neutron enegy increases from 0.55 MeV to 2.24 by implementing the optimized target instead of the monolith. The optimized target is characterized by lower neutron inelastic reaction probability (see table 6.1), because of leaking high energy neutrons, thereby increasing the mean neutron energy. Leakage of high energy neutrons is also an advantage in the optimized target because of further reduction in activation and damage problems. From the neutron energy spectrum, it can be seen that the energy of neutrons range from few tens of keV up to few hundreds of MeV. In general, the three different curves are comprised of two parts, a gaussian part followed by an exponential high energy tail. The former is attributed to isotropically emitted evaporation neutrons abiding the statistical model, while the latter is due to cascade reactions leading to build up of high energy neutrons in the forward direction.

Forward and backward (w.r.t. beam) leakage of neutrons is negligible in comparison to lateral leakage for the optimized target. This helps to minimize radiation damage to the structures in the forward direction. Backward leaked neutrons may diffuse into

Table 6.1: Performance comparison of the different target configurations

	Target Configuration		
	monolith	**segmented**	**optimized**
Maximum power density (kW/cm^3 per mA)	0.79	0.73	0.69
Beam power deposited (MW per mA)	0.46	0.35	0.32
Total neutron intensity (n/s per mA)	6.73×10^{16}	5.23×10^{16}	4.72×10^{16}
Lateral neutron intensity (n/s per mA)	3.75×10^{16}	4.68×10^{16}	4.39×10^{16}
Species produced (per proton)			
Neutrons	32.68	12.14	10.04
Gammas	80.07	27.13	19.24
Spallation products	77.95	11.60	6.47
Nuclear reactions producing neutrons			
Proton inelastic (per proton)	7.32	6.72	6.34
Neutron inelastic (per proton)	25.17	5.25	3.58
Neutron leakage (per proton)			
Lateral	6.00	7.48	7.03
Forward	1.34	0.03	0.06
Backward	3.44	0.86	0.46
Total	10.77	8.37	7.54
Proton leakage (per proton)	0.01	0.18	0.24

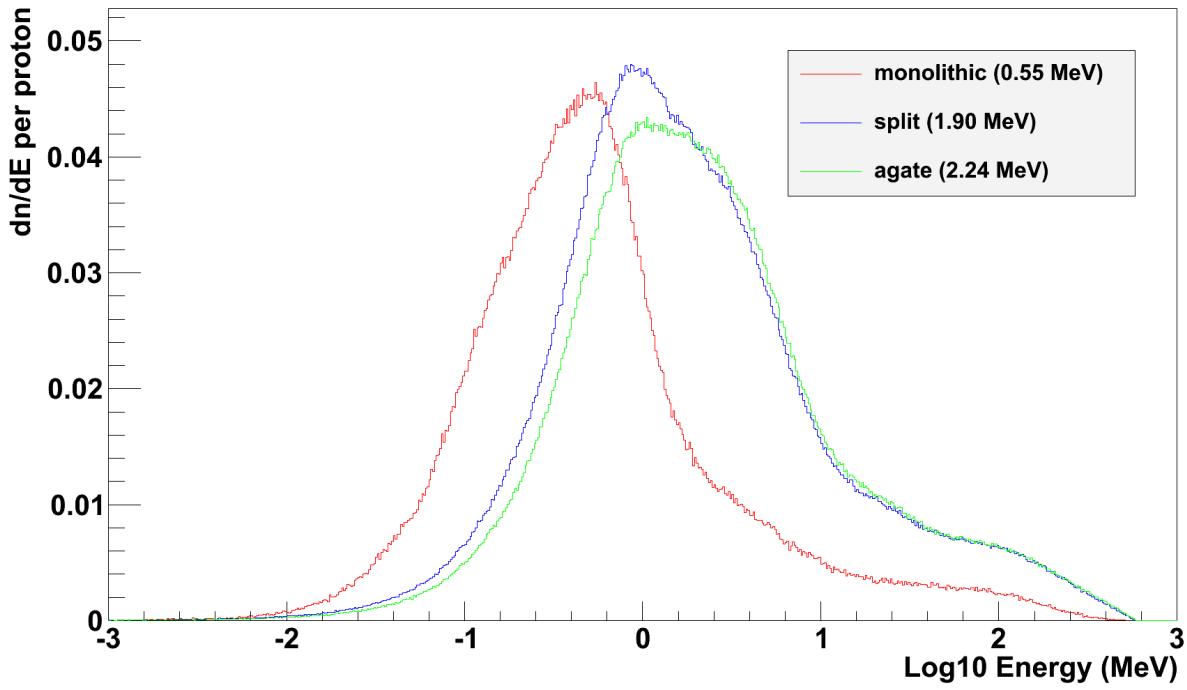

Figure 6.7: Comparison of laterally leaking neutron energy spectrum for different targets

the beam tunnel, activating structures and inducing radiation protection problem. The problem is greatly diminished here, as there is hardly any neutron delivered by the target in the backward direction. However, there are always neutrons scattered within the STM, creeping back into the beam tunnel.

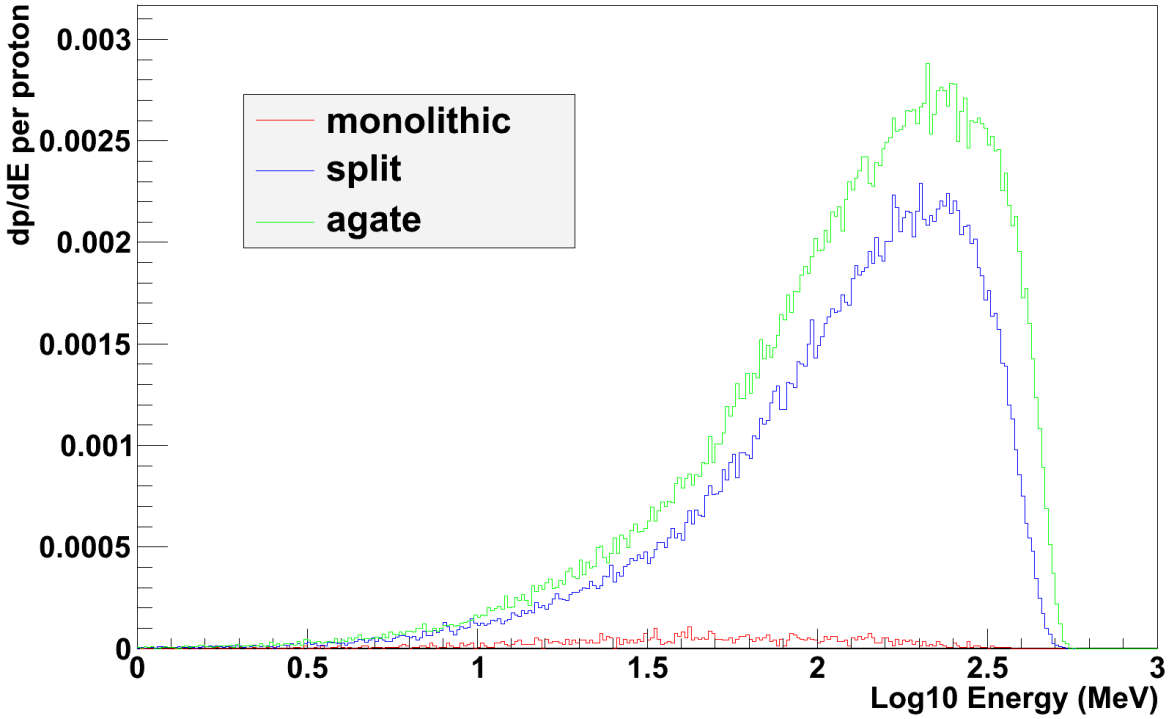

Figure 6.8: Comparison of leaking proton energy spectrum for different targets

The optimized target has evolved from the basic monolith, through the segmented concept. Inclusion of flux-traps, incorporates many significant inherent advantages to the target. However, the major drawback is the leakage of protons along with the neutrons due to flux-traps. Figure 6.8 shows the energy spectrum of protons leaking out of the target. While there are hardly any protons leaking from the monolith, it increases by about an order for the optimized target. The energy of protons range from over 1 MeV to about a few hundreds of MeV. Unlike the neutron leakage, the probability for proton leakage is very low. As it can be seen later in chapter 7, protons have higher damage capacity and leaking protons cause particle production in sites other than in the target. This can be overcome by implementing an additional dimension to the target design, i.e., making the target radially composite.

6.2 Particle Transport Simulation in the Proton Beam Window and Stop

6.2.1 Proton Beam Window

A proton beam window (PBW) is necessary to separate the vacuum region of the proton beamline and the high pressure region of the spallation target. It avoids the diffusion of gaseous and volatile nuclides, some of which are radiotoxic from the target region to the beamline region. Since the targets are irradiated outside the beamline vacuum, therefore

no breaking of the vacuum and pumping down afterwards is required when exchanging targets [Steyn et al., 1990]. Using PBW, maneuvering target exchange is simplified and hence, beam-off time is reduced.

Thin foils of low atomic number materials are preferred to keep proton beam interaction with the PBW at a minimal level. Table A.5 lists the properties of some PBW materials. Figure 6.9 plots the incident proton interaction cross section for ^{27}Al, ^{48}Ti and ^{56}Fe, the major components respectively in aluminum wrought alloy AlZnMgCu1,5, stainless steel 1.4429 and TiAl6V4 (grade5). In the incident proton energy range of some hundreds of MeV, among the three isotopes, protons have the least interaction cross section with ^{27}Al. Other advantages of aluminum alloy include high thermal conductivity, low density, excellent weldability and corrosion resistance [Meng et al., 2010]. If the temperature of the PBW can be kept low, aluminum alloy is favorable in MW spallation sources.

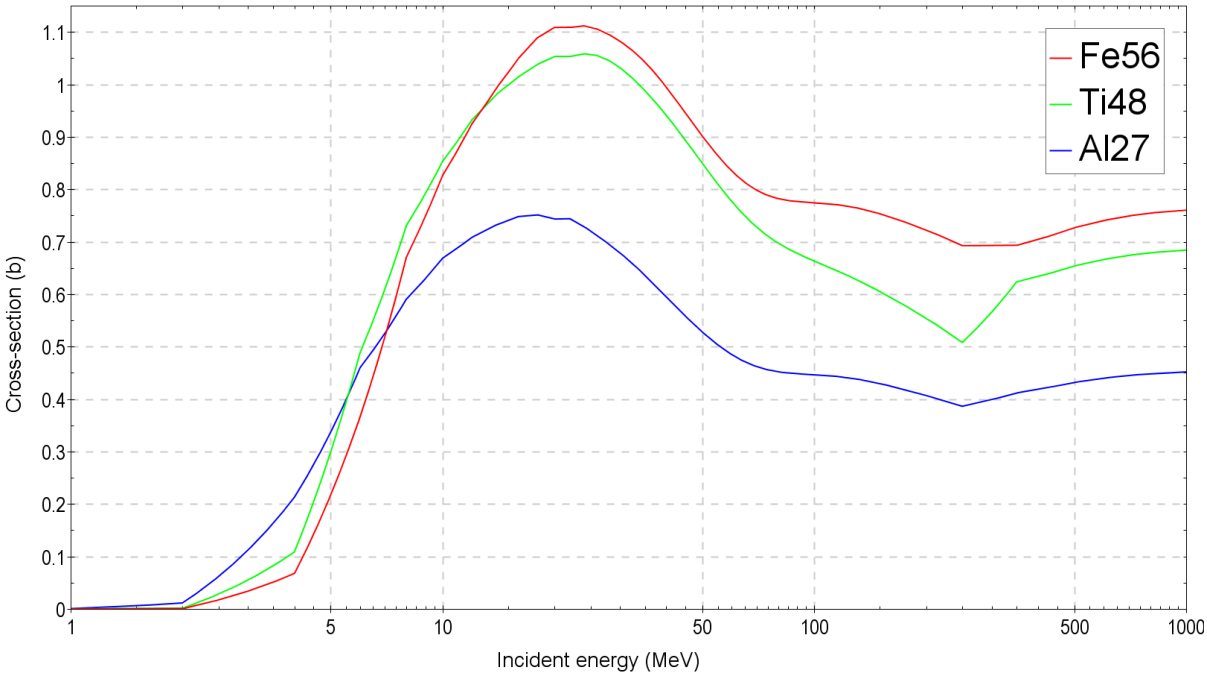

Figure 6.9: Incident proton cross section for ^{27}Al, ^{48}Ti and ^{56}Fe (JENDL/HE-2007)

Mechanical design and thermal hydraulic studies have been performed for a PBW with aluminum wrought alloy AlZnMgCu1,5 as the material [AGATE, 2010], whose elemental composition is shown in table 6.2.

Table 6.2: Composition of elements in AlZnMgCu1,5 in mass %, other than aluminum

Si	Fe	Cu	Mn	Mg	Cr	Zn	Ti
0.4	0.5	1.2-2.0	0.3	2.1-2.9	0.18-0.28	5.1-6.1	0.2

Geometry of the PBW is a spherical cap with a shape similar to a paraboloid, the curvature is oriented against the beam direction (concave). It is a double-walled design with an outer and inner shell and the gap in between is used to circulate water for heat removal. The beam window is connected to a double-walled coaxial tube. As the power

density of the proton beam is assumed to be a Gaussian distribution, the wall thickness of the inner shell of the beam window is as thin as possible in the middle and increases towards the outside. Simulations have been performed for power density in a simplified version of the PBW as shown in figure 6.10, two 3 mm thick hemispherical aluminum shells separated by 3 mm layer of water.

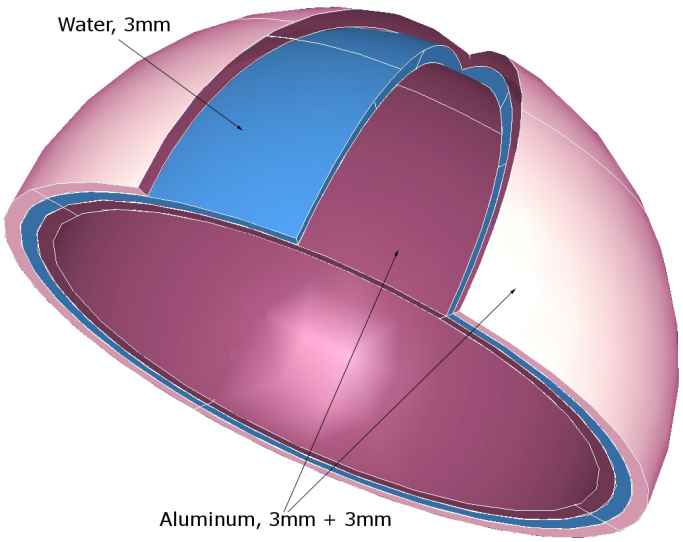

Figure 6.10: Simplified model of aluminum PBW implemented in simulation

The power density distribution for the PBW is shown in figure 6.11. A total of about 5 kW per mA is deposited in the PBW, which is about 1% of the 600 MeV proton beam power.

Heat removal from the PBW is a decisive factor to avoid significant drop in the strength parameters of the material. Temperature profile in the PBW for 25 kW power deposition, which corresponds to 5 mA proton current, is shown in figure 6.12. The heat is removed using water cooling cycle with an inlet pressure and mass flow of about 3 bar and 2 kg/s, respectively. The temperatures in both shells of the PBW remain below 100 °C.

6.2.2 Proton Beam Stop

In a linac, the beam is dumped at the linac beam stop, located at the end of the linac accelerator tunnel closer to the extraction region [Ablett et al., 2006]. The beam stop must also be able to absorb the full beam power, at least for the accident case [Efthymiopoulos, 2011]. Beam stops, like the target, see the beam directly and it is desirable to have materials which produces lesser neutrons hence lesser activation and desirable properties with respect to cooling. For nuclear analysis, a simple graphite block is used as beam stop.

As it can be seen from the figure 6.14, the neutron flux in graphite beam stop is far less when compared to the target neutron flux. Because of the low density of graphite, the stopping length for 600 MeV protons is about 80 cm (figure 6.13). This length of the beam stop necessitates a spacious arrangement of the beam stop. The maximum power density is about 0.13 kW/cm^3 per mA, which is about 5 times less than that in the tungsten target.

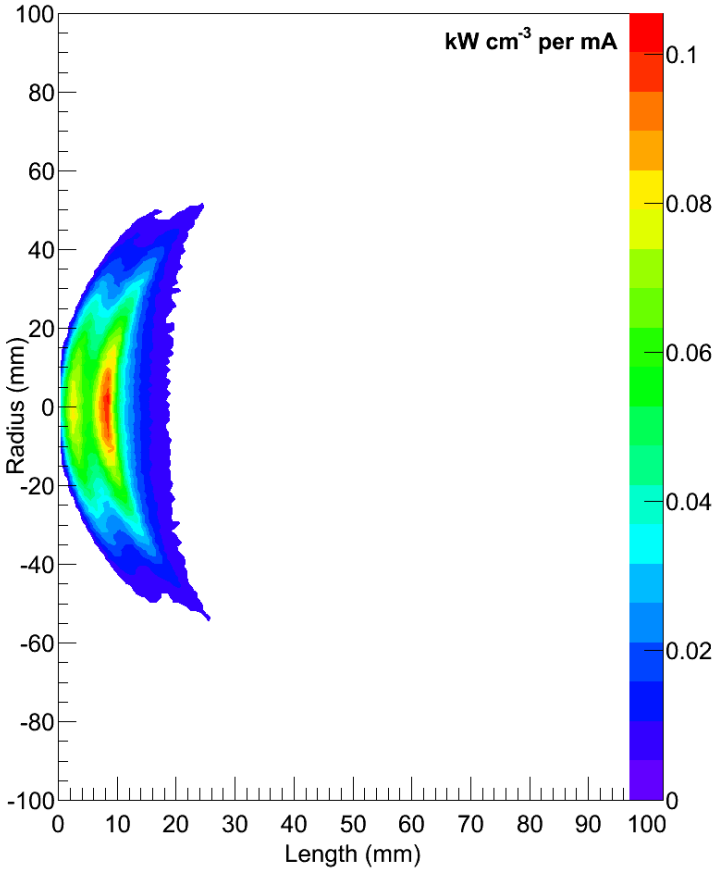

Figure 6.11: Power density in aluminum PBW

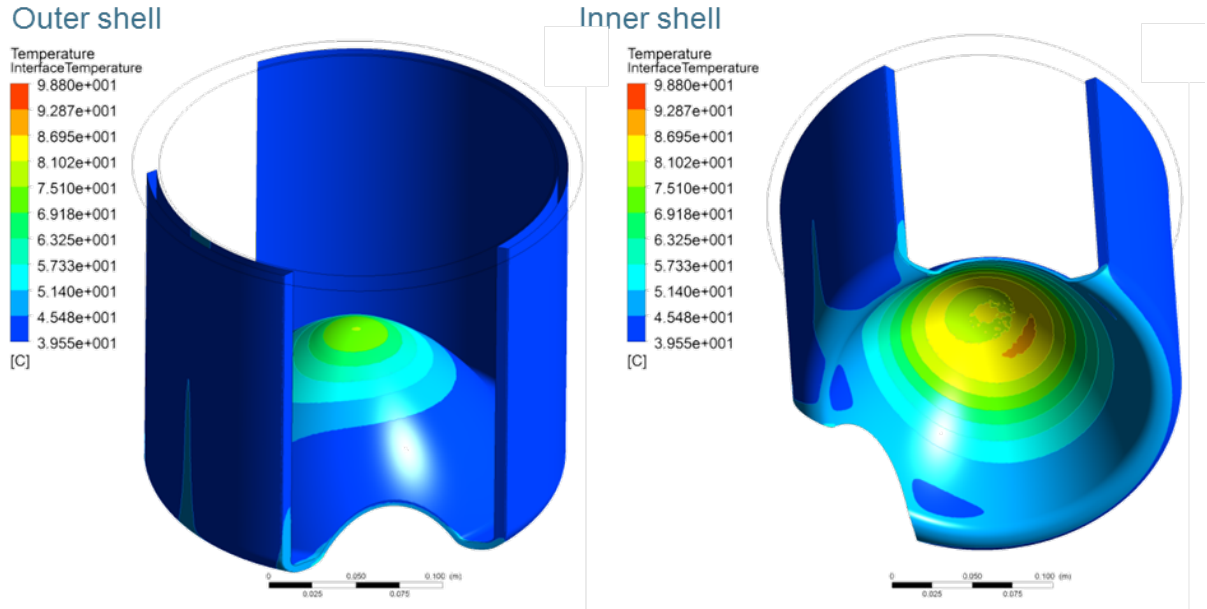

Figure 6.12: Temperature profile in aluminum PBW (outer and inner shells) [AGATE, 2011]

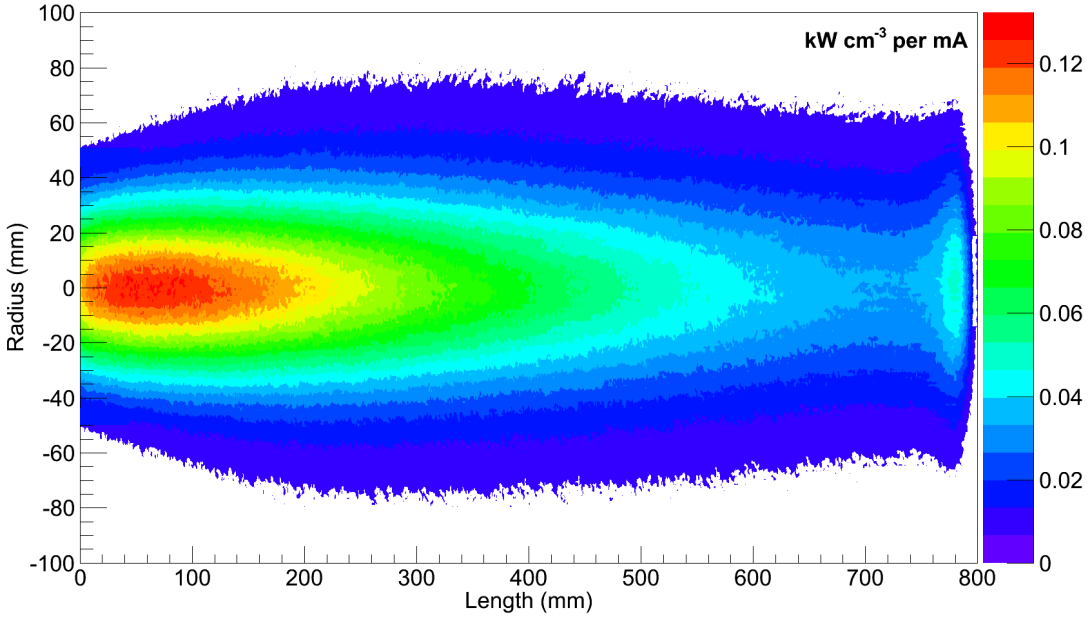

Figure 6.13: Power density in graphite beamstop

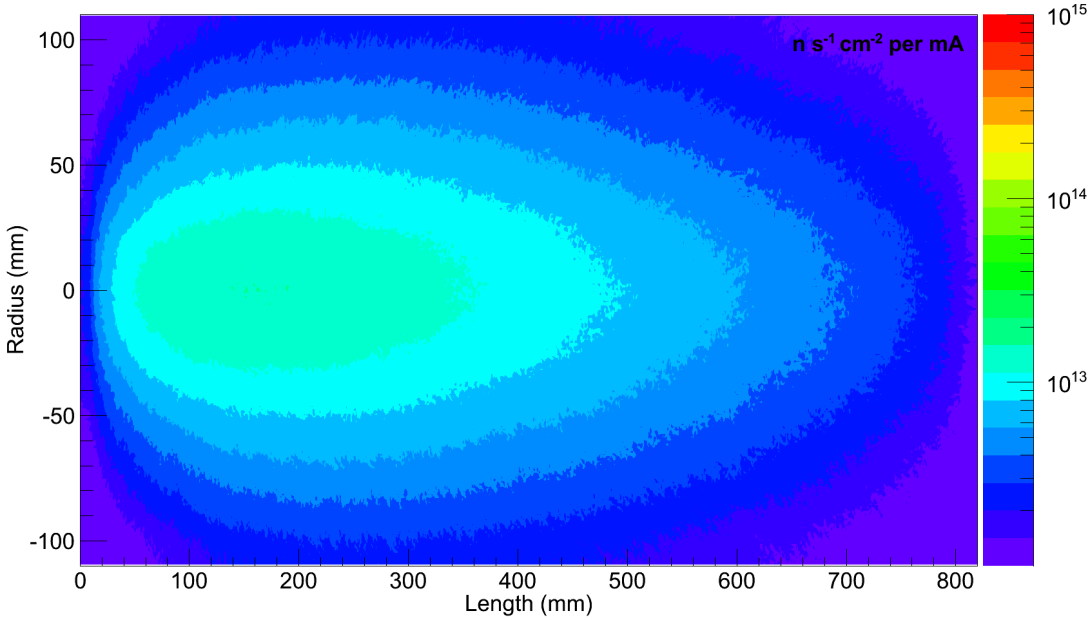

Figure 6.14: Neutron flux in graphite beamstop

CHAPTER 7

Radiation Damage Calculations

7.1 Radiation Damage Phenomenon

The general nature of radiation effects in solids is discussed in [Robinson, 1994]. A primary knock-on atom (PKA) generated in a nuclear reaction undergoes elastic collisions with the atoms of the target. Depending on the kinetic energy of the PKA, atoms are displaced from their lattice sites to make similar collisions of their own, leading to a cascade of collisions. This produces a number of atoms moving in near thermal velocities, accompanied by a small degree of electron ionization. Though many defects (interstitials and vacancies) rearrange rapidly into more stable configurations, the remaining defects agglomerate into clusters over a time that depends on the defect concentrations and target temperature. Hence, these micro structures formed cause the macroscopic effects of radiation. Radiation damage to materials is designated in terms of displacements per atom (dpa), which is a function of beam and target parameters [Efthymiopoulos, 2011]. Though dpa cannot be measured at the present time, a lot of data exist based on this concept to characterize irradiated materials.

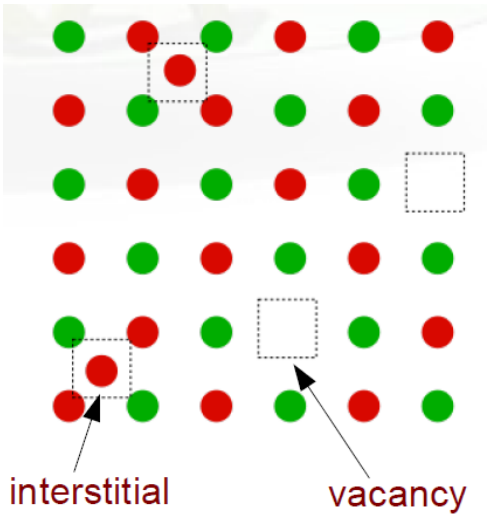

Figure 7.1: Schematic diagram illustrating the defects produced in lattice by PKAs

Other than the atomic displacements, gases like helium are produced, causing embrittlement and blistering of metallic materials [Hilscher et al., 2001]. Radiation field in a spallation target leads to much higher production of gases than in a typical nuclear

power reactor [Watanabe, 1999]. This, and high transmutation rates, makes extrapolation from reactor data very uncertain. Hence exclusive calculations are necessary to quantify radiation damage in an ADS facility

7.1.1 Radiation Damage Effects

Radiation damage effects exclusively impacting solid targets are swelling and embrittlement [Lu, 2003]. The vacancies created in the irradiated material become sufficiently mobile in the range of operating temperatures and precipitate to form voids. Such an aggregation of vacancies to form voids results in the volume change of materials and hence the swelling. On the other hand, the interstitials produced along with the vacancies induce planar defects like dislocation loops.

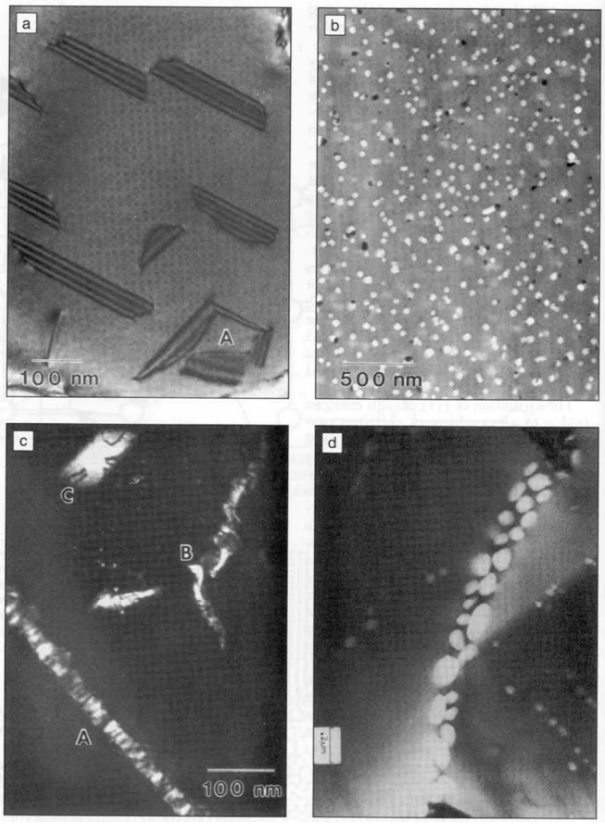

Figure 7.2: Transmission electron-microscopy micrographs of typical radiation induced defects in metals: a)Dislocation lops, b)Voids, c)Precipitates and d)Helium bubbles [Bauer, 2005]

Embrittlement occurs in the irradiated material due to helium and hydrogen, which are the major evaporation products. Helium is also a transmutation product through (n, α) and decay reactions. Aggregation of helium into gas filled voids not only fosters swelling but also results in decrease of creep and tensile ductility as these voids concentrate at the grain boundaries decreasing cohesion between the grains. On the other hand, though hydrogen is diffusive at higher temperatures, excessive hydrogen may mix with helium, or promote the formation of hydrides, the comprehensive effects of which leads to the embrittlement of the metals. Other radiation induced effects include sputtering at the target surface, chemical disorders and phase changes. Figure 7.2, shows the transmission electron-microscopy micrographs of typical radiation induced defects in metals. All these

effects degrade the structural and functional properties of the material and reduces the life time of the target. Radiation damage scales roughly with the proton current and in general, life time dose against radiation damage of most solid materials is reached after an irradiation of 10^{22} protons/cm^2 [Efthymiopoulos, 2011].

7.2 Mechanism of Atomic Displacements

Dpa can be calculated for most of the materials due to low energy neutrons (E_n <20 MeV) using the displacement cross sections available from various nuclear data libraries. For high energy neutrons and protons, this data is rather limited. A general method of estimating the displacement dose, the NRT model, has been proposed by and named after Norgett, Robinson and Torrens [Norgett et al., 1975]. According to the model, the number of Frenkel pairs N_d generated by a PKA of initial kinetic energy E is:

$$N_d = \kappa \hat{E}/2E_d \tag{7.1}$$

where κ is the displacement efficiency, given the value of 0.8, independent of the PKA energy, the target material or its temperature. E_d is the displacement threshold energy, which is listed in table A.6 for some metals. E_d for tungsten and aluminum are respectively 90 and 27 eV. $\hat{E}$ is the energy available to generate atomic displacements by elastic collisions, also called as damage energy. The damage energy is calculated using a numerical approximation to the universal function $g(\epsilon)$ [Robinson, 1994]:

$$\hat{E} = \frac{E}{[1 + kg(\epsilon)]} \tag{7.2}$$

with

$$k = \frac{32}{3\pi} \left(\frac{m_e}{M_2}\right)^{1/2} \frac{(1+A)^{3/2} {Z_1}^{2/3} {Z_2}^{1/2}}{({Z_1}^{2/3} + {Z_2}^{2/3})^{3/4}} \tag{7.3}$$

where m_e is the mass of electron. Z_i and M_i are the atomic number and mass of the atoms, i=1 for projectile and 2 for the target atom, $A = M_2/M_1$.

$$g(\epsilon) = 3.4008\epsilon^{1/6} + 0.40244\epsilon^{3/4} + \epsilon \tag{7.4}$$

where $\epsilon = E/E_L$, with

$$E_L = \frac{Z_1 Z_2 e^2}{a} \frac{1+A}{A} \tag{7.5}$$

where e is the electron charge ($e^2 = 1.4399$ eV nm)

$$a = \left(\frac{9\pi^2}{128}\right)^{1/3} \frac{a_H}{({Z_1}^{2/3} + {Z_2}^{2/3})^{1/2}} \tag{7.6}$$

where $a_H = 52.92$ pm is the Bohr radius.

The general applicability of this model is restricted by two limitations. Firstly, it is valid for a mono-atomic system, this is not a serious limitation as long as the the ratio Z_1/Z_2 does not differ too much from unity. Secondly, the energy should be less than about 25 ${Z_1}^{4/3}A_1$, which means, neutron damage calculations in light elements like beryllium in a fission spectrum or in a D-T fusion neutron spectrum would be of limited reliability.

The generic ions produced in the target and the PBW as a result of 600 MeV proton interaction, are extracted from the simulation. The part of kinetic energy of generic ions lost in elastic collisions to the atoms is calculated according to equation 7.2. Multiplying this value with the production cross section of ions gives the damage energy cross section. Summation of damage energy cross sections due to all the generic ions is implemented in equation 7.1 to obtain the final dpa values.

7.3 Radiation Damage in the Components

In a proton accelerator based transmutation system, large radiation damages are incurred in the target and the PBW [Takashita and Takahashi, 1997]. This is because of the direct interaction of these components with the incident high energy proton beam. Figure 7.3, shows the total displacement cross sections in barn for tungsten due to neutrons and protons. In the keV range, which characterizes the kinetic energy of the generic ions produced in the target due to spallation reactions (see figure 7.4), the cross section for protons is larger by an order of magnitude than that for neutrons. Hence, protons have the highest damage capacity of all the particles in an ADS. For neutrons, though the cross section of high energy neutrons is comparatively larger than the low energy neutrons, dpa due to the latter is more, owing to the higher density of evaporation neutrons.

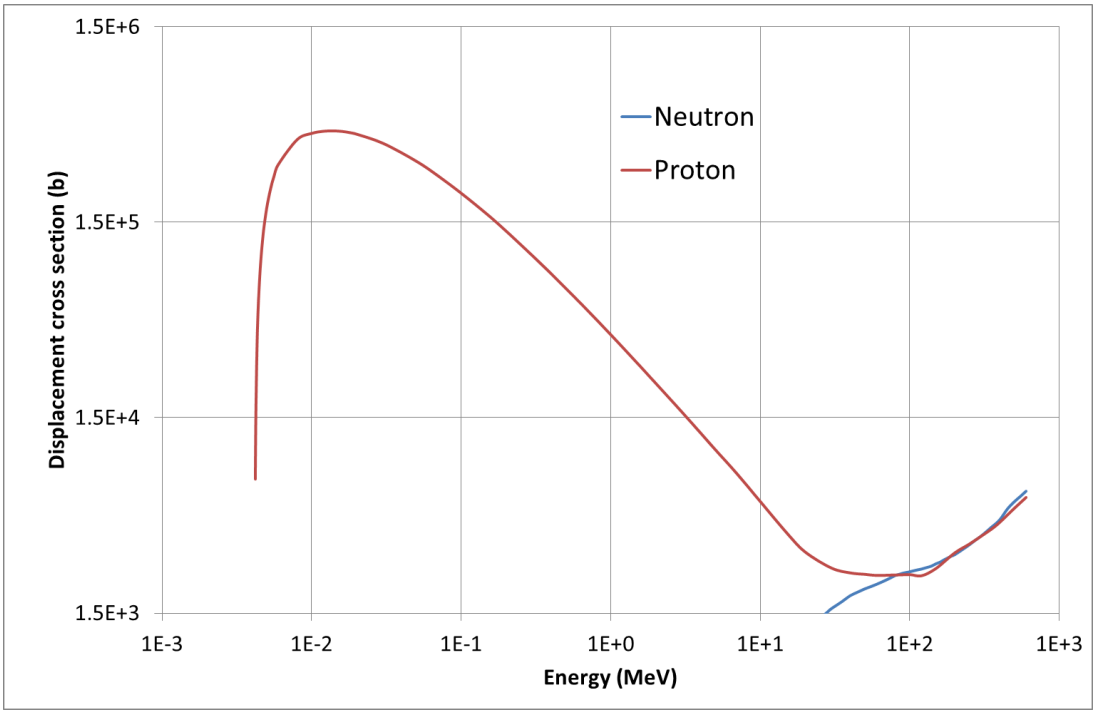

Figure 7.3: Displacement cross section for tungsten due to neutrons and protons [Broeders and Konobeyev, 2005, Broeders et al., 2005]

Simulations have been done assuming standard temperature conditions. Radiation

damage is a function of temperature. But as reported in [Bacon et al., 1997], the effect on Frenkel pairs of increasing temperatures is small but statistical significant. For example, the number of defects produced decreases by about 20-30 % as the temperature increases from 100 K to 900 K in iron. Hence, the radiation damage at eleveted temperatures, such as in irradiation conditions is smaller than that at room temperatures.

7.3.1 Radiation Damage in the Target

Figure 7.4, illustrates the kinetic energy of generic ions produced in the AGATE target. It can be seen that most of the generic ions have kinetic energy in the range of some keV, leveraging the radiation damage due to protons.

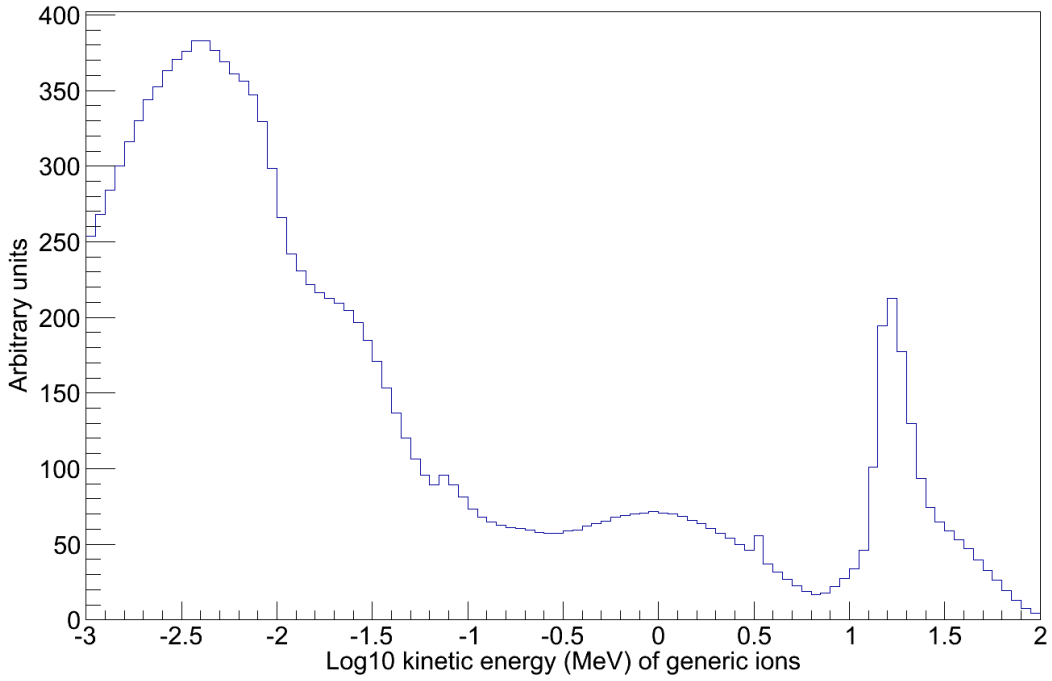

Figure 7.4: Kinetic energy of generic ions produced in the tungsten target

Table 7.1, shows the dpa and gas production in terms of appm in the AGATE target segments for one full power year (FPY) operation per mA. The radiation damage is significant in the first few segments, decreasing gradually with increasing tungsten length. This is plausible as the protons with the highest damage capacity gets stopped-out with increasing target length. Similar analogy can be applied for the helium production behavior in the segments, as the number of interaction with the material decreases with increasing target length.

A working group at Los Alamos National Laboratory in the USA headed by W.F. Sommer has looked at the configuration and cooling of tungsten targets in detail [AGATE, 2011]. Irradiations with 800 MeV at 1 mA protons over six months caused 23 dpa and produced around 11,000 appm hydrogen and 2020 appm helium. Despite this stress, when irradiation ended very few material defects were detected in the tungsten. The dpa values for the target are in line with the above observation, when compared with half FPY dpa values.

Comparing helium production to dpa (He/dpa) can result in new damage phenomena of mechanical properties [Hilscher et al., 2001]. The maximum He/dpa is in the first

Table 7.1: Radiation damage and helium production in the target segments

Target Segments (beam downstream)	**Radiation Damage** dpa/FPY per mA	**Helium Production** (appm/FPY per mA)	**He/dpa** appm He per dpa
1	4.46	827.97	185.85
2	4.49	631.04	140.39
3	4.33	600.18	138.51
4	4.19	575.35	137.27
5	4.01	546.91	136.32
6	3.81	515.45	135.14
7	3.55	484.49	136.31
8	3.37	452.92	134.44
9	3.17	425.17	134.33
10	2.89	384.22	132.82
11	2.66	355.40	133.55
12	2.45	321.71	131.53
13	2.16	282.17	130.50
14	1.89	245.24	129.63
15	1.62	207.28	127.77
16	1.35	172.04	126.97
17	1.09	132.61	121.81
18	0.83	96.86	116.47
19	0.58	60.07	103.31
20	0.32	23.76	74.46
21	0.06	2.91	49.10
Total	**53.30**	**7343.75**	**137.78**

segment of the target corresponding to about 185 He/dpa. This is about 25 % lower than what is predicted by other calculation [Green et al., 1988] for 600 MeV protons on tungsten. The lower value of helium production is probably due to the escape of high energy neutron, which otherwise would have caused the production of these gases through different reaction channels.

Certain changes in the mechanical properties of irradiated tungsten have been measured and studied [Maloy et al., 2005]. Such as high yield stress which decreases with increasing irradiation temperature and low ductility in tension. Figure 7.5 shows the compression stress/strain curves for different samples of irradiated tungsten under different irradiation temperatures. According to the study, pure tungsten is brittle after exposure to a proton fluence of 3.7×10^{20} p/cm^2, though some ability to deform is preserved and an increase in the yield stress is observed in samples irradiated over a dose of about 4 dpa.

The life time dose in the solid target is reached after a proton irradiation fluence of 10^{22} p/cm^2. Comparing this limit to the irradiation conditions in AGATE facility, yields a life time of about 1.5 years for the target, per mA and full power operation.

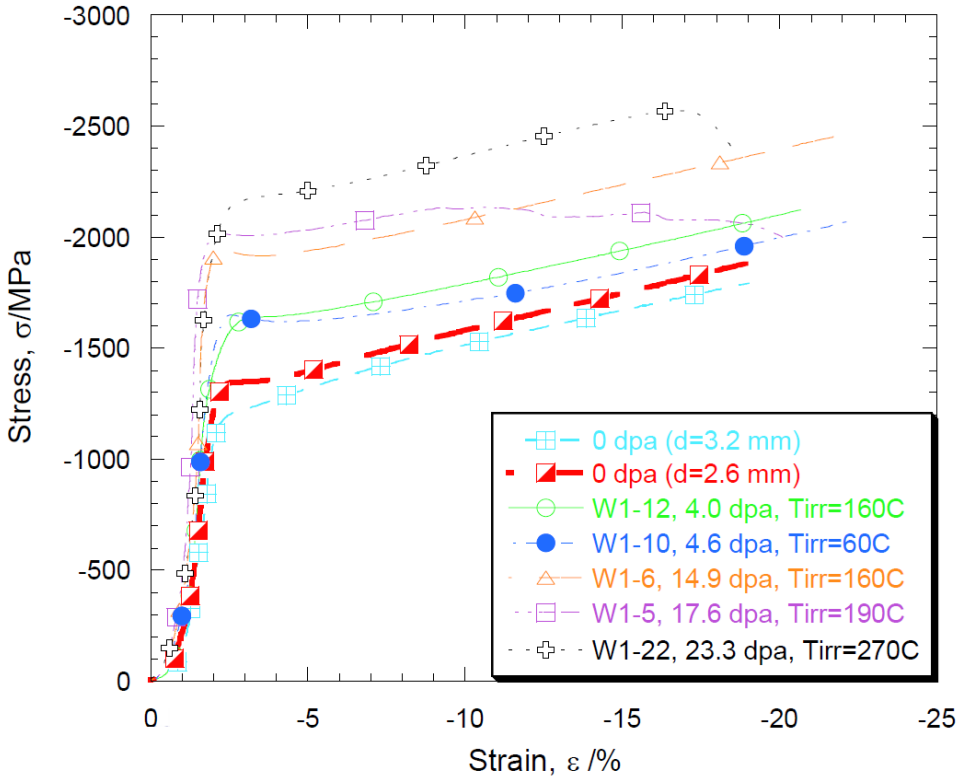

Figure 7.5: Comparison of compression stress/strain results for irradiated tungsten [Maloy et al., 2007]

7.3.2 Radiation Damage in the PBW

Table 7.2, shows the radiation damage parameters in the layers of the PBW. Since the dimensions of the PBW is very small compared to the target, the influence of the proton beam on the same is also greatly reduced. The He/dpa ratio (appm He per dpa) value is about 14 % lower than what was measured [Green et al., 1988] in aluminum for 600 MeV protons. The inner layer receives the same proton flux as the outer one but more neutron flux due to the closer proximity to the source of spallation neutrons. Hence, there is slightly more radiation damage (displacement and helium) productions in the inner layer than in the outer layer.

Table 7.2: Radiation damage and helium production in the PBW surfaces

PBW Layers (beam downstream)	**Radiation Damage** dpa/FPY per mA	**Helium Production** (appm/FPY per mA)	**He/dpa** appm He per dpa
Outer	0.37	67.92	183.28
Inner	0.44	81.41	185.13
Total	**0.81**	**149.33**	**184.28**

The life time of PBW is given roughly as 5 dpa/y [MLF, 2012, Dai et al., 2006]. According to this, assuming an operation at 5 mA proton current, the proton beam window composite has a life-time of about a year. However, dpa alone is inadequate to estimate the life time of the the components and must be accompanied by additional investigation on mechanical properties (such as tensile, fatigue and bending tests) after irradiation.

CHAPTER 8

Radiological Safety Aspects

The optimized AGATE target is encapsulated in a target container. The container is circulated with helium gas for cooling the target at a pressure of about 60 bars. PBW is flanged on to the beam entrance part of the container. Figure 8.1, describes the complete layout of the spallation target module.

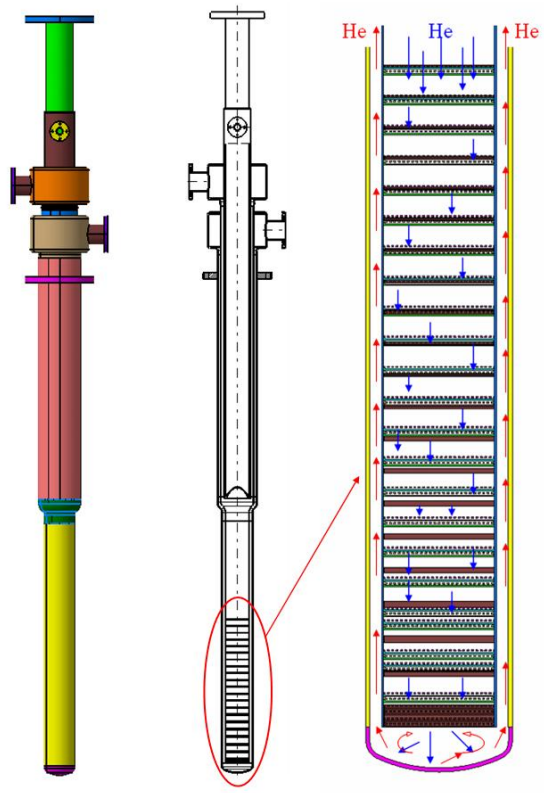

Figure 8.1: The spallation target module along with the circulation of He coolant [AGATE, 2011]

The coupling of STM with other reactor structures, such as the sub-critical core and the reflector is performed in a separate study[Biss, 2012]. Radionuclide inventory calculations are restricted to the STM alone, i.e. the feed back effect from the sub-critical core is not included. For radiation shielding, the effect of the core has also been analysed. The

proton beam energy is 600 MeV. All the results are normalized to 1 mA 600 MeV proton current or per proton.

8.1 Calculation of Radionuclide Inventory

The variety of nuclear interactions that occur in a spallation facility induces activity in the components as the stable nuclides are transmuted into radioactive nuclides. The spallation process leaves behind residues which are, sometimes far related to the target component material, some of which may be volatile too. Literally, the activity "flows" to remote regions and is not restricted to the region of origin. This activity is the source of dose for the control equipments or working personnel in the facility. Hence it is very important to know the different nuclides and also quantitatively, that can be present in the different components of an ADS facility to take suitable measures against them and stay within the legal limits of dose exposure.

Gollon [Gollon, 1976] discusses some rules of thumb which could be used for the calculations related to radioactivation in particle accelerators. They are:

- The dose rate $\dot{D}$ (R/hr) at a distance r (meters) from a "point source" of gamma rays with source strength S (Curies) and the photon energy E_γ (MeV) is:

$$\dot{D} = \frac{E_\gamma}{2.2}\frac{S}{r^2} \tag{8.1}$$

- About 50% of the nuclear interactions produce a radionuclide with half-life greater than a few minutes and out of these, about half of them have a half-life greater than a day.

- The dose rate in shielding materials due to a constant irradiation is:

$$\dot{D} = b\,\phi\,log(\frac{t_i + t_c}{t_c}) \tag{8.2}$$

  where, ϕ is the incident flux, b is a material and geometry dependent constant determined using *Rule 2* or experimentally. And t_i and t_c are the irradiation and cooling times. This is valid for materials which yield many radionuclides upon irradiation, and for $t_c > 12min$, $(t_i + tc) < 500$ days.

- In a cascade, a proton produces four stars for each GeV of kinetic energy.

Radioactive Decay Module (RDM) in Geant4 is used to simulate the nuclear decay ($\alpha, \beta^{\pm}$, EC) of unstable residual nuclei [Geant4, 2010]. It uses the Evaluated Nuclear Structure Data File (ENSDF) for information on nuclear half-lives, nuclear level structure for the parent or daughter nuclide, decay branching ratios, and the energy of the decay process. RDM also includes the treatment for de-excitation of of an excited isomer.

8.1.1 Radionuclide Inventory in the Target

As the spallation products are formed, they and the target nuclei are continuously irradiated by the secondary particles produced in situ. Figure 8.2 shows the decay of nuclide inventory in the target after one FPY operation. Tritium inventory is excluded because

of its comparatively smaller radiotoxicity due to soft beta decay and short biological life time [ESS, 2002]. The total specific activity, contributed by several nuclides, at the time of shutdown is about 2.4×10^{14} MBq/g per mA. The pie-chart in the inset of the figure shows the nuclides contributing most of the activity at shutdown, namely ^{172}Hf, ^{173}Lu, ^{174}Lu and ^{179}Ta. It takes 1000 years for the activity to reach about 6.2 MBq/g per mA. Unlike the actinides, which need to be transmuted, radionuclides produced in the target have lesser radiotoxicity and shorter life time.

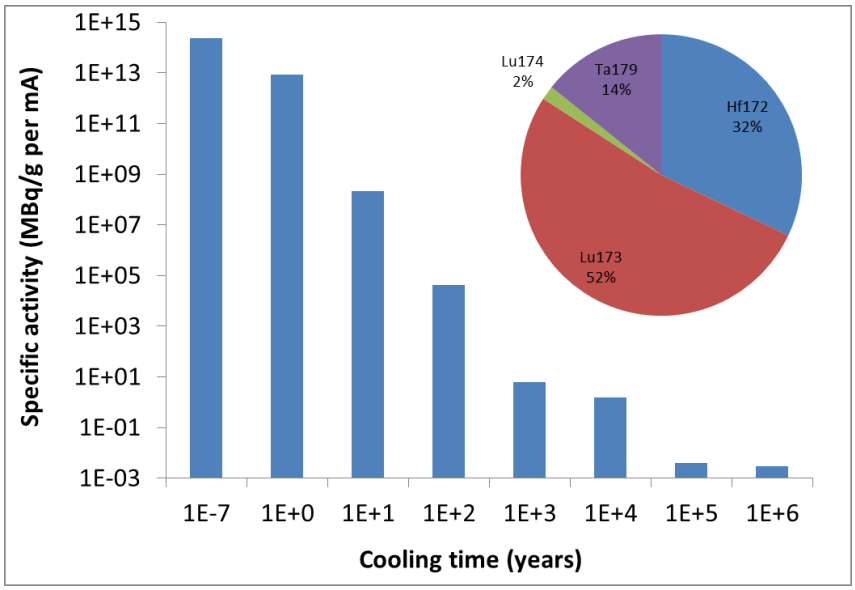

Figure 8.2: Decay of nuclide inventory in the target after one FPY operation

According to Sullivan [Sullivan, 1992], induced specific activity (S, Bq/g) in heavy element target such as lead, rhenium, tungsten, etc., after irradiation in a beam of Φ protons per cm^2 per second is:

$$S = 1.8 \times 10^{-3}\Phi[t^{-0.4} - (T+t)^{-0.4}] \tag{8.3}$$

where T and t are irradiation and cooling times respectively in days.

According to equation 8.3, the total specific activity induced in the tungsten target at the time of shutdown, for an irradiation time of one year at a proton flux of 2.2×10^{14} per cm^2 per second (corresponding to 1 mA of peak current), is about 7.5×10^{14} Mq/g per mA. This value is more by a factor of about 3, when compared to the simulated values.

Most of the activity in the target is contributed by a small number of nuclides. Nuclides whose half-lives are shorter than one year, and in present in the target in amounts of more than one MBq are listed in table 8.1.

The nuclide ^{148}Gd is of major concern as it is an alpha-particle emitter with a 75-year half-life and contributes significant amount of dose in case of inhalation [Trellue, 2003]. Measured production cross section of this isotope is about 8.3 mb due to 600 MeV protons on tungsten [Kelley et al., 2005]. The calculated cross section in the target is about 2.4 mb, which is lower by the measured value by a factor of 3 to 4. The difference in values is probably due to the segmented nature of the target, other than the uncertainties. Other significant alpha emitters are ^{146}Sm and ^{154}Dy. These isotopes are relatively in lower concentrations and have very long half-lives of over millions of years. Isotopes contributing large amounts of specific activity in the target are ^{172}Hf, ^{173}Lu, ^{174}Lu and

Table 8.1: Nuclides with half-life shorter than one year, and present in the target at shutdown in amounts of more than one MBq after one FPY operation

Isotope	**Half-life (y)**	**MBq/g per mA**
Be10	1.51E+06	1.13E-04
C14	5.73E+03	1.98E-02
Ar39	2.69E+02	1.05E-01
Fe60	1.50E+06	1.89E-05
Co60	5.28E+00	1.52E+01
Ni63	1.00E+02	5.84E-01
Se79	1.13E+06	1.52E-04
Kr81	2.29E+05	5.84E-04
Kr85	1.08E+01	1.10E-01
Sr90	2.88E+01	9.74E-01
Nb91	6.80E+02	1.25E-01
Zr93	1.53E+06	1.66E-04
Mo93	4.00E+03	1.42E-02
Nb94	2.03E+04	2.79E-03
Tc97	2.60E+06	4.34E-05
Tc99	2.11E+05	4.26E-04
Rh101	3.30E+00	7.83E+00
Pd107	6.50E+06	1.31E-05
La137	6.00E+04	9.44E-04
Pm145	1.77E+01	1.47E+01
Pm146	5.53E+00	1.45E+01
Sm146	1.03E+08	1.13E-05
Gd148	7.46E+01	1.11E+01
Eu150	3.69E+01	3.05E+00
Gd150	1.79E+06	1.15E-03
Sm151	9.01E+01	3.14E-01
Eu154	8.60E+00	3.18E+00
Dy154	3.00E+06	1.55E-03
Tb157	7.11E+01	1.58E+02
Tb158	1.80E+02	9.43E-01
Ho163	4.57E+03	7.01E+00
Tm171	1.92E+00	6.37E+01
Hf172	1.87E+00	2.33E+04
Lu173	1.37E+00	3.78E+04
Lu174	3.31E+00	1.18E+03
Ta179	1.82E+00	1.04E+04
Hf182	9.01E+06	1.64E-04
$Nb93^{m1}$	1.61E+01	2.42E-04

^{179}Ta, all emitting positrons, until stable daughter isotopes are formed. The hard gamma emitter, ^{60}Co is also present in the target.

The decay heat due to residual nuclides is low and no relevant target heat-up by decay heat is expected [ESS, 2002].

8.1.2 Radioactivity in the PBW

The PBW has two layers of aluminum, with water cooling in between. Commonly identified radionuclides under irradiated conditions in water are ^{7}Be and ^{11}C, and additionally in aluminum are ^{18}F, ^{22}Na and ^{24}Na [Mauro, 2009].

Table 8.2: Radionuclides present in the aluminum PBW at shutdown after one FPY operation

Isotope	**Half-life (y)**	**MBq/g per mA**
Be7	1.46E-01	4.40E+03
C11	3.88E-05	2.75E+03
N13	1.90E-05	1.06E+04
C14	5.73E+03	7.59E-01
O15	3.87E-06	1.14E+04
F17	2.04E-06	6.02E+01
F18	2.09E-04	7.49E+04
O19	8.53E-07	3.38E-10
Ne19	5.46E-07	1.43E-04
F20	3.49E-07	3.77E-05
Na21	7.13E-07	8.35E+02
Na22	2.60E+00	3.15E+04
Ne23	1.18E-06	2.96E+02
Mg23	3.59E-07	1.81E+05
Ne24	6.43E-06	2.77E+03
Na24	1.71E-03	7.75E+04
Na25	1.87E-06	6.15E+03
Al25	2.28E-07	2.26E-04
Al26	7.40E+05	3.03E-01
Mg27	1.80E-05	8.60E+03
$Na24^{m1}$	6.41E-10	2.56E+07
Total		**2.60E+07**

Table 8.2 highlights the radionuclides that are present in both the inner and outer layers of the aluminum PBW at shutdown. The isotope ^{26}Al, is one of the primordial isotopes and is also produced during the high energy cosmic ray interactions in the air. It has a very long half-life of over 700,000 years and emitting gammas of 1.809 MeV energy after a positron emission. ^{22}Na is also a hard gamma emitter, but with comparatively shorter half-life. Both of these isotopes may pose problems with radiation protection during the maintenance as the PBW needs to be replaced quite frequently than most of the other structures.

Water, which is used to cool the PBW is also under severe irradiation. As it circulates in the coolant loop, it can carry the radioactivity to heat exchangers and pumps and induce

dose to the working personnel in the cooling section. Hence in this case, in addition to the long-lived nuclides, it is necessary to look into the short-lived nuclides as well. In table 8.3, all the short-lived nuclides that are present in the irradiated water at shut down have been shown. All of the listed isotopes are produced as a result of spallation reaction on oxygen. Except ^{7}Be, ^{10}Be and ^{14}C, none of the nuclides have a half-life of more than an hour and hence decay very quickly. Interestingly, most of these short-lived isotopes are positron emitters. Electrons generated in electromagnetic cascade, leads to the production of bremsstrahlung, which interacts with the oxygen nuclei in giant resonance reactions [Sullivan, 1992]. These interactions mainly produce ^{15}O in cooling water, with 2.1 minutes of half-life.

Table 8.3: Radionuclides present in the cooling water of PBW at shutdown after one FPY operation

Isotope	**Half-life (y)**	**MBq/g per mA**
Be7	1.46E-01	3.07E+04
Be10	1.51E+06	2.25E-03
C10	6.10E-07	2.42E-01
C11	3.88E-05	3.29E+04
N13	1.90E-05	1.37E+04
C14	5.73E+03	2.18E+00
O14	2.24E-06	4.80E-04
O15	3.87E-06	1.59E+05
N16	2.26E-07	5.34E-04
Total		**2.37E+05**

8.1.3 Radioactivity in the Beam Stop

Graphite is used as beam stop material because of its low activation properties. There are only two long lived nuclides ^{10}Be and ^{14}C present in the beam stop at shutdown (table 8.4). In the simulation, the beam stop has been continuously irradiated for a year, which is not true in reality. The beam stop sees the proton beam only for a very small fraction of time during operation, as its function is to absorb the beam only when the beam fails to be deflected into its path or during the beam maintenance. In terms of activation, graphite is a very suitable material for the beam stop.

Table 8.4: Radionuclides present in the graphite beam stop at shutdown after one FPY operation

Isotope	**Half-life (y)**	**MBq/g per mA**
Be7	1.46E-01	3.86E+05
Be10	1.51E+06	8.18E-02
C14	5.73E+03	3.47E-02
Total		**3.86E+05**

8.2 Simulation of Shielding Behavior

Energetic and intense radiations due to different particles are produced in an ADS. The shielding should be designed such a way that it attenuates these radiations that are acceptable to humans and other apparatus outside the shielding, at reasonable cost and without compromising the spallation source facility for its designed purpose. The shielding should be optimized in such a way that it is thick enough to reduce the exposure to the personnel and thin enough to facilitate the application of particles without reducing the particle flux.

By separating the radiation fields into a spallation-induced and a fission-induced part, it is shown that the neutrons with energy higher than 10 MeV, originating exclusively from the proton induced spallation reactions in the target, contribute for the entire part of the radiation fields and the effective dose at the top of the shielding [Seltborg et al., 2005]. The largest radiation doses will appear in the forward direction of the incident proton beam and the design of the biological shielding in this direction will generally be of the greatest importance.

The knowledge of dose equivalent is important for radiation protection purposes. One way to estimate the dose is to multiply the energy deposition that is ambient dose by an appropriate quality factor [Koprivnikar and Schachinger, 2002]. The probability of stochastic radiation effects depends not only on the absorbed dose, but also on the type and energy of the radiation causing the dose.This is considered by weighting the absorbed dose with a factor related to the radiation quality and is listed in table A.7.

The other generally employed method is to multiply the fluence as a function of energy by appropriate dose conversion factors. Hence, dose conversion factors are used to convert the estimated local particle fluence to dose rates. Tables A.8 and A.9 show the fluence to equivalent dose conversion factors for neutrons and photons, which can penetrate deeply through the matter because of their neutral charge.

8.2.1 Shielding Materials

In the report [Hanslik, 2006], a comprehensive study of all the materials is described. The ideal shielding materials should have the properties such as homogeneity, durability, fire resistant, low activation and manufacturing cost. Some of these properties for different materials are compared in table A.10.

Soil is one of the cost effective shielding material. The water content in the soil plays an important role in the shielding of the low energy neutrons as most of the kinetic energy is transferred to the hydrogen in an elastic collision. Other than that, soil also contains medium heavy elements that effectively shield photons. The density of soil varies between 1.7 g/cm^3 to 2.25 g/cm^3 independent of soil type and water content. In a spallation system, soil is used as the outer most layer of shield.

Concrete is the other cost effective shielding material that can be used for the shielding of neutrons and gammas. Because hydrogen plays an important role in the neutron shielding, the operation temperature limits the life of the concrete shielding. Though concrete has a good compression strength, it is less resistant to tensile strength. Hence concrete structures must be supported with steel. Some mechanical and thermal properties of different types of concrete are displayed in table A.11.

Hydrogen is an effective neutron moderator. With the high hydrogen content, water is considered as a good choice for shielding of neutrons. Insolubility of boron salt in water,

corrosion of steel structures and the thick container required to hold water are the possible technical difficulties. Paraffin has been used as shielding material in the past. Because of its flammable nature, it must be filled in fire resistant metallic containers.

The high density (7.85 kg/cm^3) and high melting point (1536 ^0C), combined with the low production cost, makes iron as an attractive shielding material. Carbon is the most important component in steel as it determines the properties of steel. Steel is a relatively good absorber of thermal neutrons and gamma radiation, good moderator of high energy neutrons through inelastic interactions. Steel has very good structural, thermal and chemical properties. Stainless steel is the preferred variant of steel because of its resistance to corrosion. On the other hand, cobalt impurities may be activated to form the long lived ^{60}Co isotope. Cast steel offers many advantages with respect to manufacturing and design of the shielding. Its recycling capabilities leads to lower production costs.

Lead is the most important shielding material against gamma radiation. Pure lead has a high density (11.3 g/cm^3) and resistant to corrosion. Its low melting point (327.4 ^{0}C), low rigidity and high acquisition cost limits the wide usage of lead as shielding material. The high chemical toxicity of lead necessitates cautiousness while handling and working. Lead is used where a small shielding thickness is required.

8.2.2 Performance of Shielding Structures

In an ADS, the prompt radiation is dominated by neutrons. Neutrons are attenuated by elastic and inelastic scattering. The attenuation length of neutrons in the shielding determines the attenuation of dose equivalent provided by the shielding. Dense materials of high atomic number effectively attenuates neutrons of all energies by inelastic scattering to the lowest energy threshold of inelastic scattering. For the range below this threshold low atomic number materials such as hydrogen, are to be used to moderate the neutrons through elastic scattering to continue shielding against neutrons.

Due to the high material density steel is harnessed to design compact shield in order to minimize the space required. An important deficiency of steel in shielding against the neutrons is that it contains no hydrogen and its lowest inelastic energy level is 600 keV, consequently leading to buildup of neutrons below this energy. Another special effect displayed by iron in interacting with neutrons is low cross section in the energy range from 0.02 to 0.8 MeV. Figure 8.3 shows the total neutron cross section for iron in this particular energy range. It is filled with a series of small resonance lines implying that the neutron attenuation probability is lower in this region. Hence it becomes necessary to follow the steel shielding from outside by some material with hydrogen content such as concrete to eliminate the intermediate energy neutrons. From radiation transport point of view it turns out that at least one high energy inelastic interaction mean free mean path thickness of hydrogenous shielding lies on the outside which corresponds to about 60 cm of concrete. One attenuation length of concrete (about 60 cm) is enough after iron to shield against low energy neutrons, while it is only necessary to shield in the lateral and the forward directions [IAEA, 1988].

Figure 8.4 shows the neutron and gamma spectrum emanating from the tungsten target. The spectrum is characterized by high energy particles. It is also worthwhile to remind here about the angular dependence of the neutrons (figure 2.10). The high energy cascade particles are forward peaked in nature, that is along the direction of the proton beam and this fact puts stringent conditions in the forward shielding than in any other

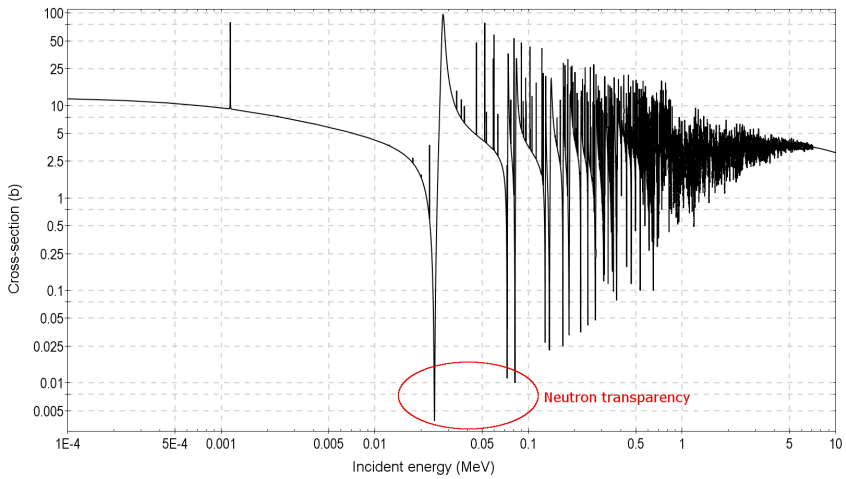

Figure 8.3: Total neutron interaction cross section for ^{56}Fe (JENDL/HE-2007)

directions.

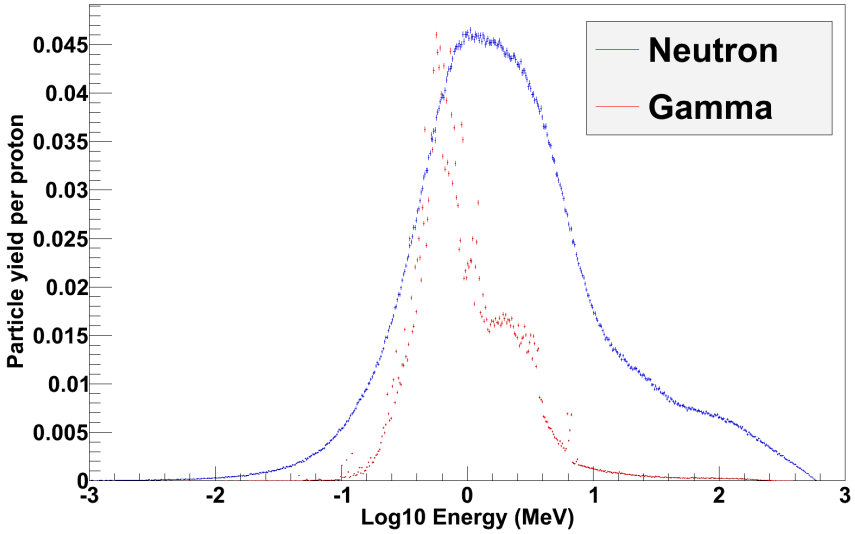

Figure 8.4: Neutron and gamma spectrum leaking from the target

The shielding model given in figure 8.5 consists of boronated steel (7.87 g/cm3) and boronated concrete (3.1 g/cm3). The composition of borated steel and concrete are summarized in tables A.12 and A.13 respectively. While the inner 200 cm is made up of boronated steel (divided into 4 layers of equal thickness), the outer layer of 50 cm thickness is made up of boronated concrete. The transmutation zone (blanket) has been modeled by a homogeneous material composition. However, the contribution of the fission neutrons to the neutron flux level in the iron layer is of minor effect if included in the low energy part of the spallation neutron spectum. This is due to the fact that the low energy part of the spectrum is already attenuated in the first shielding layer. An iron shielding of 200 cm corresponds to about 45 (HVL) half-value layers of attenuation for fission neutrons [Shapiro, 2002]. This effect has been analyzed by additional simulations using FLUKA for the entire model consisting of the shielding structures as well as the transmutation zone as shown in figure 8.5. Accordingly, very high energy neutrons as well as fission neutrons are efficiently attenuated in the steel layers resulting in a low energy spectrum. This flux level is a result of the superimposition of the spallation and fission

neutrons and hence independent of the source (fission or spallation).

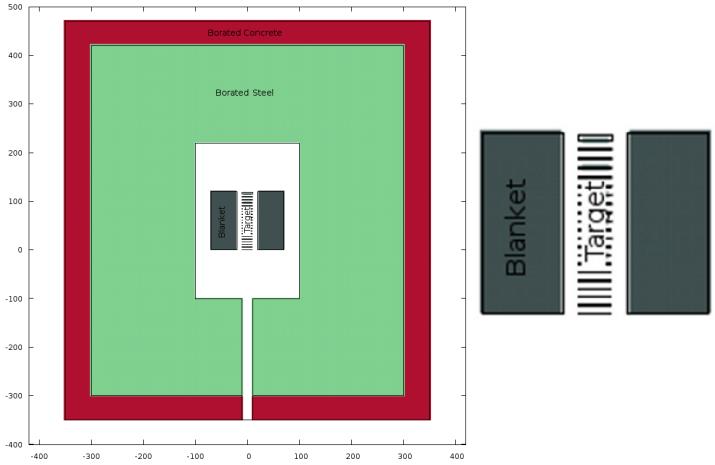

Figure 8.5: FLUKA model used in the simulation of shielding behaviour

The results of the simulation on the behavior of neutron flux incident on the different layers of the shielding in the outward direction are illustrated in figures 8.6 and 8.7 respectively. Additionally, result from FLUKA simulation for the entire model consisting of the shielding structures as well as the transmutation zone as shown in figure 8.8. It shows that iron is very efficient in attenuating the high energy tail of the spectrum. Each layer attenuates high energy neutrons by about an order of magnitude. Meanwhile there is a buildup of low energy neutrons in the lower energy range of about a few keV after about four layers of iron as the lowest inelastic energy level of iron is beyond this energy range. Following is the effect of final layer of concrete in attenuating these low energy neutrons at least by two orders of magnitude. Hence the proposed and modeled shielding structures with a thick inner layer of iron followed by concrete is the effective configuration in attenuating the neutron spectrum with a broad energy range.

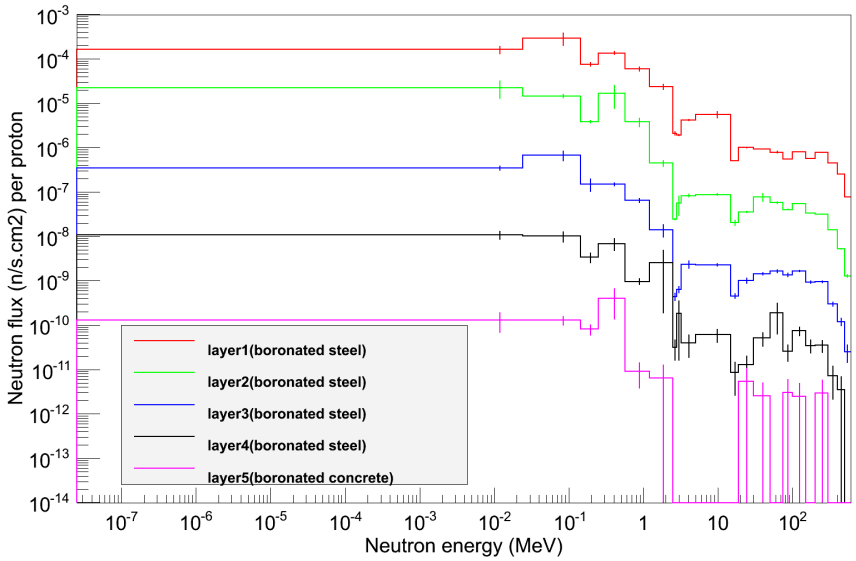

Figure 8.6: Neutron spectrum in different layers of the shielding (forward direction)

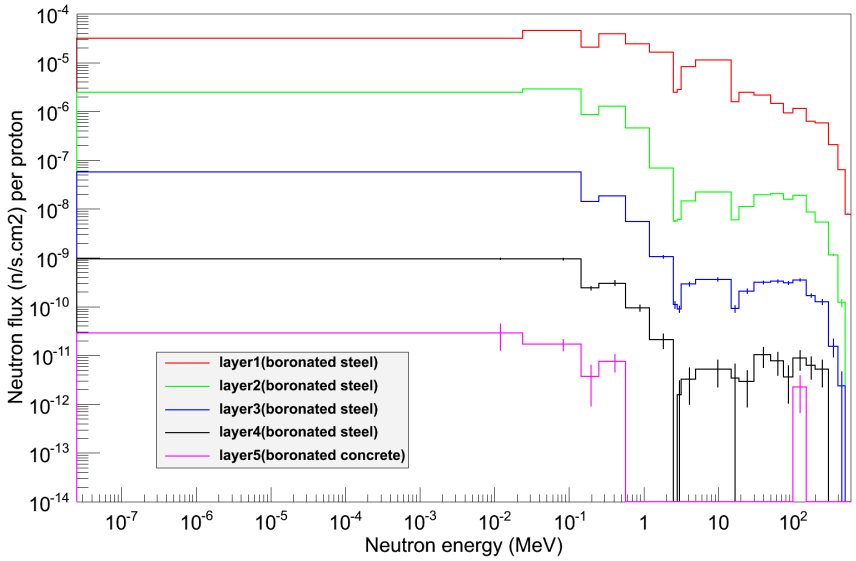

Figure 8.7: Neutron spectrum in different layers of the shielding (sideward direction)

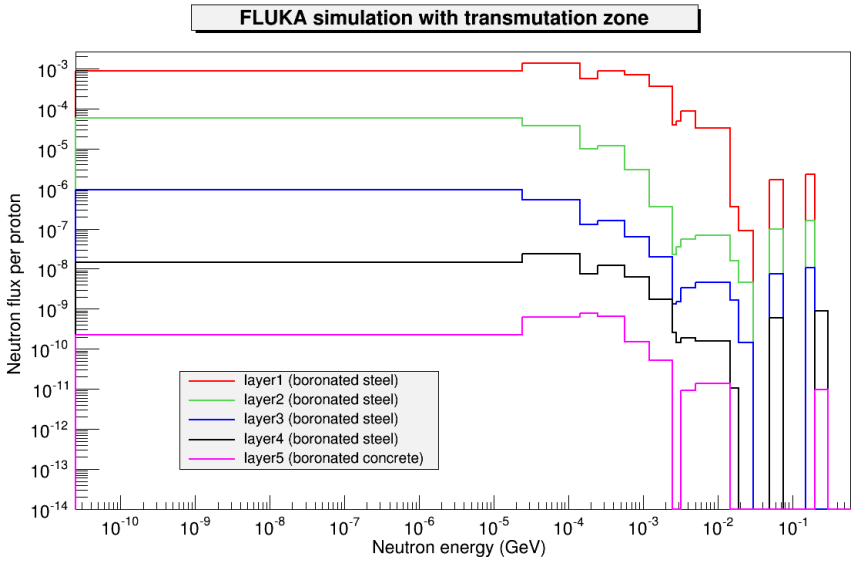

Figure 8.8: Neutron spectrum in different layers of the shielding (forward direction) including transmutation zone

By comparison, the shielding design calculations for the EURISOL multi-MW target have yielded shielding dimensions of 1 m thick monolith steel shield encapsulating the target followed by 7-9 m of concrete [Felcini et al., 2006]. By using borated shielding materials, the shielding dimensions can be greatly reduced, also reducing the volume of activated materials. The attenuation of gammas, as seen in figures 8.9 and 8.10 is rather insensitive to the kind of material (of low atomic number) used in the shielding. A decreasing flux of gammas is observed with increasing thickness of the shielding. Ideally, a material with high atomic number is efficient as a shield against the gammas. But as the radiation weighting factors is higher for neutrons when compared to gammas, shielding of neutrons takes precedence before shielding of gammas. A sufficiently thick layer of the composite shielding of iron and concrete shields the gamma radiation effectively.

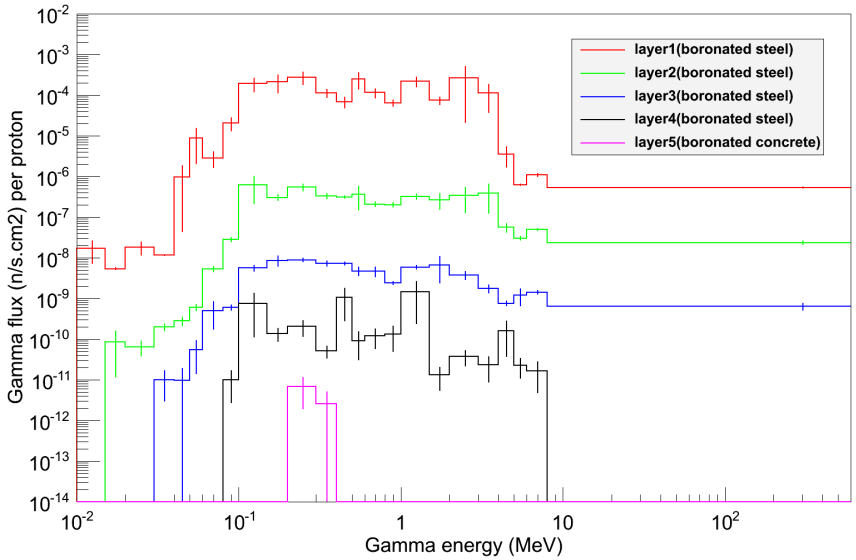

Figure 8.9: Gamma spectrum in different layers of the shielding (forward direction)

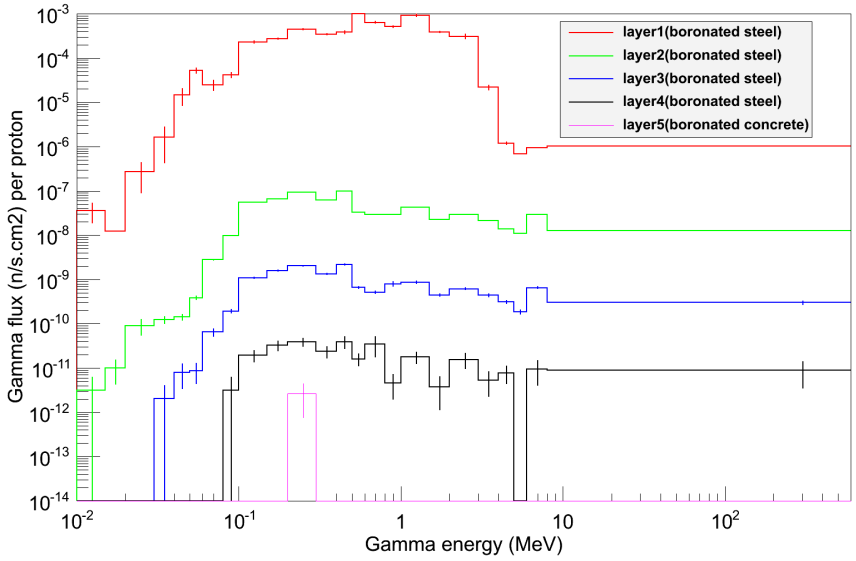

Figure 8.10: Gamma spectrum in different layers of the shielding (sideward direction)

CHAPTER 9

Conclusions and Outlook

Transmutation of highly radioactive nuclear waste can be performed using an ADSS, where high energy protons impinge on a spallation target to produce neutrons. These neutrons are multiplied in a sub-critical system, while simultaneously fissioning the MAs into short-lived or stable nuclides. AGATE is a project envisaged to demonstrate the feasibility of transmutation in a gas cooled ADS using solid spallation target. Development of the spallation target and assessing the safety aspects in the STM are the main highlights of this work. According to the AGATE concept parameters, 600 MeV protons are delivered on to the segmented tungsten spallation target, cooled using helium. Tungsten is an ideal solid spallation target material because of its high melting point, other than the many desirable properties.

Spallation is by far the most attractive means of neutron production when it comes to energy deposition per neutron (about 50 MeV per neutron leaked from the target). Hence it finds many scientific and engineering applications. The spallation mechanism initiates with an INC, leaving the nuclei in an excited state. Further, these nuclei exhibit de-excitation through different channels such as evaporation, multi-fragmentation and fission. Both the INC and de-excitation processes lead to the production of neutrons and spallation products. Spallation neutron energy spectrum is relatively harder compared to fission because of the higher energetics involved. For 600 MeV protons on tungsten, about 30% of the neutrons have energy greater than 1 MeV, a small fraction of them, which are energetic in nature are emitted in the forward direction. Life time of the spallation products are relatively shorter compared to MAs.

The monte carlo toolkit Geant4 has been used in the simulation of particle transport. Binary cascade is used to simulate INC, along with the G4NDL neutron data library for low energy neutrons (< 20 MeV). The results from various simulations are normalized per incident proton or per mA current, so that the results could be scaled to higher or lower proton currents.

Particle Production Study

From the systematics study of incident projectile types (proton, deuteron and ^{4}He), neutron yield due to proton and deuteron are generally higher than that for ^{4}He. At higher energies, deuteron fares better than proton. Given the lower kinetic energy of proton (600 MeV) and owing to the fact that acceleration cost increases with increasing mass, proton turns out to be the ideal projectile for the current system. Energy cost of neutron production is the most efficient for protons of energy between 800 - 1000 MeV. Nuclear

collision probability increases with increasing proton energy, reaching a saturation value at about 1 GeV for tungsten. At 600 MeV, the nuclear collision probability in tungsten is about 80% for protons.

Parametric expressions are available which describe the neutron yield pretty well, according to which the neutron yield is a linear function of material mass number. Consequently, to obtain a neutron yield of about 10 neutrons per 600 MeV proton, the minimum mass number of the target material is at least 160. Hence the spallation material options are limited to lanthanides, period 6 elements and actinides. Lanthanides are limited in resource and actinide targets produce other actinide spallation products(due to peripheral collisions, quasi-elastic reactions and activation). The spallation materials that are presently used or proposed come mainly from period 6, such as, tantalum, tungsten, mercury, lead, bismuth and gold. The other materials that emerge out of the study are hafnium and thallium, which probably are good candidate materials respectively for solid and liquid targets. As far as it is known, detailed study of these two materials as spallation material candidates is still missing.

To ensure maximumi interaction, the target length needs to be as long as the range of protons in the material. For 600 MeV protons, the range is about 15 cm in tungsten. There exists an optimum radius of the target determining the neutron yield. While lower radii means the leakage of energetic secondaries without producing further neutrons, larger radii results in the parasitic absorption. For tungsten, target radius of about 10 cm turns out to be a good option.

Neutron leakage and gamma production in monoliths of W, Hg and Pb are comparable with each other. In all the cases, two spallation products are formed per neutron produced. In tungsten there is higher neutron production leading to more spallation products. A significant portion of neutrons leak from the front side of the monolith targets as the there is neutron build-up site near the target head.

About 70% of the beam power is lost in target heating for all materials at 600 MeV. Protons, both primary and secondary are responsible for more than 80% of energy deposition in the target. To facilitate adequate cooling of the target and to distribute the neutron yield along the length of the target, segmentation of the target is necessary.

Target Development

The development of the tungsten target may be seen as a transformation from the simple monolith through the segmented target to the target optimized for the AGATE concept. In the monolith case, neutron build-up near the target head is not very suitable to illuminate the sub-critical core coupled to the target. High power densities are reached in the target which is difficult to be cooled. Hence segmentation of the target is necessary to produce a homogenized neutron field. This also leads to the hardening of the emitted neutron energy spectrum. The flux-traps allow efficient cooling of the target. The other advantages of segmentation are reduced neutron leakage from the front target surface and reduced parasitic absorption in the target. These advantages are not exclusively for solid targets, rather holds true even in the liquid target domain.

Three different tungsten target configurations are studied, monolith, target with equally thick segments (segmented target) and segmented target with variable thicknesses of the segments (optimized target). All the targets are 10 cm in radius and about 18 cm in solid target length. The latter two configurations have elongated lengths due to the inclusion of 5 cm flux-traps between the segments.

Maximum power density and the beam power deposited in the target are in decreasing order accordingly for the monolith (0.79 kW/cm^3 per mA, 0.46 MW per mA), the segmented (0.73 kW/cm^3 per mA, 0.35 MW per mA) and the optimized (0.69 kW/cm^3 per mA, 0.32 MW per mA) targets. Though the total neutron intensity decreases in this sequence, the lateral neutron intensity is increasing (3.75×10^{16} n/s per mA, 4.68×10^{16} n/s per mA, 4.39×10^{16} n/s per mA). This is because of more neutron leakage from the front and back surfaces in the monolith case, while more neutron leakage from the lateral surface in the other two cases. Given that the lateral neutron leakage is more suitable of applications, the optimized target is advantageous than its predecessor targets, in terms of power density and lateral neutron intensity performance. Gamma production in the optimized target is reduced by about a factor of four when compared to the monolith. About two spallation products are created per neutron produced in the monolith and this ratio is even less than one in the optimized target.

About 30% of the neutrons produced leak from the monolith, while it is about 70% in the optimized target due to flux-traps. The optimized target is characterized by lower neutron inelastic reaction probability, because of leaking high energy neutrons, thereby increasing the mean neutron energy to 2.24 MeV from 0.55 MeV than in the monolith case. Leakage of high energy neutrons is also an advantage in the optimized target because of further reduction in activation and damage problems.

Power density in the optimized target is still very high to be cooled. Fluidizing the target with pebbles instead of solid material is a feasible option. Thermal hydraulic studies of the first segment of the optimized pebble bed target indicates that the maximum temperature reached in the tungsten pebbles is about 670 °C, which is well below the recrystallization temperature (1350 °C) and melting point (3410 °C) of tungsten. Such study needs to be performed for all the segments of the fluidized target in order to assess the holistic feasibility of the target in terms of cooling.

Major drawback of the optimized target is the leakage of high energy protons. While there are hardly any protons leaking from the monolith, it increases by about an order for the optimized target. Making the target radially composite is envisaged as a feasible solution, whose influence on the neutron leakage behavior could be analyzed in a further study. Approximately 70 % of the proton energy is converted to heat - plays an important role in the gas cooled ADS concept. Hence, optimization of power density in the target needs to be studied a step deeper. Further configuration options of the target in this regard include using slanted or curved segments instead of flat ones, reduced target material density and rotating target. It is also important to learn the functional response of the target due to accelerator transients such as beam trips, in order to establish the allowable duration and frequency of beam trips.

Radiation Damage and Radiation Safety

The model for mechanism of atomic displacements is based on NRT theory. Target and PBW suffer large radiation damage due to their direct interaction with the proton beam. High energy protons have the highest damage capacity. But low energy neutrons also induce significant damage because of their high density in the components. Damage is significant in the first few segments of the target, decreasing gradually with increasing tungsten length. Maximum damage in the target is inflicted on the first segment, about 4.5 dpa/FPY per mA and the total damage is about 53 dpa/FPY per mA. Total helium production in the target is about 7340 appm/FPY per mA. The life time of the tungsten target is roughly approximated to be 1.5 years per mA and full power operation.

However, additional investigations such as tensile, fatigue and bending tests are necessary to practically determine the life time of the target. Radiation damage in the PBW is comparatively lower (0.81 dpa/FPY per mA and 149 helium appm/FPY per mA).

Total specific activity in the target at shutdown after one FPY operation is about 2.4×10^{14} MBq/g per mA. Production cross section of ^{148}Gd is about 2.4 mb in the target. Other significant alpha emitters are ^{146}Sm and ^{154}Dy. Isotopes contributing large amounts of specific activity in the target are positron emitters such as, ^{172}Hf, ^{173}Lu, ^{174}Lu and ^{179}Ta. The hard gamma emitter, ^{60}Co is also present in significant amounts in the target. Unlike the actinides, which need to be transmuted, radionuclides produced in the target are less radiotoxic and have shorter life time. Major radionuclides in PBW cooling water are ^{7}Be and ^{11}C, and additionally in aluminum are ^{18}F, ^{22}Na and ^{24}Na. Major nuclides produced in the components are identified and quantified. It is necessary to further study the radiological implications of these radionuclides on the biosphere.

Spallation produces high energy neutrons and gammas which need to be shielded. An additional dimension in the shielding calculation is introduced by the high energy forward-peaked neutrons. The shielding consists of 5 layers, each layer 50 cm thick, both in the forward and sideward directions. The first four layers are made up of boronated steel and the final layer is made up of boronated concrete. Using boronated materials greatly reduce the shielding dimensions while exhibiting good shielding performance. This also reduces the amount of activated materials. An inner thick layer of iron is required to attenuate the high energy of neutrons. The concrete block following this is efficient in shielding against the low energy neutrons. With the same shielding material configuration, gammas tend to attenuate relatively faster than the neutrons.

From the nuclear simulation of the graphite beam stop, it has been found out that the neutron flux around the stop is very less and the maximum power density is about 5 times lesser than that in the tungsten target. The only significant isotope produced is ^{7}Be, leading to lower activation and complimenting the other advantages of the graphite beam stop.

Bibliography

[IAEA, 1988] (1988). Radiological safety aspects of the operation of proton accelerators. Technical Report Series 283, IAEA.

[NEA, 1994] (1994). Overview of physics aspects of different transmutation concepts. Technical report, NEA.

[IAEA, 1997] (1997). Accelerator driven systems: Energy generation and transmutation of nuclear waste. Technical Report IAEA-TECDOC-985, IAEA.

[ESS, 2002] (2002). The ess project volume iii technical report.

[IAEA, 2004] (2004). Implications of partitioning and transmutation in radioactive waste management. Technical Report TECHNICAL REPORTS SERIES No. 435, IAEA.

[KENS, 2004] (2004). Review of the neutron science laboratory kens in the high energy accelerator research organization kek, japan. Technical report.

[NEA, 2005] (2005). Accelerator and spallation target technologies for ads applications. Technical Report NEA No. 5421, NEA.

[IAEA, 2008a] (2008a). Cyclotron Produced Radionuclides: Principles and Practice. Technical Report Technical Reports Series No. 465, IAEA.

[MCNPX, 2008] (2008). Mcnpx 2.6.0 manual. Technical Report LA-CP-07-1473, Los Alamos Laboratory.

[IAEA, 2008b] (2008b). Spent fuel reprocessing options. Technical Report IAEA-TECDOC-1587, IAEA.

[IAEA, 2009] (2009). Advanced reactor technology options for utilization and transmutation of actinides in spent nuclear fuel. Technical Report IAEA-TECDOC-1626, IAEA.

[CIA, 2009] (2009). *The World Factbook 2009*. Central Intelligence Agency, Washington, DC.

[AGATE, 2010] (2010). AGATE feasibility study.

[IAEA, 2010] (2010). Annual report. Technical report, IAEA.

[Geant4, 2010] (2010). Geant4 physics reference manual. Technical report. Version: geant4 9.4.

[CEA, 2010] (2010). Second advanced workshop on model codes for spallation reactions.

[AGATE, 2011] (2011). Konzept einer gasgekuehlten beschleunigergetriebenen transmutationsanlage. Synthese Report ISBN 978-3-941277-11-3, Institut fuer Nuklearen Brennstoffkreislauf der RWTH Aachen, Elisabethstraße 16, D-52062 Aachen.

[IAEA, 2011] (2011). Nuclear technology review. Technical report, IAEA.

[ATW, 2012] (2012). Accelerator transmutation of waste. http://www.lanl.gov/orgs/pa/science21/ATW.html.

[IAEA, 2012] (2012). Benchmark of spallation models. http://nds121.iaea.org/alberto/mediawiki-1.6.10/index.php/Main_Page.

[MEDICIS, 2012] (2012). Cern-medicis. http://cdsweb.cern.ch/journal/CERNBulletin/2012/14/News%20Articles/1434420.

[ESS, 2012] (2012). European spallation source. http://ess-scandinavia.eu.

[Geant4, 2012] (2012). Geant4. http://geant4.cern.ch.

[IPNS, 2012] (2012). Intense pulsed neutron source. http://www.aai.anl.gov/history/project_pages/ipns.html.

[LNSC, 2012] (2012). Los alamos neutron science center. http://lansce.lanl.gov/.

[MLF, 2012] (2012). Materials and life science experimental facility (mlf). http://j-parc.jp/MatLife/en/facilities/pbw.html.

[MIT, 2012] (2012). MIT OpenCourseWare. http://ocw.mit.edu/courses/nuclear-engineering/22-101-applied-nuclear-physics-fall-2006/lecture-notes/lec10.pdf.

[MYRRHA, 2012] (2012). Myrrha: Multi-purpose hybrid research reactor for high-tech applications. http://www.sckcen.be/en/Our-Research/Research-domains/Advanced-nuclear-systems-GEN-IV-MYRRHA-ADS.

[NIST, 2012] (2012). Neutron sources around the world. http://www.ncnr.nist.gov/nsources.html.

[MTS, 2012] (2012). Properties of tungsten. http://www.tungsten.com/.

[USGS, 2012] (2012). Rare earth elements - critical resources for high technology. http://pubs.usgs.gov/fs/2002/fs087-02/. Fact Sheet 087-02.

[ISIS, 2012] (2012). Rutherford appleton laboratory. http://www.isis.stfc.ac.uk/index.html.

[SNS, 2012] (2012). Spallation neutron source. http://neutrons.ornl.gov/facilities/SNS/.

[PSTAR, 2012] (2012). Stopping-power and range tables for protons. http://physics.nist.gov/PhysRefData/Star/Text/PSTAR.html.

[SINQ, 2012] (2012). Swiss spallation neutron source. http://www.psi.ch/sinq/.

[TEF, 2012] (2012). Transmutation experimental facility. `http://j-parc.jp/Transmutation/en/index.html`.

[Wiki, 2012] (2012). Wikipedia. `http://en.wikipedia.org/wiki/Main_Page`.

[Abderrahim et al., 2001] Abderrahim, H., Kupschus, P., Malambu, E., Benoit, P., Tichelen, K. V., Arien, B., Vermeersch, F., D'hondt, P., Jongen, Y., Ternier, S., and Vandeplassche, D. (2001). Myrrha: A multipurpose accelerator driven system for research and development. *Nuclear Instruments and Methods in Physics Research Section A: Accelerators, Spectrometers, Detectors and Associated Equipment*, 463(3):487 – 494.

[Abe, 1996] Abe, K. (1996). Study of neutron absorption in tungsten.

[Ablett et al., 2006] Ablett, J., Ackerman, A., Alforque, R., Allaire, M., and Arena, D. (2006). Conceptual design report, national synchrotron light source ii. Technical report, Brookhaven National Laboratory.

[Agostinelli et al., 2003] Agostinelli, S., Allison, J., Amako, K., Apostolakis, J., Araujo, H., Arce, P., Asai, M., Axen, D., Banerjee, S., Barrand, G., Behner, F., et al. (2003). Geant4 - a simulation toolkit. *Nuclear Instruments and Methods in Physics Research Section A: Accelerators, Spectrometers, Detectors and Associated Equipment*, 506(3):250 – 303.

[Allison et al., 2006] Allison, J., Amako, K., Apostolakis, J., Araujo, H., Dubois, P., Asai, M., Barrand, G., Capra, R., Chauvie, S., Chytracek, R., Cirrone, G., et al. (2006). Geant4 developments and applications. *Nuclear Science, IEEE Transactions on*, 53(1):270 –278.

[Amian et al., 1993] Amian, W., Byrd, R., Clark, D., Goulding, C., Meier, M., Morgan, G., and Moss, C. (1993). Differential neutron production cross sections for 597-mev protons. *Nuclear Science and Engineering*, 115(ISSN 0029-5639):1.

[Ammerman et al.,] Ammerman, C., Woloshun, K., He, X., James, M., Li, N., Tcharnotskaia, V., and Wender, S. Conceptual designs for a spallation neutron target constructed of a helium-cooled, packed bed of tungsten particles.

[Armstrong et al., 1981] Armstrong, T. W., Cloth, P., Filges, D., and D., N. R. (1981). Theoretical target physics studies for the snq spallation neutron source. Technical Report ISSN 0343-7639, KFA Jülich.

[Artisyuk et al., 2002] Artisyuk, V., Saito, M., Stankovskii, A., Korovin, Y., and Shmelev, A. (2002). Radiological hazard of long-lived spallation products in accelerator-driven system. *Progress in Nuclear Energy*, 40:637 – 645.

[Atchison et al., 2005] Atchison, F., Baumann, P., Brys, T., Daum, M., Egorov, A., Fierlinger, P., Fuchs, P., Henneck, R., Joray, S., Keil, R., Kirch, K., Krutova, R., Kühne, G., Lebedev, V., Obermeier, H., Orlova, D., Perret, C., Pichlmaier, A., Richard, P., Serebrov, A., and Thies, S. (2005). On the use of lead/tin alloys as target material for the production of spallation neutrons. *Nuclear Instruments and Methods in Physics Research Section A: Accelerators, Spectrometers, Detectors and Associated Equipment*, 539(3):646 – 653.

[Bacon et al., 1997] Bacon, D., Calder, A., and Gao, F. (1997). Defect production due to displacement cascades in metals as revealed by computer simulation. *Journal of Nuclear Materials*, 251(0):1 – 12. Proceedings of the International Workshop on Defect Production, Accumulation and Materials Performance in an Irradiation Environment.

[Battistoni et al., 2006] Battistoni, G., Muraro, S., Sala, P. R., Cerutti, F., Ferrari, A., Roesler, S., Fass'o, A., and Ranft, J. (2006). The fluka code: Description and benchmarking. In *Proceedings of the Hadronic Shower SimulationWorkshop*, Fermilab.

[Bauer, 2001] Bauer, G. (2001). Physics and technology of spallation neutron sources. *Nuclear Instruments and Methods in Physics Research Section A: Accelerators, Spectrometers, Detectors and Associated Equipment*, 463(3):505 – 543. Accelerator driven systems.

[Bauer, 2010] Bauer, G. (2010). Overview on spallation target design concepts and related materials issues. *Journal of Nuclear Materials*, 398:19–27. Forschungszentrum Jülich, D-52425 Jülich, Germany.

[Bauer, 2005] Bauer, G. S. (2005). Target design and technology for research spallation neutron sources. Workshop on "Technology and Applications of Accelerator Driven Systems (ADS)", Trieste - Italy.

[Beller et al., 2001] Beller, D. E., Tuyle, G. J. V., Bennett, D., Lawrence, G., Thomas, K., Pasamehmetoglu, K., Li, N., Hill, D., Laidler, J., and Fink, P. (2001). The u.s. accelerator transmutation of waste program. *Nuclear Instruments and Methods in Physics Research Section A: Accelerators, Spectrometers, Detectors and Associated Equipment*, 463(3):468 – 486. Accelerator driven systems.

[Benlliure, 2006] Benlliure, J. (2006). Spallation reactions in applied and fundamental research. *Lecture Notes in Physics*, 238:191–238.

[Benlliure et al., 2001] Benlliure, J., Armbruster, P., Bernas, M., Boudard, A., Dufour, J., Enqvist, T., Legrain, R., Leray, S., Mustapha, B., Rejmund, F., Schmidt, K.-H., et al. (2001). Isotopic production cross sections of fission residues in 197au-on-proton collisions at 800 a mev. *Nuclear Physics A*, 683(1-4):513 – 539.

[Biss, 2012] Biss, K. (2012). *Untersuchung des Transmutationsverhaltens von Transuranen in einer gasgekühlten ADS-Anlage*. PhD thesis, Institute of Nuclear Fuel Cycle (INBK), RWTH Aachen University.

[Blomgren et al., 2010] Blomgren, J., Karlsson, F., Pomp, S., and Aneheim, E. (2010). Partitioning and transmutation current developments - 2010. Technical Report TR-10-35, Swedish Nuclear Fuel and Waste Management Co.

[Broeders and Konobeyev, 2005] Broeders, C. and Konobeyev, A. (2005). Displacement cross-sections for tantalum and tungsten irradiated with protons at energies up to 1 gev. *Journal of Nuclear Materials*, 336:201 – 209.

[Broeders et al., 2005] Broeders, C., Konobeyev, A., and Villagrasa, C. (2005). Neutron displacement cross-sections for tantalum and tungsten at energies up to 1 Gev. *Journal of Nuclear Materials*, 342:68 – 76.

[Broome, 1996] Broome, T. (1996). High power targets for spallation sources. In *EPAC96*, Sitges, Spain.

[Bungau et al., 2010] Bungau, A., Cywinski, R., and Bungau, C. (2010). Target optimisation studies for the european spallation source. In *IPAC'10 - Proceedings of the 1st International Particle Accelerator Conference*, pages 256–258. IPAC 10 OC/ACFA, Kyoto, Japan.

[Bungau et al., 2009] Bungau, A., Cywinski, R., and Lord, J. (2009). Geant4 simulations of the isis muon target at rutherford appleton laboratory. In *Proceedings of the 23rd Particle Accelerator Conference*, PAC09, pages 1400–1402. JACOW, Vancouver, Canada.

[Bungau et al., 2008] Bungau, C., Tygier, S., Barlow, R., and Cywinski, R. (2008). Accelerator driven systems for energy production and waste transmutation. Session : TUPP147 - 24 JUNE 2008 Poster Session.

[Butzek et al., 2003] Butzek, M., Kulessa, T., and Wolters, J. (2003). Proton beam window for high current densities. ESS- Report ESS 03-147-T, Forschungszentrum Jülich GmbH.

[Canada, 2007] Canada, D. R. (2007). Geant4 particle simulations in support of the neutron interrogation project. Technical Report DRDC-SUFFIELD-CR-2008-235, Suffield, Ralston ALTA (CAN);ANS Technologies Inc., Montreal QC (CAN).

[Carpenter, 1977] Carpenter, J. M. (1977). Pulsed spallation neutron sources for slow neutron scattering. *Nuclear Instruments and Methods*, 145(1):91 – 113.

[Chou, 2003] Chou, W. (2003). Spallation neutron source and other high intensity proton sources.

[Coninx, 2011] Coninx, S. (2011). Untersuchung des schnellen anfahrens/wiederanfahrens eines ads-systems. Diplomarbeit, RHEINISCHE FACHHOCHSCHULE KÖLN.

[Cugnon et al., 1997] Cugnon, J., Volant, C., and Vuillier, S. (1997). Nucleon and deuteron induced spallation reactions. *Nuclear Physics A*, 625(4):729 – 757.

[Dai et al., 2006] Dai, Y., Henry, J., Auger, T., Vogt, J.-B., Almazouzi, A., Glasbrenner, H., and Groeschel, F. (2006). Assessment of the lifetime of the beam window of megapie target liquid metal container. *Journal of Nuclear Materials*, 356(1?3):308 – 320. Proceedings of the Seventh International Workshop on Spallation Materials Technology, Proceedings of the Seventh International Workshop on Spallation Materials Technology.

[Dementyev et al., 1996] Dementyev, A., Sobolevsky, N., and Stavissky, Y. (1996). Neutron yield from extended lead target under incident protons of 0.1 to 100 gev. *Nuclear Instruments and Methods in Physics Research Section A: Accelerators, Spectrometers, Detectors and Associated Equipment*, 374(1):70 – 72.

[Efthymiopoulos, 2011] Efthymiopoulos, I. (2011). New target concepts. CERN Accelerator School: High Power Hadrons Machines.

[Eidelman et al., 2004] Eidelman, S., Hayes, K., Olive, K., Aguilar-Benitez, M., Amsler, C., Asner, D., Babu, K., Barnett, R., Beringer, J., Burchat, P., Carone, C., et al. (2004). Review of Particle Physics. *Physics Letters B*, 592.

[Enparantza et al., 2010] Enparantza, R., Ariz, I., Romano, P., and Sedano, A. (2010). Beam stop design and construction for the front end test stand at isis. In *Proceedings of IPAC10, Kyoto, Japan.*

[Enqvist et al., 2001] Enqvist, T., Wlazo, W., Armbruster, P., Benlliure, J., Bernas, M., Boudard, A., Czajkowski, S., Legrain, R., Leray, S., Mustapha, B., Pravikoff, M., Rejmund, F., Schmidt, K.-H., Stéphan, C., Taieb, J., Tassan-Got, L., and Volant, C. (2001). Isotopic yields and kinetic energies of primary residues in 1 A gev 208Pb+p reactions. *Nuclear Physics A*, 686(1-4):481 – 524.

[Fasil'kov et al., 1995] Fasil'kov, R., Myzin, N., and Chirkin, Y. (1995). Neutron yield from a massive lead target under the action of relativistic lightions. *Atomic Energy*, 79:664–670.

[Felcini et al., 2006] Felcini, M., Herrera-Martinez, A., Kadi, Y., Otto, T., and Tecchio, L. (2006). Design of the eurisol multi-mw target assembly: Radiation and safety issues. In *Shielding Aspects of Accelerators, Targets and Irradiation Facilities - SATIF 8*, pages 105–114.

[Ferrari and Sala, 1996] Ferrari, A. and Sala, P. (1996). The physics of high energy reactions. Proc. Workshop on Nuclear Reaction Data and Nuclear Reactors Physics, Design and Safety, International Centre for Theoretical Physics, Miramare-Trieste, Italy.

[Filges and Goldenbaum, 2010] Filges, D. and Goldenbaum, F. (2010). *Handbook of Spallation Research: Theory, Experiments and Applications.* Wiley-VCH.

[Folger et al., 2004] Folger, G., Ivanchenko, V. N., and Wellisch, J. P. (2004). The binary cascade. *The European Physical Journal A - Hadrons and Nuclei*, 21:407–417.

[Gaarde, 1991] Gaarde, C. (1991). Isobar excitations in nuclei. *Annual Review of Nuclear and Particle Science*, 41(1):187–218.

[GAO, 2011] GAO (2011). Nuclear fuel cycle options. Technical Report GAO-12-70, United States Government Accountability Office.

[Gardner, 1998] Gardner, I. S. K. (1998). A review of spallation neutron source accelerators.

[Goldenbaum, 2003] Goldenbaum, F. (2003). *The Physics of Spallation Processes - Theory, Experiments and Applications.* Forschungszentrum Jülich, Zentralbibliothek.

[Goldstone, 1991] Goldstone, J. A. (1991). The manuel lujan, jr. neutron scattering center (lansce). *Neutron News*, 2(2):7–13.

[Gollon, 1976] Gollon, P. J. (1976). Production of radioactivity by particle accelerators. *Nuclear Science, IEEE Transactions on*, 23(4):1395 –1400.

[Green et al., 1988] Green, S., Green, W., Hegedus, F., Victoria, M., Sommer, W., and Oliver, B. (1988). Production of helium by medium energy (600 and 800 mev) proton. *Journal of Nuclear Materials*, 155-157, Part 2(0):1350 – 1353.

[Green, 1984] Green, S. L. (1984). Calculated radiation damage effects of high energy proton beams. *Journal of Nuclear Materials*, 126(1):30 – 37.

[Haines et al., 2011] Haines, J., Riemer, B., Futakawa, M., Wagner, W., and Wohlmuther, M. (2011). Operational experience for high power spallation targets. 4th High Power Targetry Workshop. Malmö, Sweden.

[Hanslik, 2006] Hanslik, R. (2006). Sicherheitstechnische analyse und auslegungsaspekte von abschirmungen gegen teilchenstrahlung am beispiel von spallationsanlagen im megawatt bereich. Technical Report Berichte des Forschungszentrums Jülich JUEL-4225, Forschungszentrum Jülich.

[Heikkinen, 2009] Heikkinen, A. (2009). *Geant4 Hadronic Cascade Models and CMS Data Analysis : Computational Challenges in the LHC era*. PhD thesis, University of Helsinki.

[Herrera-Martínez, 2004] Herrera-Martínez, A. (2004). *Transmutation of Nuclear Waste in Accelerator-Driven Systems*. PhD thesis, University of Cambridge.

[Hilscher et al., 2001] Hilscher, D., Herbach, C.-M., Jahnke, U., Tishchenko, V., Enke, M., Filges, D., Goldenbaum, F., Neef, R.-D., Nunighoff, K., Paul, N., Schaal, H., Sterzenbach, G., Letourneau, A., Bohm, A., Galin, J., Lott, B., Peghaire, A., and Pienkowski, L. (2001). Helium production for 0.8-2.5 gev proton induced spallation reactions, damage induced in metallic window materials. *Journal of Nuclear Materials*, 296(1):83–89.

[Hilscher et al., 1998] Hilscher, D., Jahnke, U., Goldenbaum, F., Pienkowski, L., Galin, J., and Lott, B. (1998). Neutron production by hadron-induced spallation reactions in thin and thick Pb and U targets from 1 to 5 GeV. *Nuclear Instruments and Methods in Physics Research Section A: Accelerators, Spectrometers, Detectors and Associated Equipment*, 414(1):100 – 116.

[Howard, 2006] Howard, A. (2006). Validation of neutrons in geant4 using tarc data - production, interaction and transportation. In *Nuclear Science Symposium Conference Record, 2006. IEEE*, volume 3, pages 1506 –1510.

[IAEA, 2004] IAEA (2004). Development opportunities for small and medium scale accelerator driven neutron sources. Technical Report IAEA TECDOC 1439, IAEA.

[Jansen, 1995] Jansen, C. (1995). *Protonenfenster und Flüssigmetall-target für eine beschleunigergetriebene Transmutationsanlage*. PhD thesis, Research Center Juelich.

[Jones et al., 2009] Jones, F., Baartman, R., and Rao, Y.-N. (2009). Using geant4-based tools to simulate a proton extraction and transfer line. In *Proceedings of tenth International Computational Accelerator Physics conference (ICAP09)*, San Francisco.

[Kadi, 2003] Kadi, Y. (2003). Iaea workshop: Technology and applications of accelerator driven systems.

[Kadi and Revol, 2002] Kadi, Y. and Revol, J. (2002). Design of an accelerator-driven system for the destruction of nuclear waste. ICTP Lecture Notes Series, Volume 12. (ISBN 92-95003-17-9).

[Kato and Nakamura, 2001] Kato, T. and Nakamura, T. (2001). Analytical method for calculating neutron bulk shielding in a medium-energy accelerator facility. *Nuclear Instruments and Methods in Physics Research Section B: Beam Interactions with Materials and Atoms*, 174(4):482 – 490.

[Kelley et al., 2005] Kelley, K., Hertel, N., Pitcher, E., Devlin, M., and Mashnik, S. (2005). 148gd production cross section measurements for 600- and 800-mev protons on tantalum, tungsten, and gold. *Nuclear Physics A*, 760(3?4):225 – 233.

[Khripunov et al., 1997] Khripunov, V., Santoro, R., and Khater, H. (1997). Profit from borating concrete in the iter biological shield. In *Fusion Engineering, 1997. 17th IEEE/NPSS Symposium*, volume 2, pages 991 –994 vol.2.

[Kim et al., 2006] Kim, J., sup Gil, C., Maeng, W., and Kim, D. (2006). Design of a high energy proton beam dump for komac. *Nuclear Instruments and Methods in Physics Research Section A: Accelerators, Spectrometers, Detectors and Associated Equipment*, 562(2):997 – 1000. Proceedings of the 7th International Conference on Accelerator Applications-AccApp05-7th International Conference on Accelerator Applications.

[Koprivnikar, 2001] Koprivnikar, I. (2001). *The Biological Shield of High Intensity Spallation Sources: A Monte Carlo Design Study.* PhD thesis, Graz University.

[Koprivnikar and Schachinger, 2002] Koprivnikar, I. and Schachinger, E. (2002). The biological shield of a high-intensity spallation source: a monte carlo design study. *Nuclear Instruments and Methods in Physics Research Section A: Accelerators, Spectrometers, Detectors and Associated Equipment*, 487(3):571 – 584.

[Krása, 2010] Krása, A. (2010). Spallation reaction physics. Lecture Notes on "Neutron Sources for ADS".

[Lamarsh and Baratta, 2001] Lamarsh, J. R. and Baratta, A. J. (2001). *Introduction to nuclear engineering; 3rd ed.* Prentice-Hall, Upper Saddle River, NJ.

[Latge et al., 2006] Latge, C., Groeschel, F., Agostini, P., Dierckx, M., Fazio, C., Guertin, A., Kurata, Y., Laffont, G., Song, T., Thomsen, K., Wagner, W., and Woloshun, K. (2006). MEGAPIE Spallation Target: Design Implementation and Preliminary Tests of the First Prototypical Spallation Target for Future ADS. In *Actinide and Fission Product Partitioning and Transmutation Ninth Information Exchange Meeting*, pages 407–419, Nimes, France.

[Ledoux et al., 1999] Ledoux, X., Borne, F., Boudard, A., Brochard, F., Crespin, S., Drake, D., Duchazeaubeneix, J. C., Durand, D., Durand, J. M., Fréhaut, J., Hanappe, F., Kowalski, L., Lebrun, C., Lecolley, F. R., Lecolley, J. F., Lefebvres, F., Legrain, R., Leray, S., Louvel, M., Martinez, E., Meigo, S. I., Ménard, S., Milleret, G., Patin, Y., Petibon, E., Plouin, F., Pras, P., Stuttge, L., Terrien, Y., Thun, J., Uematsu, M., Varignon, C., Whittal, D. M., and Wlazło, W. (1999). Spallation neutron production by 0.8, 1.2, and 1.6 gev protons on pb targets. *Phys. Rev. Lett.*, 82(22):4412–4415.

[Leray et al., 2002] Leray, S., Borne, F., Crespin, S., Fréhaut, J., Ledoux, X., Martinez, E., Patin, Y., Petibon, E., Pras, P., Boudard, A., Legrain, R., Terrien, Y., Brochard, F., Drake, D., Duchazeaubeneix, J. C., Durand, J. M., Meigo, S. I., Milleret, G., Whittal, D. M., Wlazlo, W., Durand, D., Le Brun, C., Lecolley, F. R., Lecolley, J. F.,

Lefebvres, F., Louvel, M., Varignon, C., Hanappe, F., Ménard, S., Stuttge, L., and Thun, J. (2002). Spallation neutron production by 0.8, 1.2, and 1.6 gev protons on various targets. *Phys. Rev. C*, 65(4):044621.

[Letourneau et al., 2000] Letourneau, A., Galin, J., Goldenbaum, F., Lott, B., Péghaire, A., Enke, M., Hilscher, D., Jahnke, U., Nünighoff, K., Filges, D., Neef, R. D., Paul, N., Schaal, H., Sterzenbach, G., and Tietze, A. (2000). Neutron production in bombardments of thin and thick w, hg, pb targets by 0.4, 0.8, 1.2, 1.8 and 2.5 gev protons. *Nuclear Instruments and Methods in Physics Research Section B: Beam Interactions with Materials and Atoms*, 170(3-4):299 – 322.

[Lindenbaum, 1961] Lindenbaum, S. J. (1961). Shielding of high-energy accelerators. *Annual Review of Nuclear Science*, 11(1):213–259. PMID: 14465443.

[Lu, 2003] Lu, W. (2003). *Radiation damage to materials at SINQ facilities*. Dissertation, North Carolina State University, United States – North Carolina.

[Magill, J. et al., 2007] Magill, J., Galy, J., Dreher, R., Hamilton, D., Tufan, M., Normand, C., Schwenk-Ferrero, A., and Wiese, H. W. (2007). Nucleonica: a nuclear science portal. pages 89–92.

[Maloy et al., 2007] Maloy, S., Hosemann, P., Byler, D., et al. (2007). Irradiation effects in tungsten and tantalum. 3rd High-Power Targetry Workshop, Bad Zurzach, Switzerland.

[Maloy et al., 2005] Maloy, S., James, M., Sommer, W., Willcutt, G., Lopez, M., Romero, T., and Toloczko, M. (2005). The effect of 800 MeV proton irradiation on the mechanical properties of tungsten at room temperature and at 475 0^0 C. *Journal of Nuclear Materials*, 343(1-3):219 – 226. Proceedings of the 6th International Workshop on Spallation Materials Technology.

[Mansur and Coghlan, 1983] Mansur, L. and Coghlan, W. (1983). Mechanisms of helium interaction with radiation effects in metals and alloys: A review. *Journal of Nuclear Materials*, 119(1):1 – 25.

[Mauro, 2009] Mauro, E. (2009). *Radiation protection studies for CERN Linac4/SPL accelerator complex*. PhD thesis, Lausanne.

[McConn Jr et al., 2011] McConn Jr, R. J., Gesh, C. J., Pagh, R. T., Rucker, R. A., and Williams III, R. G. (2011). Compendium of material composition data for radiation transport modeling. Technical Report PNNL-15870, Pacific Northwest National Laboratory, Richland, Washington 99352.

[McManamy et al., 2008] McManamy, T., Gallmeier, F., Rennich, M., Janney, J., and Ferguson, P. (2008). 3 mw solid rotating target design. 2nd Oxford-Princeton High-Power Target Workshop.

[McManamy et al., 2010] McManamy, T., Rennich, M., Gallmeier, F., Ferguson, P., and Janney, J. (2010). 3 mw solid rotating target design. *Journal of Nuclear Materials*, 398(1?3):35 – 42. Proceedings of the Ninth International Workshop on Spallation Materials Technology.

[Medarde et al., 2011] Medarde, M., Moormann, R., Frison, R., Pu?niak, R. J., Pomjakushina, E., Conder, K., Platacis, E., Dai, Y., Kiselev, D., Zanini, L., Török, S., Zagyvai, P., Heinitz, S., Neuhausen, J., Schumann, D., and Thomsen, K. (2011). Lead-gold eutectic: An alternative liquid target material candidate for high power spallation neutron sources. *Journal of Nuclear Materials*, 411(1?3):72 – 82.

[Meng et al., 2010] Meng, C., Tang, J. Y., and Jing, H. T. (2010). Scattering effect in proton beam windows at spallation targets. *ArXiv e-prints*.

[Mueller, 2009] Mueller, A. C. (2009). Prospects for transmutation of nuclear waste and associated proton-accelerator technology. *The European Physical Journal - Special Topics*, 176:179–191. 10.1140/epjst/e2009-01157-8.

[Murdoch et al., 2003] Murdoch, G., Decarlo, A., Henderson, S., Kim, S., Potter, K., Roseberry, T., Rank, J., and Raparia, D. (2003). Beam dump window design for the spallation neutron source. In *Particle Accelerator Conference, 2003. PAC 2003. Proceedings of the*, volume 3, pages 1467 – 1469 vol.3.

[Nabbi, 1979] Nabbi, R. (1979). Die physikalischen Grundlagen der Spallation und ihre möglichen Anwendungen in der Nukleartechnik. Technical Report KFA - IRE - IB - 20/79, Forschungszentrum Jülich.

[NCRP, 2003] NCRP (2003). Radiation protection for particle accelerator facilities. Technical Report NCRP Report no. 144, National Council on Radiation Protection and Measurements.

[NEA, 2006] NEA (2006). Physics and safety of transmutation systems. Technical Report ISBN 92-64-01082-3, OECD, NEA.

[Norgett et al., 1975] Norgett, M., Robinson, M., and Torrens, I. (1975). A proposed method of calculating displacement dose rates. *Nuclear Engineering and Design*, 33(1):50 – 54.

[Polsky et al., 2010] Polsky, Y., Geoghegan, P., Jacobs, L., McTeer, S., and Plum, M. (2010). Beam stop design methodology and description of a new sns beam stop. In *Proceedings of IPAC10, Kyoto, Japan*.

[Robinson, 1994] Robinson, M. T. (1994). Basic physics of radiation damage production. *Journal of Nuclear Materials*, 216(0):1 – 28.

[Roche et al., 1995] Roche, C., Revol, J., Mandrillon, P., Klapisch, R., Kadi, Y., Galvez, J., Carminati, F., Buono, S., Rubio, J., and Rubbia, C. (1995). Conceptual design of a fast neutron operated high power energy amplifier. Technical report. CERN-AT-95-44 ET.

[Russell et al., 1997] Russell, G. J., Ferguson, P. D., Pitcher, E. J., and Court, J. D. (1997). Split-target neutronics and the mlnsc spallation target system. *AIP Conference Proceedings*, 392(1):361–364.

[Russell et al., 1995] Russell, G. J., Pitcher, E. J., and Daemen, L. L. (1995). Introduction to spallation physics and spallation-target design. *AIP Conference Proceedings*, 346(1):93–104.

[Satyamurthy et al., 2007] Satyamurthy, P., Gantayet, L. M., and Ray, A. K. (2007). Heavy density liquid metal spallation target studies for indian ads programme. *Pramana - Journal of Physics*, 68(2):343–353.

[Schmidt et al.,] Schmidt, K. H., Armbruster, P., and Brohm, T. Inverse-kinematic measurements of residues at gsi.

[Seltborg et al., 2005] Seltborg, P., Polanski, A., Petrochenkov, S., Lopatkin, A., Gudowski, W., and Shvetsov, V. (2005). Radiation shielding of high-energy neutrons in sad. *Nuclear Instruments and Methods in Physics Research Section A: Accelerators, Spectrometers, Detectors and Associated Equipment*, 550(1-2):313 – 328.

[Serber, 1947] Serber, R. (1947). Nuclear reactions at high energies. *Phys. Rev.*, 72:1114–1115.

[Shapiro, 2002] Shapiro, J. (2002). *Radiation Protection: A Guide for Scientists, Regulators, and Physicians*. Harvard University Press.

[Shetty, 2010] Shetty, N. V. (2010). Calculation of spallation and activation products in the ess target. Master Thesis.

[Stankovsky et al., 2001] Stankovsky, A., Saito, M., and Artisyuk, V. (2001). Accumulation and transmutation of spallation products in the target of accelerator-driven system. *J Nucl Sci Technol*, 38:503–510.

[Steyn et al., 1990] Steyn, G., Nortier, F., and Mills, S. (1990). Helium cooling of a double-foil window for external cyclotron beams. *Nuclear Instruments and Methods in Physics Research Section A: Accelerators, Spectrometers, Detectors and Associated Equipment*, 292(1):35 – 44.

[Sullivan, 1992] Sullivan, A. H. (1992). *A Guide to Radiation and Radioactivity Levels Near High Energy Particle Accelerators*. Nuclear Technology Publishing.

[Takashita and Takahashi, 1997] Takashita, H. and Takahashi, H. (1997). Radiation damage to a transmutation system based on a proton accelerator. *Nuclear Instruments and Methods in Physics Research Section A: Accelerators, Spectrometers, Detectors and Associated Equipment*, 399(2?3):421 – 431.

[Teichmann, 2006] Teichmann, S. (2006). Shielding parameters of concrete and polyethylene for the psi proton accelerator facilities. In *Shielding Aspects of Accelerators, Targets and Irradiation Facilities - SATIF 8*, pages 45–54.

[Trebukhovsky et al., 2005] Trebukhovsky, Y., Titarenko, Y., Batyaev, V., Mulambetov, R., Mulambetova, S., Smirnov, G., Lipatov, K., Koldobsky, A., Zhivun, V., Barashenkov, V., Kumawat, H., Mashnik, S., and Prael, R. (2005). Double-differential cross sections for the production of neutrons from pb, w, zr, cu, and al targets irradiated with 0.8-, 1.0-, and 1.6-gev protons. *Physics of Atomic Nuclei*, 68:3–15. 10.1134/1.1858552.

[Trellue, 2003] Trellue, H. R. (2003). Reduction of the radiotoxicity of spent nuclear fuel using a two-tiered system comprising light waste reactors and accelerator-driven systems. Technical Report LA-14052-T, Los Alamos National Laboratory.

[Turner, 2007] Turner, J. E. (2007). *Atoms, Radiation, and Radiation Protection*. WILEY-VCH Verlag GmbH & Co.

[Ullmaier and Carsughi, 1995] Ullmaier, H. and Carsughi, F. (1995). Radiation damage problems in high power spallation neutron sources. *Nuclear Instruments and Methods in Physics Research Section B: Beam Interactions with Materials and Atoms*, 101(4):406 – 421.

[Villagrasa-Roussel et al., 2006] Villagrasa-Roussel, C., Broeders, C., and Konobeyev, A. (2006). Irradiation damages in tantalum spallation target.

[Wang and Porile, 1987] Wang, C. and Porile, N. (1987). Systematics of thick-target recoil properties of deep spallation and fragmentation productions of high-energy proton reactions. *Nuclear Physics A*, 468(3-4):711 – 718.

[Watanabe, 1999] Watanabe, N. (1999). Material issues for spallation target by gev proton irradiation. In Yoshida, T. and Fukahori, T., editors, *Proceedings of the 1998 Symposium on Nuclear Data November 19-20, 1998, JAERI, Tokai, Japan*, pages 72–77. Japan Atomic Energy Research Institute.

[Watanabe, 2003] Watanabe, N. (2003). Neutronics of pulsed spallation neutron sources. *Reports on Progress in Physics*, 66(3):339.

[Wechsler et al., 1997] Wechsler, M., Lin, C., Sommer, W., Daemen, L., and Ferguson, P. (1997). Radiation effects in materials for accelerator-driven neutron technologies. *Journal of Nuclear Materials*, 244(3):177–184.

[Wechsler and Sommer, 1984] Wechsler, M. S. and Sommer, W. F. (1984). Spallation radiation damage and the radiation damage facility at the lampf a-6 target station. *Journal of Nuclear Materials*, 123(1-3):1078 – 1084.

[Weisskopf, 1937] Weisskopf, V. (1937). Statistics and nuclear reactions. *Phys. Rev.*, 52:295–303.

[Wiehr, 2003] Wiehr, S. (2003). Measurement of gas and volatile elements production cross section in a molten lead-bismuth target.

[Wladyslaw and Pohorecki, 2006] Wladyslaw and Pohorecki (2006). Calculation of induced radioactivity in the sad spallation target. *Nuclear Instruments and Methods in Physics Research Section A: Accelerators, Spectrometers, Detectors and Associated Equipment*, 562(2):1001 – 1004. Proceedings of the 7th International Conference on Accelerator Applications-AccApp05-7th International Conference on Accelerator Applications.

[Yurevich, 2009] Yurevich, V. (2009). Neutron production in pA and AA collisions at intermediate energies. *Physics of Particles and Nuclei*, 40:49–66. 10.1134/S1063779609010031.

[Yurevich et al., 2006] Yurevich, V. I., Yakovlev, R. M., and Lyapin, V. G. (2006). Neutron emission in interactions of ^{1}H, ^{2}H, ^{4}He, and ^{12}C nuclei with lead nuclei at 1-2 GeV per nucleon. *Physics of Atomic Nuclei*, 69:1496–1509.

APPENDIX A

Appendix

Table A.1: Physical properties and abundance of period 6 elements [Wiki, 2012]

Element Symbol	**Density at RT** g/cm^3	**Melting Point** °C	**Boiling Point** °C	**Crustal Abundance** ppm
Hf	13.31	2233	4603	5.8
Ta	16.69	3017	5458	1 to 2
W	19.25	3422	5555	-
Re	21.02	3186	5596	0.001
Os	22.59	3033	5012	0.00005
Ir	22.56	2466	4428	0.001
Pt	21.45	1768	3825	0.005
Au	19.3	1064	2856	-
Hg	13.53	-38.83	356.73	0.08
Tl	11.85	304	1473	-
Pb	11.34	327.46	1749	-
Bi	9.78	271.5	1564	-

Table A.2: Isotopic composition of natural tungsten

Isotope	**Composition (%)**
^{180}W	0.12
^{182}W	26.5
^{183}W	14.31
^{184}W	30.64
^{186}W	28.43

Table A.3: Atomic and physical properties of tungsten [MTS, 2012]

Atomic Number	74
Atomic Weight	183.86
Density at 20 °C (gm/cc)	19.3
Melting Point °C	3410
Boiling Point °C	5530
Linear Coefficient of Expansion per °C	4.3×10^{-6}
Thermal Conductivity at 20 °C (cal/cm/°C/sec)	0.4
Specific Heat at 20 °C (cal/gram/°C)	0.032
Tensile Strength at Room Temp., psi	100,000 - 500,000
Tensile Strength at 500 °C, psi	75,000 - 200,000
Tensile Strength at 1000 °C, psi	50,000 - 75,000
Working Temperature, °C	<1700
Recrystallization Temperature, °C	1300 - 1500

Table A.4: Material data for helium [AGATE, 2011]

Properties helium:	
Density (393 K / 60 bar)	7.2 $g \cdot cm^{-3}$
Density (593 K / 60 bar)	4.8 $g \cdot cm^{-3}$
Dynamic viscosity (393 K / 60 bar)	2.4×10^{-5} $kg \cdot m^{-1} \cdot s^{-1}$
Dynamic viscosity (593 K / 60 bar)	3.1×10^{-5} $kg \cdot m^{-1} \cdot s^{-1}$
Thermal conductivity (393 K / 60 bar)	0.19 $W \cdot m^{-1} \cdot K^{-1}$
Thermal conductivity (593 K / 60 bar)	0.25 $W \cdot m^{-1} \cdot K^{-1}$
Specific thermal capacity	5.2 $J \cdot g^{-1} \cdot K^{-1}$

Table A.5: Properties of different PBW materials [AGATE, 2011]

Properties stainless steel 1.4429:	
Density (20 °C)	7.98 g·cm^{-3}
Melting point	1425 °C
Young's modulus (20 °C and 400 °C)	200 GPa and 172 GPa
Linear thermal expansion coefficient (20-100 °C)	16×10^{-6} K^{-1}
Thermal conductivity (20 °C)	15 W·m^{-1}·K^{-1}
Specific heat (20°C)	0.5 J·g^{-1}·K^{-1}
Properties aluminum AlZnMgCu1,5:	
Density (20 °C)	2.78 g·cm^{-3}
Melting point	640 °C
Young's modulus (20 °C)	70 GPa
Linear thermal expansion coefficient (20-100 °C)	23.6×10^{-6} K^{-1}
Thermal conductivity (20 °C)	130-160 W·m^{-1}·K^{-1}
Specific heat (20 °C)	0.9 J·g^{-1}·K^{-1}
Yield point Rp$_{p0.2}$ (20 °C)	440 MPa
Properties Incoloy 825 (2.4858):	
Density (20 °C)	8.12 g·cm^{-3}
Melting point	1370 - 1400 °C
Young's modulus (20 °C)	195 GPa
Linear thermal expansion coefficient (20-100 °C)	14×10^{-6} K^{-1}
Thermal conductivity (20 °C)	11 W·m^{-1}·K^{-1}
Specific heat (20 °C)	0.5 J·g^{-1}·K^{-1}
Yield point R$_{p0.2}$ (20°C, 400 °C)	235MPa , 160 MPa
Properties TiAl6V4 (grade5):	
Density (20 °C)	4.43 g·cm^{-3}
Melting point	1660 °C
Young's modulus (20 °C)	110 GPa
Linear thermal expansion coefficient (20-100 °C)	9×10^{-6} K^{-1}
Thermal conductivity (20 °C)	7.1 W·m^{-1}·K^{-1}
Specific heat (20 °C)	0.56 J·g^{-1}·K^{-1}
Yield point R$_{p0.2}$ (20 °C)	830 MPa
Properties Zircaloy 4:	
Density (20 °C)	6.55 g·cm^{-3}
Melting point	1850 °C
Young's modulus (20 °C)	99 GPa
Linear thermal expansion coefficient (20-100 °C)	6×10^{-6} K^{-1}
Thermal conductivity (20 °C)	21.5 W·m^{-1}·K^{-1}
Specific heat (20 °C)	0.29 J·g^{-1}·K^{-1}
Yield point R$_{p0.2}$ (20 °C)	240 MPa

Table A.6: Recommended values for displacement threshold energy (* updated value) [Lu, 2003]

Metals	**T_d (eV)**
Al	27*
Ti	30
V	40
Cr	40
Mn	40
Fe	40
Co	40
Ni	40
Cu	30
Zr	40
Nb	60
Mo	60
Ta	90
W	90
Pb	25

Table A.7: Radiation weighting factors

Radiation type and energy	**Radiation weighting factor**
Photons, all energies	1
Electrons, myons, all energies	1
Neutrons	
$<$ 10 keV	5
10 keV to 100 keV	10
$>$ 100 keV to 2 MeV	20
$>$ 2 MeV to 20 MeV	10
$>$ 20 MeV	5
Protons $>$ 2 MeV	5
Alpha particles, fission fragments, heavy nuclei	20

Table A.8: Flux-to-dose conversion factors for neutrons [Teichmann, 2006]

$\mathbf{E}_n$ **(MeV)**	$\mathbf{CF}_n$ **(pSv cm^2)**
2.50E-08	11.4
0.024	20.2
0.144	134
0.25	215
0.57	355
1.2	433
2.5	437
2.8	433
3.2	429
5	420
14.8	561
19	600
30	515
50	400
75	330
100	300
150	285
200	285
300	306
400	349
500	420
600	487

Table A.9: Flux-to-dose conversion factors for photons [Teichmann, 2006]

$\mathbf{E_\gamma}$ **(MeV)**	$\mathbf{CF_\gamma}$ **(pSv cm^2)**
0.01	0.082
0.015	0.84
0.02	1.04
0.03	0.81
0.04	0.61
0.05	0.51
0.06	0.51
0.08	0.56
0.1	0.62
0.15	0.87
0.2	1.23
0.3	1.81
0.4	2.36
0.5	2.78
0.6	3.46
0.8	4.19
1	5.18
1.5	6.92
2	8.25
3	10.4
4	10.7
5	10.4
6	9.57
8	9.1
600	8.8

Table A.10: Comparison of properties of shielding materials (++ very good, + good, - bad) [Hanslik, 2006]

Properties	**Steel**	**Stainless Steel**	**Cast Steel**	**Lead**	**Tungsten**	**Normal Concrete**	**Heavy Concrete**
Density (g/cm^3)	7.85	7.85	7.1	11.34	18.8	2.3	4.3
Homogeneity	++	++	++	++	++	+	+
Strength	++	++	++	-	++	+	+
Fire Resistance	++	++	++	-	++	-	-
Fast Neutron Shielding Efficiency	+	+	+	++	++	-	+
Gamma Shielding Efficiency	+	+	+	++	++	-	+
Activation Sensitivity	medium	high	medium	medium	medium	low	medium
Acquisition cost	medium	medium	medium	high	high	low	low

Table A.11: Mechanical and thermal properties of different types of concrete [Hanslik, 2006]

Properties	**Normal**	**Barite**	**Limonite**	**Borated**
Density (g/cm^3)	2.2-2.4	3.5	4.3-4.5	5.24-5.35
Specific Heat ($kJkg^{-1}K^{-1}$)	0.65	0.52	0.7	0.75
Thermal Conductivity ($Wm^{-1}K^{-1}$)	0.88	1.6	2.8-3.6	0.8
Linear Expansion Co-efficient $(20 - 100\,^0C)(10^{-6}K^{-1})$	14		7	32
Tensile Strength (Mpa)	2.0-3.0	2		
Compression Strength (Mpa)	38	25-29	38	13-16

Table A.12: Composition of boronated steel [McConn Jr et al., 2011]

Element	**Weight fraction**
B	0.01
C	0.000396
Si	0.00495
P	0.000228
S	0.000149
Cr	0.1881
Mn	0.0099
Fe	0.694713
Ni	0.091575

Table A.13: Composition of boronated concrete [McConn Jr et al., 2011]

Element	**Weight fraction**
H	0.005626
B	0.010449
O	0.339596
F	0.002311
Na	0.012157
Mg	0.002311
Al	0.00643
Si	0.033256
S	0.091932
K	0.001005
Ca	0.062896
Mn	0.000201
Fe	0.022003
Zn	0.006631
Ba	0.403195